Site U1408[1]

R.D. Norris, P.A. Wilson, P. Blum, A. Fehr, C. Agnini, A. Bornemann, S. Boulila, P.R. Bown, C. Cournede, O. Friedrich, A.K. Ghosh, C.J. Hollis, P.M. Hull, K. Jo, C.K. Junium, M. Kaneko, D. Liebrand, P.C. Lippert, Z. Liu, H. Matsui, K. Moriya, H. Nishi, B.N. Opdyke, D. Penman, B. Romans, H.D. Scher, P. Sexton, H. Takagi, S.K. Turner, J.H. Whiteside, T. Yamaguchi, and Y. Yamamoto[2]

Chapter contents

Background and objectives 1
Operations 2
Lithostratigraphy 4
Biostratigraphy 6
Paleomagnetism 9
Age-depth model and mass accumulation rates 12
Geochemistry 12
Physical properties 14
Stratigraphic correlation 16
Downhole logging 17
References 18
Figures 20
Tables 61

[1] Norris, R.D., Wilson, P.A., Blum, P., Fehr, A., Agnini, C., Bornemann, A., Boulila, S., Bown, P.R., Cournede, C., Friedrich, O., Ghosh, A.K., Hollis, C.J., Hull, P.M., Jo, K., Junium, C.K., Kaneko, M., Liebrand, D., Lippert, P.C., Liu, Z., Matsui, H., Moriya, K., Nishi, H., Opdyke, B.N., Penman, D., Romans, B., Scher, H.D., Sexton, P., Takagi, H., Turner, S.K., Whiteside, J.H., Yamaguchi, T., and Yamamoto, Y., 2014. Site U1408. *In* Norris, R.D., Wilson, P.A., Blum, P., and the Expedition 342 Scientists, *Proc. IODP,* 342: College Station, TX (Integrated Ocean Drilling Program). doi:10.2204/iodp.proc.342.109.2014
[2] Expedition 342 Scientists' addresses.

Background and objectives

Integrated Ocean Drilling Program (IODP) Site U1408 (proposed Site SENR-21B; 41°26.3′N, 49°47.1′W; ~3022 m water depth) is a mid-depth site (~2575 meters below sea level [mbsl] paleodepth at 50 Ma) (Tucholke and Vogt, 1979) and the shallowest site drilled in the Expedition 342 Paleogene Newfoundland sediment drifts depth transect (Fig. F1). The site was positioned to capture a record of sedimentation ~2 km shallower than the largely sub–carbonate compensation depth (CCD) record drilled at Site U1403 (Figs. F2, F3). The location, well above the average late Paleogene CCD, should be sensitive to both increases and decreases in carbonate burial, whether these reflect variations in dissolution related to changes in the CCD, changes in carbonate production, or variations in background noncarbonate sedimentation. Our primary scientific objectives for drilling Site U1408 were

- To obtain an expanded sequence of Eocene calcareous ooze and chalk to reconstruct the history of both the mid-depth CCD and hyperthermal events in a primarily carbonate-dominated record;
- To obtain records of the Eocene in carbonate-rich sediment that hosts abundant foraminifers suitable to the construction of geochemical climate records;
- To evaluate the history of deep water on sediment chemistry, grain size, and provenance; and
- To evaluate biological evolution during Paleogene climate transitions.

Secondary objectives included the possible recovery of the Eocene/Oligocene boundary and the late Eocene impact at higher sedimentation rates than are typical in pelagic sedimentary sequences.

Site U1408 is a companion site to Site U1407, where we employed an "offset" drilling strategy to obtain advanced piston corer (APC) records through a thicker section of the same sediment drift. Our strategy was designed to test whether Site U1408 would sample (1) a much more expanded sedimentary record of the same middle and lower Eocene sediment recovered by APC at Site U1407 or (2) a section of progressively younger sediment. Result 1 would indicate an overall sedimentary architecture in this Southeast Newfoundland sediment drift that is similar to the one encountered at J-Anomaly Ridge sediment drift. Result 2 would indicate an essentially layer-cake sedimentary sequence.

doi:10.2204/iodp.proc.342.109.2014

The primarily calcareous sequence expected at Site U1408 should record changes in ocean alkalinity and carbonate production. Sites U1403 and U1404 were mainly positioned to capture large-amplitude CCD deepening events, such as the carbonate budget "overshoots," that are thought to be associated with the most extreme climate perturbations of the Cenozoic such as those involved with the Cretaceous/Paleogene boundary, the Paleocene/Eocene Thermal Maximum (PETM) and the Eocene–Oligocene transition (see the **"Site U1403"** and **"Site U1404"** chapters [Norris et al., 2014b, 2014c). Those events are recorded at deepwater sites as stratigraphically thin intervals of calcareous sediment in otherwise noncalcareous sediment. In contrast, transient shoaling of the CCD in generally carbonate rich sequences should be recorded at Site U1408 by decreases in carbonate preservation and decreasing carbonate content relative to clay or biosiliceous sediment, as we have already observed at Sites U1406 and U1407. As an upper-end site on the Newfoundland depth transect, Site U1408 could have few intervals in which the sediment is 100% carbonate, but also intervals where carbonate abundance falls in the record. Carbonate content was expected to be generally higher at sites in shallower water depth, such as the majority of the sites located on Southeast Newfoundland Ridge, including Sites U1407 and U1408.

The high carbonate contents anticipated in sediment at Site U1408 should permit the construction of detailed stable isotope records and calcareous microfossil biostratigraphy that can be tied by physical property records and magnetochronology to Sites U1403–U1406 further downslope. Ties between sites on Southeast Newfoundland Ridge and those on J-Anomaly Ridge will allow the isotope stratigraphy and biochronology developed for Sites U1406–U1408 to be exported to the lower ends of the depth transect. Site U1408 assumes greater importance in the depth transect because the lower and middle Eocene sedimentary sequence was expected to be more expanded than at any other Expedition 342 site.

Ultimately, the goal was to use the combination of the lower and middle Eocene record at Sites U1408 and U1407 and the younger Paleogene record at Site U1406 to produce composite stable isotope and carbonate content records that can be tied to the more intermittent geochemical records at Sites U1403–U1405. Our aim was to match carbonate-rich intervals across all of the J-Anomaly Ridge sites with the sites on Southeast Newfoundland Ridge to create an orbital-resolution record of fluctuations in ocean chemistry and deep water origins.

Site U1408 was proposed when we discovered that the subtle but recognizable internal stratigraphy of the acoustically transparent sequence on J-Anomaly Ridge was perhaps age diagnostic. Seismic data show an intermittent fuzzy reflector near the middle of the J-Anomaly Drift as well as a zone of fuzzy, slightly less transparent reflections in the lower half of the drift. Drilling on J-Anomaly Ridge showed that these two fuzzy reflector packages correspond to the Eocene/Oligocene boundary and lower and middle Eocene sediment. We used this interpretation of the seismic stratigraphy to propose sites that would preferentially target the lower half of the acoustically transparent seismic package. Site U1408 and its companion, Site U1407, were designed to recover APC records of the lower and middle Eocene sequence and to avoid drilling a large thickness of Miocene sediment such as that encountered at Sites U1404 and U1405.

The seismic stratigraphy of Site U1408 shows a complex array of reflectors below the presumed Eocene sedimentary sequence. We proposed to core by APC through the acoustically transparent sequence and stop at the cherts that occur in the middle lower Eocene at Site U1407. This strategy should collect a sedimentary record at the thickest part of the Eocene section.

We expected that Site U1408 would provide an expanded record of primarily calcareous ooze and chalk of rough age equivalence to sites in deeper water on J-Anomaly Ridge. In particular, Site U1408 should provide our highest deposition rate record of the early and middle Eocene as a counterpart to the largely sub-CCD record at Site U1403 and thereby improve age and water-depth control on the behavior of the CCD in the North Atlantic during this key interval of the Cenozoic when the CCD in the equatorial Pacific was at its most dynamic (Lyle, Wilson, Janecek, et al., 2002; Pälike et al., 2012).

Operations

All times are local ship time (UTC – 2.5). See Table **T1** for coring summary.

Hole U1408A summary

Latitude: 41°26.2985′N
Longitude: 49°47.1483′W
Water depth below sea level (m): 3021.6
Date started: 2045 h, 11 July 2012
Date finished: 1045 h, 13 July 2012
Time on hole (days): 1.6
Seafloor depth (m drilling depth below rig floor [DRF]): 3033.2
Seafloor depth est. method: mudline core
Rig floor to sea level (m): 11.64

Penetration depth (m drilling depth below seafloor [DSF]): 246.5
Cored interval (m): 246.5
Recovered length (m): 243.92
Recovery (%): 99
Total cores (number): 27
APC cores (number): 20
Extended core barrel (XCB) cores (number): 7
Drilling system: 11⅞ inch APC/XCB bit with 136.00 m bottom-hole assembly (BHA)
Objective: core from seafloor to ~250 m DSF or until science objectives are met
Result: target reached; objectives met

Hole U1408B summary

Latitude: 41°26.2989′N
Longitude: 49°47.1361′W
Water depth below sea level (m): 3022.1
Date started: 1045 h, 13 July 2012
Date finished: 1700 h, 14 July 2012
Time on hole (days): 1.3
Seafloor depth (m DRF): 3033.8
Seafloor depth est. method: mudline core
Rig floor to sea level (m): 11.69
Penetration depth (m DSF): 217.5
Cored interval (m): 214.5
Recovered length (m): 224.09
Recovery (%): 104
Drilled interval (m): 3
Drilled interval (number): 1
Total cores (number): 25
APC cores (number): 17
XCB cores (number): 8
Drilling system: 11⅞ inch APC/XCB bit with 136.00 m BHA
Objective: core from seafloor to ~220 m DSF
Result: target reached; objectives met

Hole U1408C summary

Latitude: 41°26.2878′N
Longitude: 49°47.1345′W
Water depth below sea level (m): 3022.5
Date started: 1700 h, 14 July 2012
Date finished: 0715 h, 16 July 2012
Time on hole (days): 1.6
Seafloor depth (m DRF): 3034.2
Seafloor depth est. method: mudline core
Rig floor to sea level (m): 11.71
Penetration depth (m DSF): 187.5
Cored interval (m): 184.5
Recovered length (m): 181.52
Recovery (%): 98
Drilled interval (m): 3
Drilled interval (number): 1
Total cores (number): 22
APC cores (number): 18
XCB cores (number): 4
Drilling system: 11⅞ inch APC/XCB bit with 136.00 m BHA
Objective: repeat cored sequence from Hole U1408B
Result: target reached; objectives met

Description

The vessel arrived at Site U1408 after a 1.46 nmi dynamic positioning move from Site U1407, which took 1.75 h at 0.83 kt. The vessel stabilized over Site U1408 at 2045 h on 11 July 2012. The plan for Site U1408 called for drilling three holes to ~250 m DSF. Holes U1408A, U1408B, and U1408C were successfully cored to 246.5, 217.5, and 187.5 m DSF, respectively. The total time spent at Site U1408 was 106.5 h (4.4 days).

Hole U1408A coring

A mudline core of 4.3 m determined seafloor depth at 3033.2 m DRF (3021.6 mbsl). Hole U1408A was spudded at 2335 h on 11 July, and Cores 342-U1408A-1H through 20H were retrieved using nonmagnetic core barrels and the FlexIT core orientation tool. Core 14H experienced the first partial stroke, and the APC was advanced by recovery to the APC total depth of 182.9 m DSF. The XCB was deployed for Cores 21X through 27X to a final depth of 246.5 m DSF. The seafloor was cleared at 1045 h on 13 July, ending Hole U1408A. Overall core recovery for Hole U1408A was 243.92 m for the 246.5 m interval cored (99.0% recovery). The total time spent on Hole U1408A was 38.00 h.

Hole U1408B coring

The vessel was offset 20 m east. Hole U1408B was spudded at 1230 h on 13 July, and the 6.74 m long mudline core established the seafloor at 3033.8 m DRF (3022.1 mbsl). Cores 342-U1408B-1H through 18H were retrieved using nonmagnetic core barrels and the FlexIT core orientation tool. A 3 m long interval (25.7–28.7 m DSF) was drilled without recovery to optimize coverage of coring gaps in Hole U1408A. Coring was slowed when the FlexIT tool housing sheared at the overshot connection above the core barrel three times in the APC section of Hole U1408B. Total advance including the drilled interval with the APC was 154.5 m. The XCB was deployed for Cores 19X through 26X to a final depth of 217.5 m DSF. The seafloor was cleared at 1700 h on 14 July, ending Hole U1408B. The recovery for Hole U1408B was 224.09 m over the 214.5 m cored (104.5% recovery). The total time spent on Hole U1408B was 30.25 h.

Hole U1408C coring

The vessel was offset 20 m south, and Hole U1408C was spudded at 1905 h on 14 July. Cores 342-U1408C-1H through 19H (0–165.1 m DSF) were retrieved using nonmagnetic core barrels. Core orientation was performed with Cores 6H through 8H. A 3 m long interval (8.8–11.8 m DSF) was drilled without recovery to optimize coverage of coring gaps in the previous holes. Again, the FlexIT tool was held responsible for mechanical trouble, including one mechanical shear at the overshot and one mechanical shear of the APC shear pins. During APC operations, an intermittent electrical fault developed, and coring operations were suspended for 6.5 h while the problem was located and fixed. The XCB was deployed for Cores 20X through 23X to a final depth of 187.5 m DSF. The drill string was pulled to the surface and the drill floor was secured at 0715 h on 16 July, ending Hole U1408C. The vessel began the transit to Site U1409. The recovery for Hole U1408C was 181.52 m over the 184.5 m cored (98.4% recovery). The total time spent on Hole U1408C was 38.25 h.

Lithostratigraphy

The sedimentary succession recovered from Holes U1408A–U1408C consists of pelagic deep-sea sediment of Pleistocene to upper Paleocene age and is divided into four lithostratigraphic units (Figs. **F4, F5, F6;** Table **T2**).

Unit I is ~13 m thick and composed of Pleistocene to Oligocene sediment. Brown silty clay is found in the core top, underlain by brownish foraminiferal nannofossil ooze and interbedded reddish brown clay. Manganese nodules and dropstones are common. The 10 m thick Unit II (Oligocene) consists of silty clay with nannofossils and nannofossil clay with silt. Unit III is a 202 m thick sequence of greenish gray nannofossil clays with cyclic color changes between greenish gray to dark green and very light gray intervals on a decimeter scale. The upper 3 m of Unit III is Oligocene in age followed by 199 m of middle Eocene aged sediments. Unit IV was recovered only in Hole U1408A and consists principally of lower Eocene whitish nannofossil chalk and upper Paleocene pinkish brown nannofossil chalk.

Lithostratigraphic units and boundaries are defined by changes in lithology as identified by visual core description and smear slide observations (Figs. **F7, F8, F9**), physical properties including color reflectance (L*, a*, and b*), and biogenic content (calcium carbonate) (Fig. **F4**). Lithologic differences observed between units are primarily attributable to varying abundances of nannofossils, diatoms, radiolarians, and foraminifers. Lithologic descriptions are based on sediment recovered from Hole U1408A and supplemented with observations from the two shorter holes, U1408B and U1408C.

Unit I

Intervals: 342-U1408A-1H-1, 0 cm, to 2H-6, 42 cm; 342-U1408B-1H-1, 0 cm, to 2H-5, 52 cm; 342-U1408C-1H-1, 0 cm, to 3H-1, 113 cm

Depths: Hole U1408A = 0–12.22 meters below seafloor (mbsf); Hole U1408B = 0–13.22 mbsf; Hole U1408C = 0–12.93 mbsf

Age: Pleistocene to Oligocene

Lithology: clayey silt, nannofossil foraminiferal ooze, and clay

Unit I was encountered in all three holes at Site U1408 (Fig. **F5A, F5B;** Table **T2**) and comprises a 12–13 m thick succession of sediment of brown (7.5YR 5/3) and gray (2.5Y 5/1) clayey silt atop light brown (7.5YR 6/3) well-bioturbated foraminiferal nannofossil ooze (Fig. **F6A;** below 1.50 mbsf). Decimeter-scale alternations of reddish brown (5YR 5/3) clay intervals (Fig. **F5B**) with foraminiferal nannofossil ooze are observed throughout, likely representing Pleistocene glacial–interglacial cycles. The foraminiferal nannofossil oozes have layers and blebs of clayey brick-red sediment throughout as well as foraminiferal sand layers (Fig. **F5A**). Bioturbation is moderate to complete with rare discrete burrows. Core 342-U1408A-2H contains discrete manganese nodules as large as 6 cm in diameter. Patches of disseminated manganese oxide increase in abundance downhole. Reworking was documented on the basis of biostratigraphy in Sections 342-U1408A-2H-4 through 2H-5, where sediments containing Pliocene and Miocene calcareous nannofossils are both underlain and overlain by Pleistocene age sediment. Dropstones occur occasionally in the Pleistocene sequences. The most prominent example is a subrounded, metamorphic rock cobble ~6 cm in diameter occurring close to the base of Unit I in Hole U1408B. The basal boundary of Unit I is defined by a change from predominantly brownish (7.5YR 5/3) foraminiferal nannofossil ooze to yellow-brown (2.5Y 7/3) silty clays. In addition, underlying Unit II displays lower and less variable magnetic susceptibility values than Unit I. The boundary between the two units is characterized by a sharp drop in carbonate content into Unit II from ~40 to <10 wt% (Fig. **F4**).

Unit II

Intervals: 342-U1408A-2H-6, 42 cm, to 3H-6, 92 cm; 342-U1408B-2H-5, 52 cm, to 3H-5, 150 cm; 342-U1408C-3H-1, 113 cm, to 4H-2, 57 cm

Depths: Hole U1408A = 12.22–22.22 mbsf; Hole U1408B = 13.22–23.72 mbsf; Hole U1408C = 12.93–23.37 mbsf
Age: Miocene to Oligocene
Lithology: silty clay, silty clay with nannofossils, and nannofossil clay with silt

Unit II is ~10 m thick and consists of silty clay with nannofossils (Figs. F5C, F6B) to nannofossil clay with silt. Color grades downhole from pale yellow (2.5Y 7/3) over light gray (2.5Y 7/3) to brown (10YR 5/3). Lightness (L*) also decreases downhole (Fig. F4). The upper pale yellow interval (Sections 342-U1408A-2H-6, 42 cm, through 2H-CC) has abundant layers and flecks of manganese oxide and high silt content relative to Unit I. The sediment is well bioturbated and homogenized. A distinct color change from brown to greenish gray nannofossil clay within nannofossil Zone NP23 (see "Biostratigraphy") marks the basal boundary of Unit II. Unit II has the lowest carbonate values at this site (<10 wt%), and the transition toward Unit III is characterized by an increase to >40 wt% (Fig. F4).

Unit III

Intervals: 342-U1408A-3H-6, 92 cm, to 25H-5, 94 cm; 342-U1408B-3H-5, 150 cm, to 26X-CC, 25 cm; 342-U1408C-4H-2, 57 cm, to 22X-CC, 51 cm
Depths: Hole U1408A = 22.22–224.64 mbsf; Hole U1408B = 23.72–213.7 mbsf (bottom of hole [BOH]); Hole U1408C = 23.37–179.96 mbsf (BOH)
Age: Oligocene to middle Eocene
Lithology: nannofossil clay/claystone and nannofossil ooze

Unit III is a 202 m thick succession of predominantly greenish gray (10Y 5/1 to 10Y 6/1 and 5GY 5/1 to 5GY 6/1) nannofossil clay (Figs. F4, F5D, F6C). Green mottles and layers as well as brownish blebs and burrows are observed throughout this unit. Commonly intercalated within this rather uniform lithology are light gray (10Y 8/1 and N 7) to white (N 8) nannofossil ooze (Fig. F5E). The successive occurrences of these beds are, in some cores, cyclically spaced, suggesting orbital forcing as a possible driving factor (Fig. F10). X-ray diffraction (XRD) analyses suggest that mineralogical composition varies only slightly between the three different lithologies shown in Figure F11, consisting of greenish gray nannofossil clay; a centimeter-thick greenish, possibly glauconite-chlorite–bearing layer; and light gray nannofossil ooze. The main change across color cycles is an increase in the intensity of the XRD calcite peak in the whitish layer compared to the greenish gray intervals. Other identified mineral phases include quartz, illite, chlorite, and kaolinite (in descending order of XRD peak area). Glauconite occurs in discrete bands. Bioturbation is mostly moderate, with common *Zoophycos, Planolites,* and *Chondrites* burrows (Fig. F12). Similar to other sites drilled during Expedition 342, sand-sized lithoclasts dominated by angular, clear quartz are found in the >63 µm size fraction as far downhole as Section 342-U1408A-4H-3 (nannofossil Zone NP23; Oligocene) (Fig. F13). The composition of the sand-sized lithics resembles that of lithics observed at Sites U1404 and U1406 over the same time interval.

Unit III covers the Middle Eocene Climatic Optimum (MECO) (Fig. F10), as identified by planktonic foraminifer biostratigraphy and magnetostratigraphy in Cores 342-U1408A-6H and 7H. This interval is distinguished from the underlying and overlying sediment by well-developed cyclicity and higher carbonate content (Figs. F4, F10). The observed alternations are not unique in this unit, but they are quite distinct during the MECO interval. The transitions from greenish gray nannofossil clay to decimeter-thick, carbonate-rich whitish intervals are often characterized by the occurrence of 1–1.5 cm thick, green glauconite-chlorite–bearing layers at the top of the clay (Fig. F11) that generally have either a sharp contact at the top or bottom and occur nearly exclusively in the greenish gray nannofossil clay. Bundles of millimeter-thick greenish layers are observed in some places. *Zoophycos* burrows are common in the claystone but are crossed by the greenish layers (Fig. F12), suggesting that the thin glauconitic layers formed postdepositionaly. Additionally, in Section 342-U1408A-11H-2 we observed an ~40 cm thick interval of inclined bedding without bioturbation, suggesting reworking of material into a bedform.

The Unit III/ IV boundary is defined by an abrupt change from greenish gray (5GY 6/1) nannofossil claystone to whitish (N 8) nannofossil chalk. Calcium carbonate content increases from ~50 wt% in Unit III to >80 wt% in Unit IV, accompanied by an increase in L* (Fig. F4). Biostratigraphically, this lithologic shift represents a hiatus between nannofossil Subzone NP15a and Zone NP12.

Unit IV

Interval: 342-U1408A-25X-5, 94 cm, to 27X-CC, 25 cm
Depth: Hole U1408A = 224.64–246.64 mbsf
Age: early Eocene to late Paleocene
Lithology: nannofossil chalk (with radiolarians) and chert

Unit IV was recovered only from Hole U1408A and is ~22 m thick. The unit consists predominantly of moderately bioturbated nannofossil chalk (Figs. F5F,

F6D) and chert layers 1–2 cm thick. Core 342-U1408A-26X is composed of white (N 8) to light greenish gray (10GY 8/1) nannofossil chalk with two prominent chert layers in intervals 342-U1408A-26X-1, 15–25 cm, and 26X-3, 144–150 cm, and a light greenish gray (10Y 7/1) nannofossil claystone in the upper half of Section 26X-3. Biostratigraphy constrains the Paleocene/Eocene boundary close to the base of interval 26X-2, 145–150 cm. However, the PETM was not identified and is possibly represented by a hiatus. Sediment in Core 342-U1408A-27X is pale brown (10YR 7/3 to 10YR 8/2) and composed of nannofossil chalk with radiolarians (Figs. F5F, F6D) of late Paleocene age. Pinkish brown (10R 8/3) blebs of montmorillonite occur occasionally in this core.

Lithostratigraphic unit summary

The lithostratigraphy at Site U1408 comprises a discontinuous sedimentary succession of Pleistocene to Paleocene age. All stratigraphic epoch boundaries (Paleocene/Eocene, Eocene/Oligocene, and Oligocene/Miocene) are represented by hiatuses. The division of the recovered lithology at Site U1408 into four lithostratigraphic units is associated with changes in sediment carbonate content (see "Geochemistry"; Fig. F4). The downhole transition from foraminiferal nannofossil ooze to silty clay in Unit II is characterized by a drop from 45 wt% calcium carbonate to values <10 wt%. Across the Unit II/III boundary, calcium carbonate increases from 20 to 40 wt%. The 202 m thick Unit III consists of sediment with ~40–50 wt% calcium carbonate, with cyclically intercalated whitish gray horizons that show substantially higher values of as much as 88 wt%. Unit IV is characterized by high calcium carbonate values between 55 and 91 wt%. All pre-Pleistocene samples show carbonate contents well above 10 wt%, indicating that the site was positioned above the CCD for much of its Cenozoic history.

Middle Eocene Climatic Optimum

The MECO (~40 Ma) was a warming event that lasted ~500 k.y., with a main peak in temperatures for 100 k.y. (Bohaty et al., 2009). The MECO has been observed in most ocean basins and is proposed to be associated with elevated atmospheric pCO_2 levels and ocean acidification inferred from shoaling of the CCD (Bohaty et al., 2009; Bijl et al., 2010). Biostratigraphically, the interval is well constrained by the occurrence of the planktonic foraminifer *Orbulinoides beckmanni* (planktonic foraminiferal Zone E12; Edgar et al., 2010). At Site U1408, the MECO is distinguished from the underlying and overlying sediment by well-developed cyclicity and higher carbonate content (Figs. F4, F10). Cyclic alternation on a decimeter scale between greenish gray nannofossil clay and whitish to light gray nannofossil ooze occurs throughout the MECO interval. These cycles are not restricted to the MECO itself; they occur nearly throughout all of Unit III, but they are more distinct than directly above or below this interval. Similar well-developed cyclicity is observed in Cores 342-U1408A-9H and 10H, probably representing carbonate accumulation Event 3, and in Cores 16H and 17H.

Origin of green layers

The sediment of Unit II includes green layers that contain glauconite and chlorite. At Site U1406, we hypothesized that these layers represent times of no, or extremely slow, deposition. However, *Zoophycos* burrows observed in Core 342-U1408A-24H are crosscut by these layers (Fig. F12), suggesting that these thin greenish glauconitic layers formed postdeposition and therefore are diagenetic in origin. One possibility is that these green layers represent a reduction/oxidation boundary that formed syndepositionally with the carbonate-rich white layers. The green banding is rarely seen in the white layers. If we assume that the background carbonate flux is relatively constant and changes in sedimentation rate are driven by changes in the clay flux to the site, the occurrence of more numerous green layers within the greenish gray nannofossil clay beneath the white carbonate layers would be consistent with a slowdown in sedimentation rate during intervals of background sedimentation less diluted by clay (Fig. F11). The more common greenish gray, clay-rich layers would then represent higher sedimentation rates. Individual green bands are typically 1–1.5 cm thick but can grade in intensity in either direction. The green layers have a very sharply delineated top or bottom paired with a diffuse boundary on the opposite side and can appear thicker when multiple generations of the green bands are stacked together (Figs. F11, F12).

Biostratigraphy

Coring at Site U1408 recovered a 250 m thick sequence of Pleistocene to upper Paleocene clayey nannofossil ooze with varying amounts of clay and nannofossils. The uppermost Pleistocene section comprises foraminifer sand and clay. Minor nannofossil ooze and chert lithologies occur in the lower Eocene to Paleocene section. Nannofossils, planktonic foraminifers, and benthic foraminifers are present through most of the succession. Radiolarians are only present in a short interval of the middle Eocene and upper Paleocene. Thin Pleistocene, upper Mio-

cene, and lower Oligocene intervals overlie a middle Eocene through upper Paleocene succession with significant hiatuses between the Oligocene and middle Eocene (~7 m.y.) and middle and lower Eocene (~3 m.y.) and a minor hiatus or condensed interval around the Paleocene/Eocene boundary. Sedimentation rates are high (~1.49–3.14 cm/k.y.) through the middle Eocene, low through the lower Eocene (~0.08 cm/k.y.), and relatively high through the upper Paleocene (~1.27 cm/k.y.).

Benthic foraminifers are generally rare (the "present" category) apart from the uppermost Eocene to Oligocene succession, where they become abundant to dominant. Benthic foraminifer preservation is good to very good through most of the recovered sequence, although poor preservation occurs in the Oligocene and lower Eocene.

An integrated calcareous and siliceous microfossil biozonation is shown in Figure **F14.** Datum and zonal determinations from nannofossils, planktonic foraminifers, and radiolarians are in close agreement. An age-depth plot including biostratigraphic and paleomagnetic datums is shown in Figure **F15.** A summary of calcareous and siliceous microfossil abundances and preservation is given in Figure **F16.**

Calcareous nannofossils

Calcareous nannofossil biostratigraphy is based on analysis of core catcher and additional working section-half samples from Hole U1408A. Depth positions and age estimates of biostratigraphic marker events are shown in Table **T3.** Calcareous nannofossil occurrence data are shown in Table **T4.** Note that the distribution chart is based on shipboard study only and is, therefore, biased toward age-diagnostic species.

At Site U1408, the preservation of calcareous nannofossils is generally good to exceptional in the middle Eocene but poor to moderate in the Oligocene, lower Eocene, and upper Paleocene. The uppermost sediment in Hole U1408A contains abundant nannofossils indicative of Pleistocene Zones NN21–NN18, as indicated by the presence of abundant *Emiliania huxleyi* in Sample 342-U1408A-1H-1, 75 cm (0.75 mbsf), top of *Pseudoemiliania lacunosa* in Sample 2H-3, 100 cm (8.30 mbsf), and top of *Discoaster brouweri* in Sample 2H-4, 100 cm (9.80 mbsf). The sample below this (Sample 3H-4, 100 cm; 11.30 mbsf) contains the short-ranging upper Miocene Zone NN9 marker species *Discoaster hamatus*. The short interval from Sample 342-U1408A-2H-7, 35 cm, to 4H-2, 150 cm (13.16–27.31 mbsf), can be assigned to Oligocene Zones NP25/NP23 to upper Zone NP23 based on the presence of *Dictyococcites biscectus* and the top and base of *Sphenolithus distentus*. Assemblages at the top of this interval are significantly etched. The identification of Zone NP23 in Sample 342-U1408A-4H-2, 150 cm (26.30 mbsf), and Zone NP17 in Sample 4H-3, 100 cm (27.30 mbsf), indicates the presence of a hiatus of ~8 m.y. representing the upper Eocene to lower Oligocene.

The sequence from Sample 342-U1408A-4H-4, 100 cm, through 27X-CC (28.81–246.59 mbsf) is assigned to the middle Eocene to upper Paleocene nannofossil Zones NP17–NP7/NP8. The majority of primary zonal marker species are present and listed in Table **T3.** The identification of Zone NP14 in Sample 342-U1408A-25X-5, 100 cm (224.70 mbsf), and Zone NP12 in Sample 25X-6, 80 cm (226.0 mbsf), indicates the presence of a short hiatus (~2 m.y.). The Paleocene–Eocene transition is indicated by the identification of Zone NP10 in Sample 342-U1408A-26X-2, 145 cm (229.44 mbsf), and Subzone NP9a in Sample 26X-2, 150 cm (229.49 mbsf), but the apparent absence of Subzone NP9b suggests the presence of a short hiatus (<1 m.y.) that may include most of the PETM. The PETM nannofossil excursion taxa, such as *Discoaster araneus,* were not observed.

The interval from Sample 342-U1408A-26X-2, 150 cm, to 27X-CC (229.49–246.59 mbsf) is assigned to Subzone NP9a and undifferentiated Zones NP7/NP8 based on the base of *Discoaster multiradiatus* (Sample 27X-5, 97 cm; 243.88 mbsf) and presence of *Discoaster mohleri* in the lowest Sample 27X-CC (246.59 mbsf).

Radiolarians

Radiolarian biostratigraphy is based on analysis of all core catcher samples from Hole U1408A and selected working half section samples from Cores 342-U1408A-16H, 17H, 26X, and 27X. No samples from Hole U1408B or U1408C were examined. Radiolarians are either absent or indeterminate through much of Hole U1408A but are abundant for a short interval in the middle Eocene and upper Paleocene. Sparse assemblages occur through the Paleocene–Eocene transition in Cores 25X and 26X. Depth positions and age estimates of biostratigraphic marker events are shown in Table **T5,** and the radiolarian distribution is shown in Table **T6.** Note that the distribution chart is based on shipboard study only and is, therefore, biased toward age-diagnostic species.

Samples 342-U1408A-1H-CC through 13H-CC (4.36–118.84 mbsf) are barren of radiolarians. Samples 14H-CC through 15H-CC (128.20–137.61 mbsf) contain only poorly preserved spumellarian radiolarians that cannot be assigned to species.

Samples 342-U1408A-16H-6, 78–80 cm, through 17H-3, 69–71 cm (144.29–150.50 mbsf), contain

abundant and well-preserved middle Eocene radiolarians. The interval is correlated to radiolarian Zone RP13 based on the co-occurrence of rare *Eusyringium fistuligerum,* a key index species for the zone, and *Calocyclas tripocha,* a species that appears to be restricted to Zone RP13 (Kamikuri et al., 2012). The top of *Podocyrtis dorus* in Sample 342-U1408A-17H-3, 69–71 cm (150.50 mbsf), supports this correlation. *Periphaena tripyramis triangula* is present throughout this interval, although its last occurrence is recorded within underlying Zone RP12 in the equatorial Pacific (Kamikuri et al., 2012).

Samples 342-U1408A-17H-CC through 24X-CC (156.00–215.88 mbsf) contain only poorly preserved spumellarian radiolarians that cannot be assigned to species. Samples 25X-CC through 26X-1, 54–55 cm (227.29–227.85 mbsf), contain rare radiolarians of moderate preservation. The presence of rare specimens of the Eocene species *Dictyoprora amphora* indicates that this interval is no older than radiolarian Zone RP8 (Foreman, 1973). Samples 342-U1408A-26X-4, 85–86 cm, through 27X-CC (231.85–246.59 mbsf) are assigned to Zone RP7 based on the common occurrence of primary index species *Bekoma bidartensis*. As at Sites U1406 and U1407, this interval includes the lowermost Eocene indicator species *Podocyrtis papalis, Theocorys? phyzella,* and *Theocorys?* aff. *phyzella* (sensu Sanfilippo and Blome, 2001). However, nannofossils and benthic foraminifers indicate that this interval is of Paleocene age.

Planktonic foraminifers

Core catchers and additional samples from working section halves were examined in Hole U1408A. Samples contain diverse and well-preserved assemblages of planktonic foraminifers from Pleistocene to Paleocene age. Depth positions and age estimates of biostratigraphic marker events identified are shown in Table **T7.** The stratigraphic distribution of planktonic foraminifers is shown in Table **T8.**

The uppermost part of the interval between Sample 342-U1408A-1H-CC and 2H-4, 100–102 cm (4.33–9.80 mbsf), contains *Globorotalia truncatulinoides* and *Globorotalia inflata,* indicative of Pleistocene age. Samples 2H-5, 100–102 cm, and 2H-6, 100–102 cm (1.30–12.70 mbsf), contain poorly preserved assemblages containing no index markers except *G. inflata* and *Neogloboquadrina pachyderma,* suggesting an age of late Pliocene–Pleistocene. A poorly preserved Oligocene assemblage (mainly comprising *Catapsydrax* spp., *Dentoglobigerina galavisi, Globorotaloides suteri, Paragloborotalia nana,* and *Subbotina corpulenta*) was recovered from Samples 342-U1408A-2H-CC through 4H-3, 100–102 cm (13.82–27.30 mbsf).

Exceptionally well preserved and taxonomically diverse planktonic foraminifers of middle Eocene age were found in Samples 342-U1408A-4H-4, 100–102 cm, through 12H-CC (28.8–108.48 mbsf). The upper portion of this middle Eocene sequence is assigned to Zone E13. The top of *O. beckmanni* marks the top of Zone E12 in Sample 6H-CC (51.68 mbsf), with this species' base marking the base of Zone E12 in Sample 7H-4, 100–102 cm (51.68 mbsf). *O. beckmanni* (e.g., Fig. **F17**) has a comparatively short (~1.6–1.0 m.y.) total range that is concurrent with the MECO (Edgar et al., 2010), a prominent global warming event that interrupted the long-term Eocene cooling trend (Bohaty et al., 2009; Edgar et al., 2010). In addition to *O. beckmanii* and its descendant *Orbulinoides "superbeckmanni,"* which is characterized by a completely spherical test (Fig. **F17**) (Sample 342-U1408A-6H-CC; 51.68 mbsf), Zone E12 also contains abundant and extremely well preserved specimens of *Hantkenina* spp. and globigerine forms with spines preserved in the apertural opening.

The top of *Guembelitrioides nuttalli* in Sample 342-U1408A-9H-3, 100–102 cm (74.8 mbsf), indicates the base of Zone E11. The top of the morphologically distinctive *Morozovella aragonensis* marks the base of Zone E10 in Sample 16H-2, 100–102 cm (138.51 mbsf). The base of *Globigerinatheka kugleri* occurs in Sample 342-U1408A-18H-6, 100–102 cm (163.33 mbsf), and marks the base of Zone E9. The base of *G. nuttalli* in Sample 24X-CC (215.82 mbsf) marks the base of Zone E8.

The interval from Sample 342-U1408A-25X-2, 100–102 cm, through 25X-CC (220.2–227.24 mbsf) contains planktonic foraminifers from Zones E7–E5. The poorly preserved planktonic foraminifers in Samples 25X-6, 80–82 cm, through 25X-CC (226–227.24 mbsf) do not include any key marker species. Samples 342-U1408A-26X-CC through 27X-CC (232.33–246.54 mbsf) contain poorly preserved assemblages and span upper Paleocene Zones P5–P4 based on the marker species *Morozovella subbotinae* alongside other biostratigraphically useful taxa such as *Morozovella velascoensis, Morozovella occlusa, Morozovella aequa, Acarinina soldadoensis,* and *Subbotina velascoensis*. The PETM interval is not recognized above this upper Paleocene sequence.

Benthic foraminifers

Benthic foraminifers were examined semiquantitatively in core catcher samples from Hole U1408A. Additional working section half samples taken from Cores 342-U1408A-2H through 27X were examined for preservation and relative abundance of benthic foraminifers. Benthic foraminifers at this site are pre-

dominantly rare (the "present" category) relative to total sediment particles >150 µm in the Eocene and Paleocene and more abundant in the Oligocene and lower Eocene (Fig. F16; Table T9).

Preservation of benthic foraminifer tests is generally good to very good in the middle to upper Eocene to Paleocene, but the Oligocene and lower Eocene successions contain poorly to moderately preserved benthic foraminifers. The occurrences of benthic foraminifers at this site are shown in Tables T9 and T10.

Sample 342-U1408A-1H-CC yields a well-preserved Pleistocene fauna containing mainly *Bolivina* sp., *Cibicidoides* spp., *Pullenia* spp., and *Pyrgo* sp.

Samples 342-U1408A-2H-CC (13.87 mbsf) and 3H-CC (23.37 mbsf) include abundant Oligocene benthic foraminifers. The assemblage of Sample 2H-CC is dominated by the agglutinated taxon *Bathysiphon* sp., and calcareous taxa like *Bulimina* spp., *Cassidulina subglobosa, Dentalina* sp., and *Gyroidinoides* spp. Stilostomellids (including mainly *Stilostomella lepidula* and *Stilostomella subspinosa*) are subordinate (Table T10). The abundant occurrence of benthic foraminifers relative to total sediment particles and dominant occurrence of *Bathysiphon* sp. indicate intensive carbonate dissolution. Sample 342-U1408A-3H-CC (23.37 mbsf) is dominated by *C. subglobosa* and stilostomellids, indicating higher organic matter flux to the seafloor compared to Sample 2H-CC.

Samples 342-U1408A-4H-CC through 24X-CC (31.79–215.88 mbsf) yield a middle Eocene fauna characterized by the calcareous taxa *Anomalina* sp., *Anomalinoides* spp., *Bulimina* sp., *Cibicidoides* spp., *Dentalina* sp., *Nuttallides truempyi, Oridorsalis umbonatus,* and *Pullenia* spp. (including *Pullenia bulloides, Pullenia* cf. *jarvisi,* and *Pullenia quinqueloba*) and stilostomellids (Fig. F18). Agglutinated taxa are mainly represented by *Dorothia trochoides, Karreriella* sp., and *Valvulina spinosa*. Within the middle Eocene sequence, Samples 342-U1408A-7H-CC (61.94 mbsf) and 11H-CC (99.27 mbsf) show a dominance of infaunal taxa, such as *C. subglobosa* and stilostomellids, whereas epifaunal species are nearly absent. This pattern suggests high organic matter transport to the seafloor.

Sample 342-U1308A-25X-CC (227.29 mbsf) contains a lower Eocene assemblage represented by *Anomalinoides* sp., *Cibicidoides praemundulus, Dentalina* sp., *Lenticulina* sp., *N. truempyi,* and *O. umbonatus*. Benthic foraminifer preservation in this sample is moderate, probably because of the effect of dissolution related to the observed hiatus between lower and middle Eocene sediment.

Samples 342-U1408A-26X-CC (232.38 mbsf) and 27X-CC (246.59 mbsf) are represented by Paleocene taxa dominated by *Anomalina* sp., *Gavelinella beccariiformis,* and *N. truempyi*.

Paleomagnetism

We completed a paleomagnetism study of APC and XCB cores from Holes U1408A–U1408C with the primary objective of establishing a magnetostratigraphic age model for the site. The natural remanent magnetization (NRM) of each archive half section was measured at 2.5 cm intervals before and after demagnetization treatment in a peak alternating field (AF) of 20 mT for all cores from Hole U1408A, Cores 342-U1408B-1H through 18H, and Cores 342-U1408C-6H through 8H. For all other cores, we only measured NRM after 20 mT demagnetization. Archive half section measurement data were processed by removing data points from within 7.5 cm of section ends and from disturbed intervals described in the Laboratory Information Management System database. Cores 342-U1408A-1H through 20H, 342-U1408B-1H through 5H, and 342-U1408C-6H through 8H were azimuthally oriented using the FlexIT orientation tool (Table T11). All other cores were not oriented.

We also collected 168 discrete samples from working half sections to verify the archive half section measurement data and to measure the anisotropy of magnetic susceptibility (AMS) and the bulk susceptibility of Site U1408 sediment. Discrete samples were collected and stored in 7 cm^3 plastic cubes and typically taken from the least disturbed region closest to the center of each section from Hole U1408A. Selected samples were subjected to measurements of AMS, including bulk susceptibility, and NRM measurements after 20 mT AF demagnetization. Twenty-one samples were selected for stepwise demagnetization at 0, 10, 20, 30, 40, and 60 mT. All discrete sample data are volume corrected to 7 cm^3.

Results

Downhole paleomagnetism data after 20 mT demagnetization are presented for Holes U1408A, U1408B, and U1408C in Figures F19, F20, and F21, respectively. Similar to paleomagnetism results from previous Expedition 342 sites, section half measurement data from XCB-recovered cores are difficult to interpret because of biscuiting and substantial core disturbance. We chose to interpret only results obtained from APC cores except for a few cases in which discrete samples provide additional constraints on magnetozone identification in XCB-cored intervals.

We report the following three principal features in the paleomagnetism data at Site U1408. First, we observed intensity zonation that correlates with lithostratigraphy. Second, inclination values cluster at ~60° and 0° to –45°, a trend that is associated with clustering of declination values at ~0° and 180°, respectively. Third, an exceptionally detailed record of two successive Eocene geomagnetic field transitions is recorded over ~6 m of sediment.

Magnetic intensity zonation

Downhole magnetic intensity values vary with lithostratigraphic units. The uppermost ~13 m of sediment comprises Pleistocene–Oligocene clayey silt and nannofossil and foraminiferal ooze (see **"Lithostratigraphy"**) and is characterized by high magnetic intensity values (~10^{-2} A/m). The ~10 m thick Oligocene silty clay (with nannofossils) of lithostratigraphic Unit II has magnetic intensity values on the order of 10^{-4} A/m. The ~202 m of Oligocene to middle Eocene nannofossil clay, claystone, and nannofossil ooze of Unit III has intensity values that vary between 10^{-4} and 10^{-2} A/m. In detail, Unit III exhibits three main trends:

1. A consistently high intensity of ~10^{-2} A/m at ~30–110 mbsf, with high-amplitude variability from these mean values;
2. A steady downhole decrease in intensity from ~10^{-3} to ~10^{-4} A/m at ~110–150 mbsf, with second-order low-amplitude variability from the mean downhole trend; and
3. Intensity values of ~10^{-4} A/m at ~150–230 mbsf, with low-amplitude variability.

Finally, the lower Eocene to upper Paleocene nannofossil chalk with intermittent radiolarian-rich and chert-rich intervals of lithostratigraphic Unit IV (~225–246 mbsf) are characterized by consistently higher magnetic intensity values of ~10^{-3} A/m.

Downhole trends in magnetic intensity are similar to downhole trends in redox-sensitive interstitial water chemistry, particularly Mn and Fe (see **"Geochemistry"**). The peak in magnetic intensity in Unit III is observed in the same interval in which interstitial water iron concentrations are highest; decrease in intensity below this broad peak also follows a downhole decrease in interstitial water Fe concentrations. Sedimentation rate (see below), carbonate content, and lithostratigraphy (see **"Lithostratigraphy"**) remain constant over this interval, so we conclude that the first-order magnetic trends are a function of downhole dissolution of magnetic minerals rather than a change in provenance or a function of carbonate dilution. The higher frequency, lower amplitude variability, however, may reflect changes in carbonate content, sediment provenance, magnetic field strength, or a combination of these processes. Finally, we note that the first-order magnetic intensity at Site U1408 is high compared to previous sites studied during Expedition 342. This may be because magnetic dissolution is not as aggressive in sediment recovered from Site U1408 as it is at other sites; interstitial water sulfate concentrations remain high throughout the entire recovered interval (see **"Geochemistry"**).

Inclination and declination clustering

Inclination values following 20 mT AF demagnetization treatment often cluster around +60° and between 0 and –45°. Inclination clustering is usually associated with declination clustering at ~0° and 180°, respectively. The 0 to –45° inclinations are shallow with respect to the reversed polarity value expected at the ~40°N latitude of Site U1408. This shallow bias is readily attributed to a small normal polarity drilling overprint that remains after 20 mT AF demagnetization. AF demagnetization at 20 mT was most effective at removing the drilling overprint in the APC-recovered interval from ~140 to 180 mbsf; it was less effective between ~60 and 100 mbsf but sufficient to reveal reversed polarity magnetozones. We can utilize the positive and negative polarity clustering behavior to readily identify magnetozones in Site U1408 sediment.

Comparison between pass-through and discrete sample data

AF demagnetization results for 92 discrete samples are summarized in Table **T12.** Of the 21 samples treated with a peak AF demagnetization field of 60 mT, 12 reveal reasonably stable components of magnetization (e.g., Fig. **F22A, F22B**). These samples have remanent magnetizations that are strong enough to be measured by the onboard JR-6A spinner magnetometer. The remaining samples typically display NRM intensities that decrease by an order of magnitude following AF demagnetization in a 20 mT field. This behavior indicates that a drilling overprint probably obscures the primary magnetic signal. An example of such samples can be seen in Figure **F22C.** Nevertheless, these results are useful for verifying the 20 mT pass-through paleomagnetism data from the archive half sections.

In general, paleomagnetism data from archive half sections and discrete samples from oriented APC core intervals agree well. In contrast, discrete samples from XCB cores do not always show results that are consistent with the section half measurement data (Fig. **F19**). This discrepancy suggests that section half measurement data from XCB core intervals

should be interpreted with care, similar to our conclusions regarding paleomagnetism data from Sites U1403, U1406, and U1407.

Magnetostratigraphy

The shipboard downhole results reveal a series of normal and reversed magnetozones between Cores 342-U1408A-4H and 25X (~29–220 mbsf), between Cores 342-U1408B-5H and 18H (~30–154 mbsf), and between Cores 342-U1408C-5H and 19H (~35–165 mbsf). These magnetostratigraphies can be straightforwardly correlated among all three holes.

By utilizing radiolarian, foraminifer, and nannofossil biostratigraphic datums from Hole U1408A (see **"Biostratigraphy"**), we can correlate magnetozones to the geomagnetic polarity timescale (GPTS). The shipboard magnetostratigraphic age model is based on Hole U1408A, for which we have the most biostratigraphic datums. Extension of this age model to the magnetozonation observed in Holes U1408B and U1408C is contingent on the accuracy of the stratigraphic correlation between holes, which is corroborated by some lithologic horizons, biostratigraphic datums, and physical property features (see **"Stratigraphic correlation"**). Our correlation is presented in Table **T13** and in Figures **F19, F20, F21,** and **F23.**

In Hole U1408A, we correlated the magnetostratigraphy in Cores 342-U1408A-4H through 16H to lower Chron C17n.3n (~38.3 Ma) through upper Chron C20r (~43.4 Ma). Chron C20r is continuously recognized downhole to the bottom of the APC-recovered interval (i.e., bottom of Core 342-U1408A-20H). Continuous downhole negative inclinations indicative of reversed polarity are recognized in archive half section and discrete samples from XCB-cored sediment downhole to Core 342-U1408A-24X. The transition from negative to positive inclinations between 211.59 and 212.60 mbsf in Core 24X is correlated to the Chron C20r/C21n boundary (45.724 Ma). Magnetozone correlations for Holes U1408B and U1408C are similar to Hole U1408A, with the exception that we did not interpret the XCB-cored intervals because we did not have paleomagnetism data from discrete samples to verify the data from archive half sections.

The correlations described above provide a shipboard chronostratigraphic framework for interpreting the middle Eocene sediment record at Site U1408. The most salient implication of this age model is that sedimentation rates along the Southeast Newfoundland Ridge at the paleowater depth of Site U1408 varied between ~1.5 and 3.14 cm/k.y. across the middle Eocene (Fig. **F15**). Average linear sedimentation rates were higher before the MECO (~41.5 Ma) than after.

Detailed record of a geomagnetic field transition

The geomagnetic field transitions from Chrons C18n.1n to C18n.1r to C18n.2n are recorded in exceptional detail in all three holes at Site U1408. In Hole U1408A, the Chron C18n.1n–C18n.1r transition is recorded from ~47 to 51 mbsf. In Hole U1408C, the Chron C18n.1r–C18n.2n transition is recorded from ~50 to 55 mbsf. Both transitions are recorded in Hole U1408B from ~50 to 57 mbsf. See Table **T13** for precise locations of the transitions in each hole. Variations in declination, inclination, and intensity during the transitions are illustrated in Figure **F24.** Magnetic field behavior is very coherent between all three holes.

Detailed sediment records of the most recent magnetic field transition (i.e., the Matuyama–Brunhes transition [0.781 Ma]) show that magnetic directions flip several times and intensity values oscillate while the geomagnetic field transitions between stable polarity states (e.g., Yamazaki and Oda 2001; Valet et al., 2005). We observe similar paleomagnetism behavior during the Chron C18 series transitions recorded in all three holes (Fig. **F24**). We note that some of the variation in NRM that remains after 20 mT demagnetization may reflect not only geomagnetic field intensity but also changes in magnetic mineralogy, concentration, grain size, or a combination of these factors. A thorough shore-based paleomagnetism and rock magnetic study is necessary to fully characterize and understand the geomagnetic field transition behavior. Cyclostratigraphic analysis of physical properties in this interval may provide constraints on the duration of these Eocene field reversals.

Magnetic susceptibility and anisotropy of magnetic susceptibility

Bulk magnetic susceptibility measured on 94 discrete samples is summarized in Table **T14.** Although discrete samples were collected from each core section from the entire depth of Hole U1408A, we chose to measure only odd-numbered samples. Downhole variation in whole-round magnetic susceptibility (WRMS) and discrete sample magnetic susceptibility (DSMS) for Hole U1408A are shown in Figure **F19.** The WRMS data for Hole U1408A are shown in raw form; they have not been trimmed at section ends or filtered for obvious outliers, so noise in the data probably reflects edge effects or spurious measure-

ments. We multiplied the WRMS data, which are in instrument units (IU), by a factor of 0.577×10^{-5} to convert to approximate SI volume susceptibilities (see **"Paleomagnetism"** in the "Methods" chapter [Norris et al., 2014a]). WRMS and DSMS data agree very well after this conversion, and we attribute small absolute differences to the fact that the conversion factor applied to the WRMS data is not constant downhole because of changes in core diameter and density; only discrete samples provide calibrated susceptibility values in SI units. Both magnetic susceptibility data sets show the same first- and second-order cyclic trends, indicating that these trends are robust features of Site U1408 sediment.

AMS results for the discrete samples are also summarized in Table **T14** and are shown in Figure **F25.** The eigenvalues associated with the maximum (τ_1), intermediate (τ_2), and minimum (τ_3) magnetic susceptibilities at Site U1408 show some downhole variations that correspond to changes in lithostratigraphy. We also observed a distinct change in AMS values at the transition from APC to XCB coring technologies, with greater divergence between principal eigenvalues, consistently greater anisotropy, and a trend toward steeper inclinations of the minimum principal eigenvector (V_3) in XCB-recovered intervals.

Triaxial fabrics are greatest, and most variable, in lithostratigraphic Unit III. Magnetic fabrics, reflected in the V_3 inclination, lineation (τ_1/τ_2), and foliation (τ_2/τ_3) values, are greatest between ~90 and 180 mbsf. This interval also corresponds to the greatest sedimentation rates calculated for Site U1408 (3.14 cm/k.y.) (Fig. **F15**) and a zone of nannofossil clay with lower carbonate content compared to the nannofossil ooze lithostratigraphy above and below this interval.

Age-depth model and mass accumulation rates

At Site U1408, we recovered a 250 m thick sequence of Pleistocene to upper Paleocene clayey nannofossil ooze with varying amounts of clay and nannofossils. A condensed Pleistocene to upper Eocene section overlies a middle Eocene through upper Paleocene succession with significant hiatuses between the Oligocene and middle Eocene (~7 m.y.) and between the middle and lower Eocene (~3 m.y.) and a minor hiatus or condensed interval around the Paleocene/Eocene boundary. Sedimentation rates are high (~1.39–3.03 cm/k.y.) through the middle Eocene, low (~0.08 cm/k.y.) through the lower Eocene, and relatively high (~1.27 cm/k.y.) through the upper Paleocene.

Biostratigraphic datums and magnetostratigraphic datums from Hole U1408A (Table **T15**) were compiled to construct an age-depth model for this site (Fig. **F15**). A selected set of datums (Table **T16**) was used to create an age-depth correlation and calculate linear sedimentation rates (LSRs). Total mass accumulation rate (MAR), carbonate MAR (CAR), and noncarbonate MAR (nCAR) were calculated at 0.2 m.y. intervals using a preliminary shipboard splice rather than the sampling splice described in this volume (Table **T17;** Fig. **F26**).

Age-depth model

The age-depth model is tied to Pleistocene to upper Eocene nannofossil datums in the upper 38 m of Hole U1408A. Through the middle Eocene, paleomagnetic datums are used as the primary tie points. These datums are closely aligned to nannofossil datums and are also in good agreement with the more sparse radiolarian and foraminifer datums. Nannofossil datums are the primary tie points from the lower middle Eocene to Paleocene and are in good agreement with foraminifer and radiolarian datums.

Linear sedimentation rates

Below the condensed Pleistocene–Oligocene interval in the upper 38 mbsf, LSRs in Hole U1408A are high (2–3 cm/k.y.) in the middle Eocene and moderately high (1.27 cm/k.y.) in the Paleocene. The intervening Eocene section is highly condensed, with an average LSR of <0.1 cm/k.y.

Mass accumulation rates

MARs range from <0.1 g/cm²/k.y. in the Pleistocene to lower Oligocene to higher values of 4.0 g/cm²/k.y. in the middle Eocene and 1.5 g/cm²/k.y. in the Paleocene. CAR and nCAR are roughly equal during the middle Eocene. Carbonate accumulation dominates mass accumulation during a peak in MAR during the Paleocene.

Geochemistry

The shipboard geochemistry program during operations at Site U1408 included

- Analysis of interstitial gas compounds on headspace samples;
- Measurement of minor and trace element concentrations in interstitial water squeezed from whole-round samples from Hole U1408A; and

- Inorganic carbon, total carbon, and total nitrogen determinations of solid sediment samples from multiple holes.

Headspace gas samples

Headspace gas samples for routine safety monitoring were collected at a typical frequency of one sample per core in Hole U1408A (Table T18), usually in the bottom half of each core (i.e., Section 4, 5, or 6). Methane was the only hydrocarbon detected in measurable amounts. Methane concentrations increase from 1.9 to 5.9 ppmv in the upper 150 mbsf of Hole U1408A. After reaching peak concentrations at 150 mbsf, methane decreases to 2.1 ppmv between 150 and 260 mbsf.

Interstitial water samples

Twenty-six interstitial water samples were squeezed from whole-round samples taken at a typical frequency of one per core in Hole U1408A (Table T19). Whole-round samples were collected immediately after the cores were sectioned on the catwalk. In some cases, disturbed cores or low recovery precluded whole-round sampling, as in the case with Core 342-U1408A-22X, which was too disturbed for collection of a whole-round sample.

Results

Salinity, pH, alkalinity, ammonium, manganese, iron, and sulfate

The interstitial fluid profiles of sulfate, alkalinity, and ammonium in Hole U1408A reflect typical changes associated with organic carbon cycling (Fig. F27). The downhole pH and salinity profiles are near uniform with no substantial inflections. In contrast, alkalinity shows strong increases downhole, from <3.3 mM in the uppermost 50 mbsf to a maximum of ~5.5 mM at 150–180 mbsf and then declining to ~4.5 mM at the base of the recovered section. Chloride and sodium show very limited variations in interstitial water, with very slight overall decreasing trends downhole.

Manganese concentrations decrease rapidly with depth in lithostratigraphic Units I and II (see "Lithostratigraphy") to 30 mbsf and then increase gradually to a maximum value of 10 µM at 135 mbsf. The downhole trend reverses below this depth and decreases to 2 µM at the bottom of the recovered sequence.

Iron concentrations show three distinct peaks in the recovered sequence. First, there is a broad peak from 50 to 90 mbsf with maximum concentrations of 30–40 µM. The second and third peaks occur at 135 and 190 mbsf with concentrations reaching 20 µM in both instances.

Sulfate concentrations are 30 mM near the top of the recovered sequence. The downhole profile shows gently decreasing sulfate concentrations with no major inflections or correlations to lithostratigraphic unit boundaries. Overall, the sulfate concentrations at Site U1408 are high (average = 26.9 mM), suggesting that the influence of organic matter respiration within the sediment column at Site U1408 is modest.

The downhole ammonium profile is more variable than that documented at previous Expedition 342 sites. It is possible, however, to discern two main maxima, one at 25 mbsf (40 µM) and another at 175 mbsf (78 µM).

Calcium, magnesium, sodium, chloride, boron, and potassium

Calcium concentrations in Hole U1408A show an increasing downhole trend in the upper 180 mbsf. Below this depth, the downhole calcium concentration profile becomes more or less uniform at ~16 mM.

Magnesium and potassium concentrations show decreasing downhole trends in the upper 180 mbsf. Below this depth, the downhole magnesium concentration profile becomes more or less uniform at 45 mM. Mg/Ca ratios show a remarkably gentle decline to 180 mbsf, where the ratios become uniform at ~2.8.

Sodium and chloride concentrations range from 460 to 470 mM and 520 to 560 mM, respectively, and are highly variable, with no discernible downhole trends that correspond to lithostratigraphic units.

Boron concentrations are ~400 µm in lithostratigraphic Units I and II and then increase to a broad maximum of 480 µm. Between 20 and 70 mbsf, boron concentrations show an overall downhole decrease to 310 µm at 205 mbsf.

Discussion

The downhole patterns of alkalinity, manganese, and iron suggest two zones of organic matter degradation within the recovered sequence. The typical succession of electron acceptor use during early diagenesis is manganese, followed by iron then sulfate (cf. Berner, 1980). Elevated concentrations of manganese coupled with iron concentrations of 0 µM within the uppermost 30 mbsf of the sediment column indicate ongoing oxic to suboxic diagenesis driven by microbial reduction of ferromanganese oxide. Below 30 mbsf, the reduction of iron oxide is evident from the rapid increase in iron concentrations. The broad peak in iron between 40 and 90 mbsf sug-

gests a locus of modest organic matter consumption within this depth. Little change in sulfate concentrations and increasing alkalinity concentrations beginning at 50 mbsf corroborate this interpretation.

Increasing manganese concentrations below 30 mbsf point to the existence of a deeper manganese source. Further reduction of ferromanganese oxide occurs deeper in the sequence, likely around 120–130 mbsf, where interstitial water iron concentrations peak at 125 and 190 mbsf. This portion of the sequence would appear to be a reservoir of relatively high organic carbon contents (Fig. **F28**), and the interstitial fluid profiles reflect the diffusional signal following the degradation of this reservoir, but the interstitial water sulfate profile shows that this reservoir is not a zone of active sulfate reduction. It is also possible that these strata are richer in ferromanganese oxide.

Site U1408 downhole trends in potassium, calcium, magnesium, and Mg/Ca ratios reflect diffusion profiles resulting from calcium-magnesium exchange associated with alteration of volcanic basement (Gieskes and Lawrence, 1981), with potassium and magnesium decreasing and calcium slightly increasing with depth (Fig. **F27**). Inflections in calcium and alkalinity at ~180 mbsf indicate possible dissolution/reprecipitation of carbonate, which is high in the nannofossil chalk that comprises the basal lithostratigraphic Unit IV (see **"Lithostratigraphy"**).

Laboratory experiments under regulated temperatures and pressures have shown that boron is leached from terrigenous sediment into fluids (James et al., 2003), and a study of Ocean Drilling Program Leg 186 interstitial water samples concluded that boron removal from clays and volcanic ash accounted for boron enrichment in interstitial water (Deyhle and Kopf, 2002). Therefore, the broad downhole peak in interstitial water boron concentrations at 20–70 mbsf at Site U1408 presumably indicates increased supply from the terrigenous sediment components in lithostratigraphic Units II and III (see **"Lithostratigraphy"**).

Sediment samples

Sediment plugs (5 cm^3) for downhole analysis of sediment elemental geochemistry were taken from Cores 342-U1408A-1H through 27X at an average resolution of one sample per section, adjacent to the moisture and density (MAD) samples (Table **T20**).

Results

Concentrations of inorganic carbon vary from 0.12 to 10.9 wt% in Hole U1408A (Table **T19;** Fig. **F28**). These concentrations are equivalent to 0.6 to 90.5 wt% $CaCO_3$, assuming that all of the carbonate is calcite. Total organic carbon (TOC) values are typically 0–0.5 wt%, excluding data from the 30.96–89.44 mbsf interval, which were run with a different calibration standard and thus show much higher (>1 wt%) and very likely incorrect values. Of the data plotted, TOC contents are slightly higher (0.4 wt%) in the 100–150 mbsf interval than in the underlying and overlying sediment. Total nitrogen values range from 0 to 0.15 wt%.

Carbonate concentrations are roughly 40 wt% in lithostratigraphic Unit I and decrease to 0–10 wt% in Unit II, which is consistent with low carbonate levels observed in other Oligocene age sequences recovered during Expedition 342. In the expanded middle Eocene sequence represented by Unit III, carbonate content values are 40–50 wt%, with a few peaks to 80–90 wt%. Carbonate increases to 90 wt% in Unit IV, which corresponds to early Eocene sediment.

Discussion

Moderately high carbonate contents throughout the recovered sequence are consistent with the relatively shallow paleodepth of the site throughout the Eocene. The most prominent change in carbonate content is a step increase associated with the downhole transition from dominantly nannofossil clay to nannofossil chalk at the lithostratigraphic Unit III/IV boundary (from ~50 to >80 wt% $CaCO_3$; ~225 mbsf). This step increase is typical of the pattern seen in lower to middle Eocene boundary sequences recovered at Expedition 342 sites and reflects a transition from pelagic chalk sedimentation to clay deposition in the initial stages of sediment drift development. An unconformity is present between middle Eocene sediment of Unit III and lower Eocene sediment of Unit IV, precluding further interpretation at this stage.

Physical properties

We made physical property measurements on whole-round sections, section halves, and discrete samples from section halves. Gamma ray attenuation (GRA) bulk density, magnetic susceptibility, *P*-wave velocity, and natural gamma radiation (NGR) measurements were made on whole-round sections using the Whole-Round Multisensor Logger (WRMSL). Thermal conductivity was measured on one section per core for Cores 342-U1408A-1H through 10H. Compressional wave velocity on section halves was also measured at a frequency of two in each section (at ~50 and 100 cm) using a *P*-wave caliper (PWC). For MAD analyses, one discrete sample was collected in each section (typically at ~35 cm from the top of a section). The Section Half Multisensor Logger was

used to measure spectral reflectance and magnetic susceptibility on archive half sections.

Magnetic susceptibility

Overall, magnetic susceptibility ranges from 0 to 160 IU (Fig. F29). From the top of the sediment column at Site U1408 to ~12 mbsf (lithostratigraphic Unit I; see "Lithostratigraphy"), magnetic susceptibility is characterized by high values and varies in magnitude between 40 and 160 IU. At the contact with underlying Unit II, magnetic susceptibility decreases sharply to ~10 IU. Magnetic susceptibility throughout Units II–IV remains constant and averages 14 IU. In Unit III, two superimposed sharp peaks appear and correlate among all three holes. The first peak (~25 IU) occurs just below the transition between Units II and III at ~30 mbsf. The second peak, with a magnitude of ~60 IU in Holes U1408A and U1408C and ~40 IU in Hole U1408B, occurs at ~60 mbsf. In all three holes between ~80 and 115 mbsf, magnetic susceptibility data show pronounced variability associated with distinct color cycles. Cycles in magnetic susceptibility also occur between ~140 and 170 mbsf in all holes.

Density and porosity

Two methods were used to evaluate bulk density at Site U1408. The GRA density method provided a bulk density estimate from whole-round sections. The MAD method applied to 173 discrete samples gave a second, independent measure of bulk density, as well as dry density, grain density, water content, and porosity from discrete samples.

Overall, bulk density values vary between 1.4 and 1.95 g/cm^3 (Fig. F29). MAD bulk density values are on average ~3% lower than GRA bulk density downhole to 180 mbsf. Below ~180 mbsf, the offset increases to 5% as a result of the change in coring method from APC to XCB. In lithostratigraphic Unit I, bulk density increases from 1.5 to 1.75 g/cm^3. An abrupt decrease to ~1.4 g/cm^3 occurs at the contact with underlying Unit II; this change correlates with the transition between clayey silt, nannofossil foraminiferal ooze, and nannofossil clay with silt (see "Lithostratigraphy"). Bulk density throughout Units II and III increases downhole at Site U1408 to ~1.95 g/cm^3 at ~225 mbsf. In Holes U1408B and U1408C, this trend toward higher values changes to more constant values that average 1.8 g/cm^3 at 75 mbsf. Between 225 mbsf and the bottom of Hole U1408A, bulk density decreases from 1.9 to 1.6 g/cm^3.

Water content and porosity vary between 20 and 60 wt% and between 45 and 80 vol%, respectively, throughout Site U1408. Water content and porosity show greater variability in Units I and II than in underlying sediment. Throughout Unit III (below 22 mbsf), both of these properties decrease gradually downhole from 50 to 25 wt% for water content and from 75 to 50 vol% for porosity. In Unit IV, water content and porosity both increase downhole to ~55 wt% and ~65 vol%, respectively, at the bottom of the hole.

Throughout Hole U1408A, grain density remains relatively constant and averages 2.77 g/cm^3. Units I and II are characterized by higher amplitude variability in grain density (2.6 and 2.9 g/cm^3) than Unit III (2.7 and 2.8 g/cm^3). Unit IV is characterized by a downhole decrease in grain density from 2.8 to 2.68 g/cm^3 at the bottom of the hole.

P-wave velocity

P-wave velocity was measured with the *P*-wave logger (PWL) on all whole-round sections and by the PWC on undisturbed section halves from Holes U1408A–U1408C. Whole-round and section-half data track each other well, but PWC values are consistently lower than PWL values by ~18 m/s (Fig. F30). Overall, *P*-wave velocity gradually increases downhole from 1500 to 1800 m/s, which we attribute to downhole compaction; bulk density and water content show similar trends. *P*-wave velocities are slightly higher in lithostratigraphic Unit I than in the upper part of Unit II, which corresponds to the transition between clayey silt, nannofossil foraminiferal ooze, and nannofossil clay with silt (see "Lithostratigraphy"). We did not complete PWL measurements for the lower part of Unit III and all of Unit IV, because sediment rarely filled the liner in these intervals, a consequence of coring soft chalks with the XCB. PWC-measured velocities increase to 1900 m/s in the nannofossil chalk and thin chert layers associated with Unit IV.

Natural gamma radiation

NGR was measured on the whole-round sections in Holes U1408A–U1408C. NGR values range from 10 to 55 cps in all three holes (Fig. F30). In lithostratigraphic Unit I, NGR data show large variations between 15 and 55 cps, with the largest values occurring at the peak defining the contact between Units I and II. NGR values increase from ~20 to ~30 cps in Unit II and reach ~40 cps at the top of Unit III (~22 mbsf). The upper part of Unit III (between 22 and 40 mbsf) is characterized by a trend toward lower values, from 40 to 25 cps. Between ~40 and 225 mbsf, the NGR trend remains constant, with an average of ~25 cps, significant low-amplitude variability

throughout, and several larger peaks and troughs (see "Stratigraphic correlation"). NGR values decrease from 25 to 5 cps at the contact between Units III and IV and remain low to the bottom of the hole.

Color reflectance

Color reflectance was measured on archive section halves from Holes U1408A–U1408C. Four general trends can be defined in all three holes (Fig. F31). In lithostratigraphic Unit I, values show relatively large fluctuations between 3.5 and 8 for a* and from 3 to 10 for b*. In Unit II, a* has decreased, constant values of 2.2 and b* decreases from ~11 to ~8. The change in color reflectance across the Unit I/II boundary is associated with the transition from brown and gray clayey silt and nannofossil foraminiferal ooze to pale yellow and light gray nannofossil clay with silt (see "Lithostratigraphy"). At the transition between Units II and III at ~22 mbsf, distinct decreases occur in a* (from 2 to –1) and b* (from 4.5 to 2). These decreases correspond to the transition from yellow, pale brown, and greenish gray sediment. Throughout Unit III, color reflectance parameters a* and b* remain constant downhole (a* averages 0.5 and b* averages –0.35). Two superimposed peaks that correlate among all three holes occur at ~30 and ~135 mbsf. In Hole U1408A at the top of Unit IV (230 mbsf), a pronounced step occurs where a* and b* increase from –1 to 2.2 and from –1 to 1.75, respectively. These changes correlate to increases in water content and in radiolarian content and decreases in bulk density and NGR. This step also correlates to the transition from greenish gray to light greenish gray nannofossil oozes to underlying pinkish brown nannofossil oozes.

The peaks in a* and b* at 115 mbsf in Hole U1408A and at 85 mbsf in Hole U1408C are spurious measurements attributable to technical problems during data collection.

L* corresponds to sediment brightness and generally follows pronounced lithostratigraphic changes (Fig. F31). L* records show similar trends in all three holes. In lithostratigraphic Unit I, L* values average 53 and abruptly increase to 65 in Unit II, clearly recording the transition from brown and gray clayey silt and nannofossil foraminiferal ooze to pale yellow and light gray nannofossil clay with silt (see "Lithostratigraphy"). From ~15 mbsf to the bottom of Unit II, L* values decrease to 45 and remain constant throughout Unit III with an average value of 54, although distinctive peaks in all three holes are observed at ~95 and ~155 mbsf. At the top of Unit IV, L* values increase to 80 and remain high but variable to the bottom of the hole. The major variations in L* values recorded at Site U1408 appear to correlate with changes in calcium carbonate content (see "Geochemistry").

Thermal conductivity

Thermal conductivity was measured on Section 3 in Cores 342-U1408A-1H through 10H, usually near the middle of the section (~75 cm), using the full-space probe (Table T21). Thermal conductivity increases downhole from ~1.0 to 1.2 W/(m·K) and follows an approximately linear trend (Fig. F32). Thermal conductivity measurements show some correlation with bulk density (R^2 = ~0.61) (Fig. F33). Thermal conductivity increases downhole as porosity decreases, which we attribute to lower interstitial spacing that attenuates the applied heat from the probe.

Stratigraphic correlation

Sampling splice

Clear signals in shipboard magnetic susceptibility and shore-based X-ray fluorescence (XRF) core scanning measurements of the ratio of calcium to iron resulted in a continuous splice at Site U1408 downhole to ~234 m core composite depth below seafloor (CCSF). The expression of orbital obliquity (and/or precession) cycles between ~35 and ~220 m CCSF aided correlation and splice construction. Hole U1408A is the deepest hole drilled at this site and reaches a maximum depth of ~247 mbsf (~274 m CCSF). Holes U1408B and U1408C extend to ~212 mbsf (~233 m CCSF) and ~187 mbsf (~204 m CCSF), respectively. The overall trends and patterns in physical properties are very similar among the three holes; however, tentative tie points still exist in the splice below ~175 m CCSF, where features in the data sets analyzed are less distinctive and show lower amplitude variability. We denote tentative offsets and tie points in the affine and splice tables. We are most confident in the upper ~175 m CCSF of the correlation and consider this interval of the splice most appropriate for high-resolution sampling (Fig. F34). Our correlation yields a growth rate of 13% for Hole U1408A, 6% for Hole U1408B, and 5% for Hole U1408C. We mainly attribute the larger growth rate for Hole U1408A to core expansion and the slightly thicker sedimentary sequence compared to Holes U1408B and U1408C (Fig. F35).

Correlation during drilling operations

Using WRMSL magnetic susceptibility data generated on cores from Hole U1408A and Special Task Multisensor Logger (STMSL) magnetic susceptibility data generated on cores from Holes U1408B and

U1408C, we were able to correlate among holes during drilling operations. The WRMSL data were generated on cores equilibrated to room temperature, whereas the STMSL data were generated on cores immediately after curation. We guided drilling operations to make depth adjustments while drilling Holes U1408B and U1408C to correct for short cores and missed intervals in Holes U1408A and U1408B. Clear cycles in sediment color and composition are present in the magnetic susceptibility data of the Pleistocene cover (0–15 m CCSF) and the middle Eocene drift deposits (35–225 m CCSF). These cycles, together with large step changes and trends in the physical property records, made correlation during drilling operations possible.

During drilling operations at Site U1408, weather conditions were favorable and ship heave was insignificant. A clear mudline and a Pleistocene cover of even thickness were recovered in all three holes, indicating a uniform seabed with minimal lateral variability in the uppermost part of the sequence. These clear tie points allowed for quick depth adjustments in Holes U1408B and U1408C in order to offset core gaps among the three holes. In Hole U1408B, we advanced without coring by 3 m at ~28 m CCSF, and in Hole U1408C we advanced without coring by 3 m at 9 m CCSF. Prior to shooting Core 342-U1408C-12H, we pulled up by 2.5 m to prevent alignment of core gaps with Holes U1408A and U1408B; we regard the upper part of this core (the excess recovery) as fall-in.

Correlation and splice construction

The shipboard composite depth scale and splice for Site U1408 were primarily based on WRMSL magnetic susceptibility data (see **"Physical properties"**). We also analyzed core photographs, NGR, and GRA bulk density data as additional lines of evidence for a few tie points. Cyclic variations were recognized in magnetic susceptibility and color reflectance data as well as by visual analysis of split core sections. Given heavy high-resolution sampling requests for Eocene material from Site U1408, we also collected shore-based Ca/Fe measurements using the Avaatech XRF core scanner at Scripps Institution of Oceanography in order to verify and/or adjust splice tie points. We scanned the archive halves of cores along the splice from ~17 to ~234 m CCSF. In order to check the splice, we also scanned additional intervals adjacent to tie points. Where tie points were tentative based on our analysis of shipboard data or fell in disturbed cores, we scanned additional material. XRF core scanning allowed for a few modifications to the originally selected tie points and also allowed us to verify tie points previously considered tentative. All remaining tentative tie points (Tables **T22, T23**) are the result of inconclusive XRF core scanner data as well as shipboard physical properties.

We defined Core 342-U1408B-1H as the anchor in the splice because it is the most representative mudline core recovered (Fig. **F34**). Pleistocene cover with very clear cyclic variability in lithostratigraphy and magnetic susceptibility is present between 0 and 15 m CCSF. Between ~15 and ~35 m CCSF, a very condensed Miocene through late Eocene sequence is present, with much lower magnetic susceptibility values compared to the Pleistocene cover. However, values are still above the noise level and sufficiently recognizable patterns enable correlation in this interval. The correlation between ~35 and ~175 m CCSF is also robust because color and lithologic cycles provide clear tie points and depth control across this interval of high sedimentation rates (see **"Age-depth model and mass accumulation rates"**). We consider the splice for this interval of the middle Eocene drift deposit sufficient for high-resolution sampling. The interval below ~175 m CCSF to the bottom of the Site U1408 splice at ~234 m CCSF has a large number of tentative ties. In this interval, the magnetic susceptibility pattern is different among the three holes, particularly in Hole U1408B between ~150 and ~205 m CCSF as compared to Holes U1408A and U1408C. However, we were able to use XRF Ca/Fe measurements to verify tie points downhole to ~175 m CCSF, and in general Ca/Fe are more similar between holes below this interval compared to magnetic susceptibility data. The stratigraphic interval recovered by Cores 342-U1408A-24X through 27X was not recovered in Holes U1408B and U1408C. These cores are therefore appended.

APC disturbance of cores across holes at Site U1408 results in relatively strong variability in compression and extension along the length of the cores. This is apparent in the varying spacing between, or thickness of, equivalent lithologic cycles. GRA density data often show an increase along the length of cores, indicating that the bottoms of cores are more compressed compared to the relatively expanded core tops.

Downhole logging

Heat flow

Heat flow at Site U1408 was determined according to the procedure of Pribnow et al. (2000). Four temperature measurements were made in Hole U1408A using the advanced piston corer temperature tool (APCT-3), including a measurement of the mudline temperature at the seafloor. The deployment during Core 324-U1408-4H was lost when the APCT-3 failed to

couple properly with the formation and the recorded data could not be used.

Measured heat flow values ranged from 5.1°C at 61.3 m drilling depth below seafloor (DSF) to 7.39°C at 118.3 m DSF (Table **T24**), giving a geothermal gradient of 39.2°C/km (Fig. **F36**). The seafloor temperature was 2.72°C based on the average of the four minimum temperature values in the APCT-3 temperature profiles. Thermal conductivity measured in the laboratory was converted to in situ values using the method of Hyndmann et al. (1974) (see **"Physical properties"** in the "Methods" chapter [Norris et al., 2014a]). The calculated in situ values are ~2.5% lower than the measured laboratory values. Considering the variations in thermal conductivity with depth, a measure of heat flow in a conductive regime can be given by a "Bullard plot." Thermal resistance is calculated by cumulatively adding the inverse of the in situ thermal conductivity values over depth intervals downhole. If the thermal regime is purely conductive, the heat flow will be the slope of the temperature versus the thermal resistance profile (Bullard, 1939). The thermal resistance calculated over the intervals overlying the APCT-3 measurements is shown in Table **T24,** and the resulting linear fit of the temperature gives a heat flow value of 43.4 mW/m^2, which is a typical value for the ocean floor.

References

Berner, R.A., 1980. *Early Diagenesis: A Theoretical Approach:* Princeton, NJ (Princeton Univ. Press).

Bijl, P.K., Houben, A.J.P., Schouten, S., Bohaty, S.M., Sluijs, A., Reichart, G.-J., Sinninghe Damsté, J.S., and Brinkhuis, H., 2010. Transient middle Eocene atmospheric CO_2 and temperature variations. *Science,* 330(6005):819–821. **doi:10.1126/science.1193654**

Bohaty, S.M., Zachos, J.C., Florindo, F., and Delaney, M.L., 2009. Coupled greenhouse warming and deep-sea acidification in the middle Eocene. *Paleoceanography,* 24(2):PA2207. **doi:10.1029/2008PA001676**

Bullard, E.C., 1939. Heat flow in South Africa. *Proc. R. Soc. A,* 173(955):474–502. **doi:10.1098/rspa.1939.0159**

Deyhle, A., and Kopf, A., 2002. Strong B enrichment and anomalous $\delta^{11}B$ in pore fluids from the Japan Trench forearc. *Mar. Geol.,* 183(1–4):1–15. **doi:10.1016/S0025-3227(02)00186-X**

Edgar, K.M., Wilson, P.A., Sexton, P.F., Gibbs, S.J., Roberts, A.P., and Norris, R.D., 2010. New biostratigraphic, magnetostratigraphic and isotopic insights into the Middle Eocene Climatic Optimum in low latitudes. *Palaeogeogr., Palaeoclimatol., Palaeoecol.,* 297(3–4):670–682. **doi:10.1016/j.palaeo.2010.09.016**

Foreman, H.P., 1973. Radiolaria of Leg 10 with systematics and ranges for the families Amphipyndacidae, Artostrobiidae, and Theoperidae. *In* Worzel, J.L., Bryant, W., et al., *Init. Repts. DSDP,* 10: Washington, DC (U.S. Govt. Printing Office), 407–474. **doi:10.2973/dsdp.proc.10.118.1973**

Gieskes, J.M., and Lawrence, J.R., 1981. Alteration of volcanic matter in deep-sea sediments: evidence from the chemical composition of interstitial waters from deep sea drilling cores. *Geochim. Cosmochim. Acta,* 45(10):1687–1703. **doi:10.1016/0016-7037(81)90004-1**

Gradstein, F.M., Ogg, J.G., Schmitz, M.D., and Ogg, G.M. (Eds)., 2012. *The Geological Time Scale 2012:* Amsterdam (Elsevier).

Hyndman, R.D., Erickson, A.J., and Von Herzen, R.P., 1974. Geothermal measurements on DSDP Leg 26. *In* Davies, T.A., Luyendyk, B.P., et al., *Init. Repts. DSDP,* 26: Washington, DC (U.S. Govt. Printing Office), 451–463. **doi:10.2973/dsdp.proc.26.113.1974**

James, R.H., Allen, D.E., and Seyfried, W.E., Jr., 2003. An experimental study of alteration of oceanic crust and terrigenous sediments at moderate temperatures (51 to 350°C): insights as to chemical processes in near-shore ridge-flank hydrothermal systems. *Geochim. Cosmochim. Acta,* 67(4):681–691. **doi:10.1016/S0016-7037(02)01113-4**

Kamikuri, S., Moore, T.C., Ogane, K., Suzuki, N., Pälike, H., and Nishi, H., 2012. Early Eocene to early Miocene radiolarian biostratigraphy for the low-latitude Pacific Ocean. *Stratigraphy,* 9(1):77–108. **http://www.micropress.org/micropen2/articles/1/7/27546_articles_article_file_1785.pdf**

Kirschvink, J.L., 1980. The least-squares line and plane and the analysis of palaeomagnetic data. *Geophys. J. R. Astron. Soc.,* 62(3):699–718. **doi:10.1111/j.1365-246X.1980.tb02601.x**

Lyle, M., Wilson, P.A., Janecek, T.R., et al., 2002. *Proc. ODP, Init. Repts.,* 199: College Station, TX (Ocean Drilling Program). **doi:10.2973/odp.proc.ir.199.2002**

Norris, R.D., Wilson, P.A., Blum, P., Fehr, A., Agnini, C., Bornemann, A., Boulila, S., Bown, P.R., Cournede, C., Friedrich, O., Ghosh, A.K., Hollis, C.J., Hull, P.M., Jo, K., Junium, C.K., Kaneko, M., Liebrand, D., Lippert, P.C., Liu, Z., Matsui, H., Moriya, K., Nishi, H., Opdyke, B.N., Penman, D., Romans, B., Scher, H.D., Sexton, P., Takagi, H., Turner, S.K., Whiteside, J.H., Yamaguchi, T., and Yamamoto, Y., 2014a. Methods. *In* Norris, R.D., Wilson, P.A., Blum, P., and the Expedition 342 Scientists, *Proc. IODP,* 342: College Station, TX (Integrated Ocean Drilling Program). **doi:10.2204/iodp.proc.342.102.2014**

Norris, R.D., Wilson, P.A., Blum, P., Fehr, A., Agnini, C., Bornemann, A., Boulila, S., Bown, P.R., Cournede, C., Friedrich, O., Ghosh, A.K., Hollis, C.J., Hull, P.M., Jo, K., Junium, C.K., Kaneko, M., Liebrand, D., Lippert, P.C., Liu, Z., Matsui, H., Moriya, K., Nishi, H., Opdyke, B.N., Penman, D., Romans, B., Scher, H.D., Sexton, P., Takagi, H., Turner, S.K., Whiteside, J.H., Yamaguchi, T., and Yamamoto, Y., 2014b. Site U1403. *In* Norris, R.D., Wilson, P.A., Blum, P., and the Expedition 342 Scientists, *Proc. IODP,* 342: College Station, TX (Integrated Ocean Drilling Program). **doi:10.2204/iodp.proc.342.104.2014**

Norris, R.D., Wilson, P.A., Blum, P., Fehr, A., Agnini, C., Bornemann, A., Boulila, S., Bown, P.R., Cournede, C., Friedrich, O., Ghosh, A.K., Hollis, C.J., Hull, P.M., Jo, K., Junium, C.K., Kaneko, M., Liebrand, D., Lippert, P.C., Liu, Z., Matsui, H., Moriya, K., Nishi, H., Opdyke, B.N., Penman, D., Romans, B., Scher, H.D., Sexton, P., Takagi, H., Turner, S.K., Whiteside, J.H., Yamaguchi, T., and Yamamoto, Y., 2014c. Site U1404. *In* Norris, R.D., Wilson, P.A., Blum, P., and the Expedition 342 Scientists, *Proc. IODP,* 342: College Station, TX (Integrated Ocean Drilling Program). **doi:10.2204/iodp.proc.342.105.2014**

Pälike, H., Lyle, M.W., Nishi, H., Raffi, I., Ridgwell, A., Gamage, K., Klaus, A., Acton, G., Anderson, L., Backman, J., Baldauf, J., Beltran, C., Bohaty, S.M., Bown, P., Busch, W., Channell, J.E.T., Chun, C.O.J., Delaney, M., Dewangan, P., Dunkley Jones, T., Edgar, K.M., Evans, H., Fitch, P., Foster, G,L., Gussone, N., Hasegawa, H., Hathorne, E.C., Hayashi, H., Herrle, J.O., Holbourn, A., Hovan, S., Hyeong, K., Iijima, K., Ito, T., Kamikuri, S., Kimoto, K., Kuroda, J., Leon-Rodriguez, L., Malinverno, A., Moore, T.C., Jr., Murphy, B.H., Murphy, D.P., Nakamura, H., Ogane, K., Ohneiser, C., Richter, C., Robinson, R., Rohling, E.J., Romero, O., Sawada, K., Scher, H., Schneider, L., Sluijs, A., Takata, H., Tian, J., Tsujimoto, A., Wade, B.S., Westerhold, T., Wilkens, R., Williams, T., Wilson, P.A., Yamamoto, Y., Yamamoto, S., Yamazaki, T., and Zeebe, R.E., 2012. A Cenozoic record of the equatorial Pacific carbonate compensation depth. *Nature (London, U. K.),* 488(7409):609–614. **doi:10.1038/nature11360**

Pribnow, D., Kinoshita, M., and Stein, C., 2000. *Thermal Data Collection and Heat Flow Recalculations for Ocean Drilling Program Legs 101–180:* Hanover, Germany (Inst. Joint Geosci. Res., Inst. Geowiss. Gemeinschaftsauf. [GGA]). **http://www-odp.tamu.edu/publications/heatflow/ODPReprt.pdf**

Sanfilippo, A., and Blome, C.D., 2001. Biostratigraphic implications of mid-latitude Paleocene–Eocene radiolarian faunas from Hole 1051A, ODP Leg 171B, Blake Nose, western North Atlantic. *In* Kroon, D., Norris, R.D., and Klaus, A. (Eds.), *Western North Atlantic Palaeogene and Cretaceous Palaeoceanography.* Geol. Soc. Spec. Publ., 183(1):l85–224. **doi:10.1144/GSL.SP.2001.183.01.10**

Tucholke, B.E., and Vogt, P.R., 1979. Western North Atlantic: sedimentary evolution and aspects of tectonic history. *In* Tucholke, B.E., Vogt, P.R., et al., *Init. Repts. DSDP,* 43: Washington, DC (U.S. Govt. Printing Office), 791–825. **doi:10.2973/dsdp.proc.43.140.1979**

Valet, J.-P., Meynadier, L., and Guyodo, Y., 2005. Geomagnetic dipole strength and reversal rate over the past two million years. *Nature (London, U. K.),* 435(7043):802–805. **doi:10.1038/nature03674**

Yamazaki, T., and Oda, H., 2001. A Brunhes–Matuyama polarity transition record from anoxic sediments in the South Atlantic (Ocean Drilling Program Hole 1082C). *Earth, Planets Space,* 53(8):817–827. **http://www.terrapub.co.jp/journals/EPS/pdf/2001/5308/53080817.pdf**

Publication: 3 March 2014
MS 342-109

Figure F1. Bathymetric map for northwestern Southeast Newfoundland Ridge, northeast of J-Anomaly Ridge, Expedition 342. Data are based upon multibeam mapping by the KNR179-1 site survey. Single-channel seismic reflection profiles shown in Figures F2 and F3.

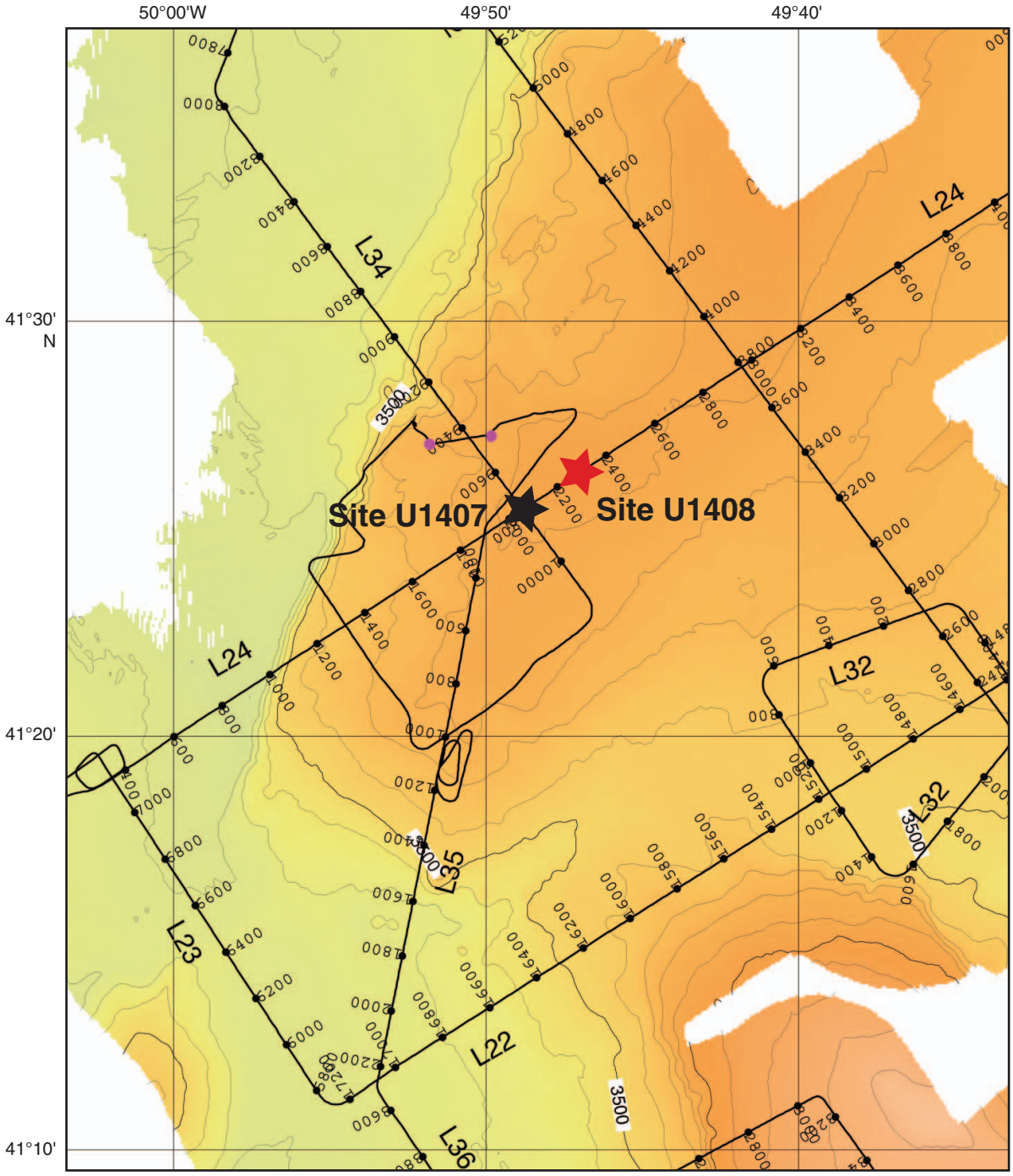

Figure F2. Single-channel seismic KNR179-1 Line 24. This is the southwest–northeast line crossing Site U1408 (at shotpoint [SP] 2285). White bars represent approximate depths of penetration of Sites U1407 and U1408.

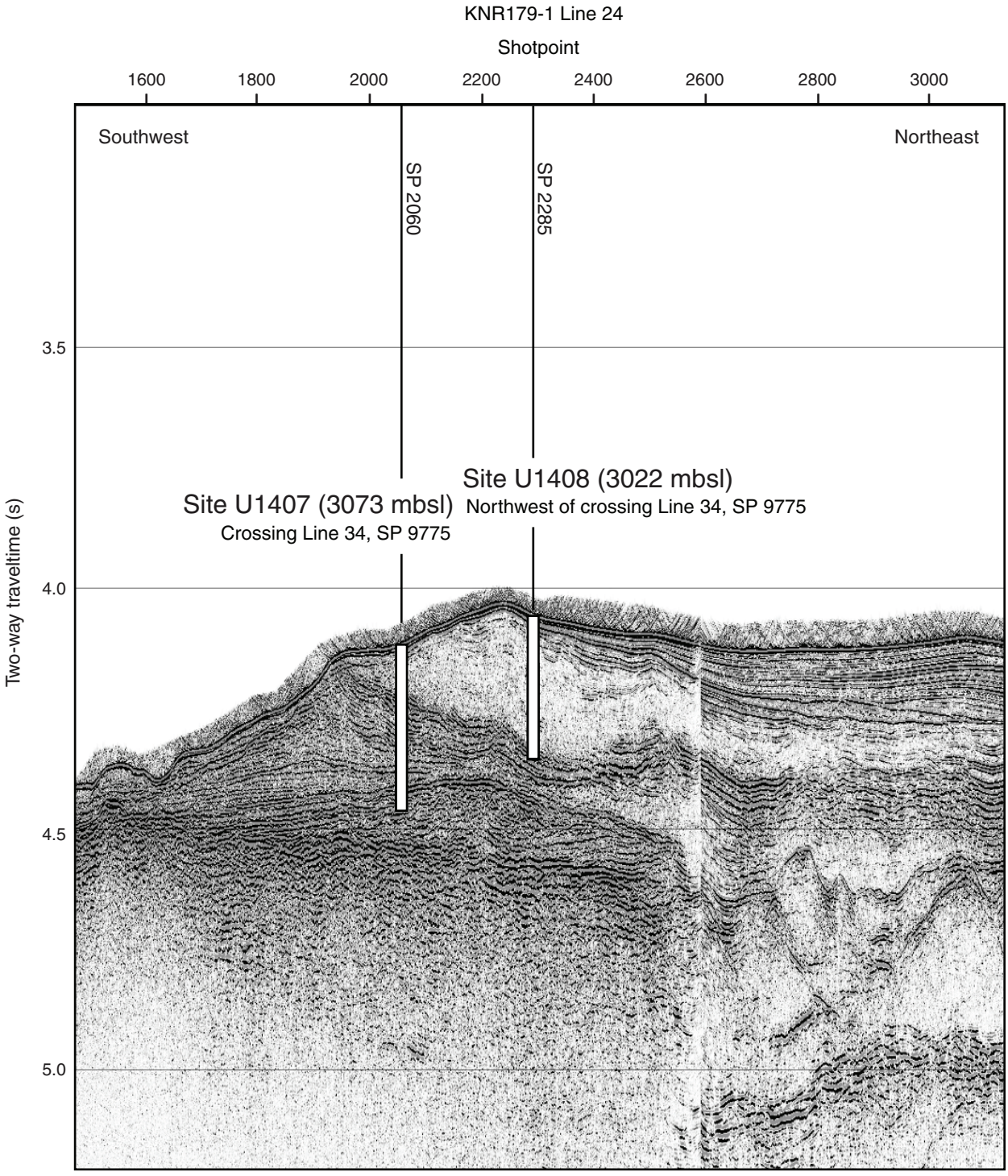

Figure F3. Single-channel seismic KNR179-1 Line 34. This is the northwest–southeast line crossing near Site U1408 (northwest of crossing at shotpoint 9775). Line 34 does not pass through Site U1408, but does show the lenslike character of the Eocene sediment drift sampled at Sites U1407 and U1408. White bar represents approximate depth of penetration of Site U1408.

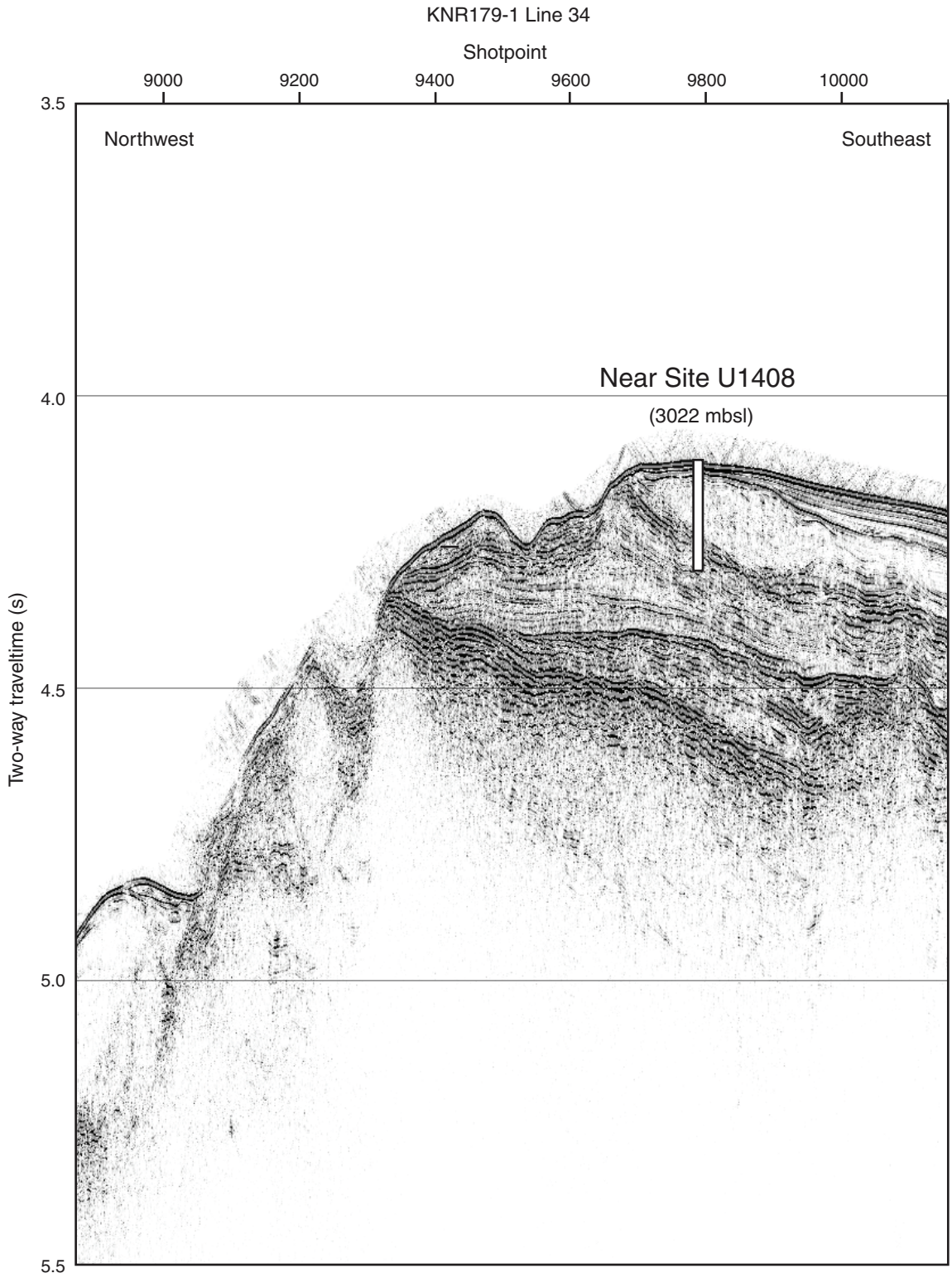

Figure F4. Lithostratigraphic summary, Site U1408.

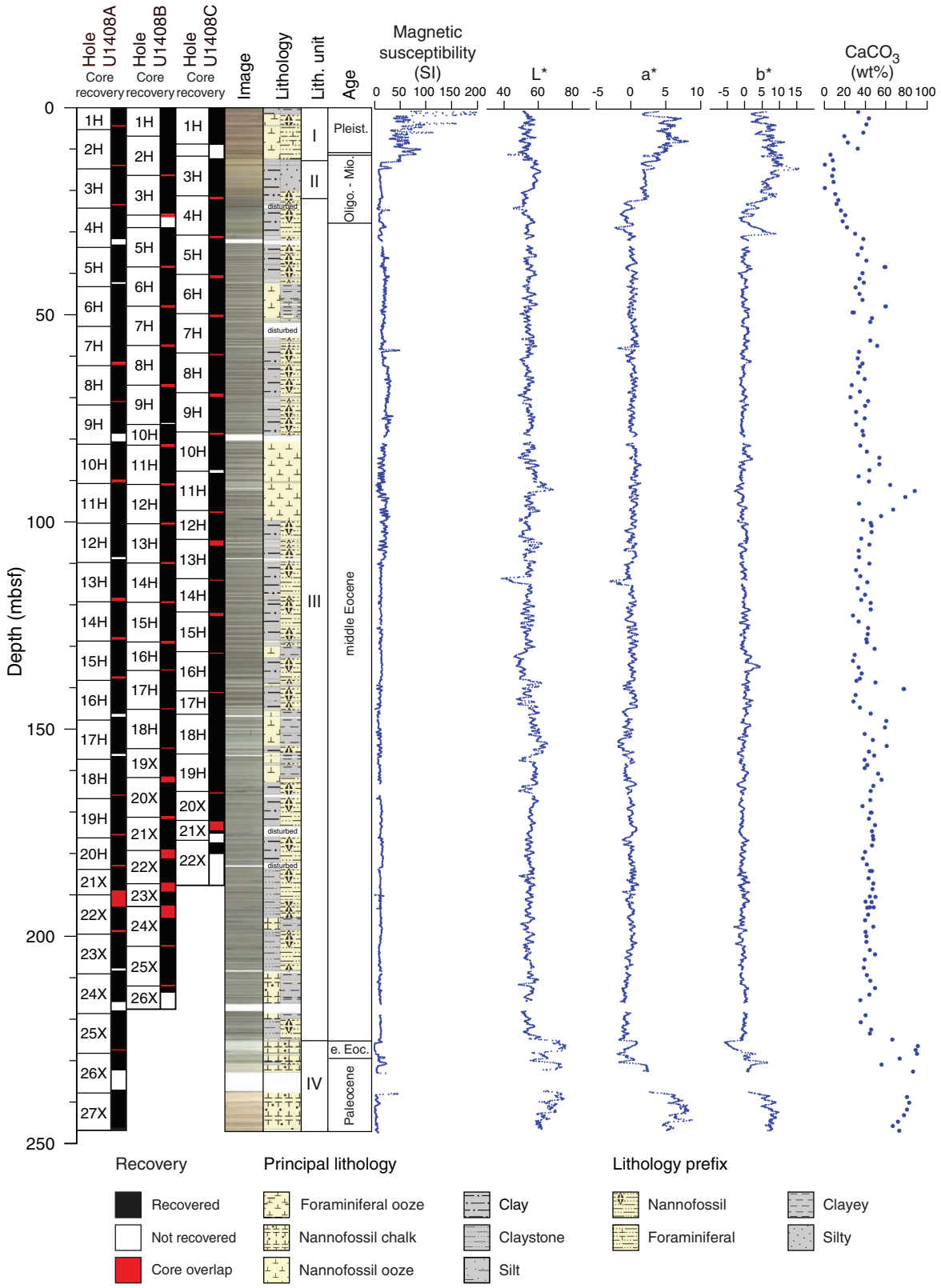

Figure F5. Core images of most common lithologies, Site U1408. **A.** Pleistocene foraminiferal sand in nannofossil ooze, Unit I. **B.** Pleistocene brownish clay, Unit I. **C.** Yellow-brown nannofossil ooze, Unit II. **D.** Middle Eocene greenish gray nannofossil clay, Unit III. **E.** Middle Eocene white-gray nannofossil ooze, Unit III. **F.** Paleocene nannofossil chalk with radiolarians, Unit IV.

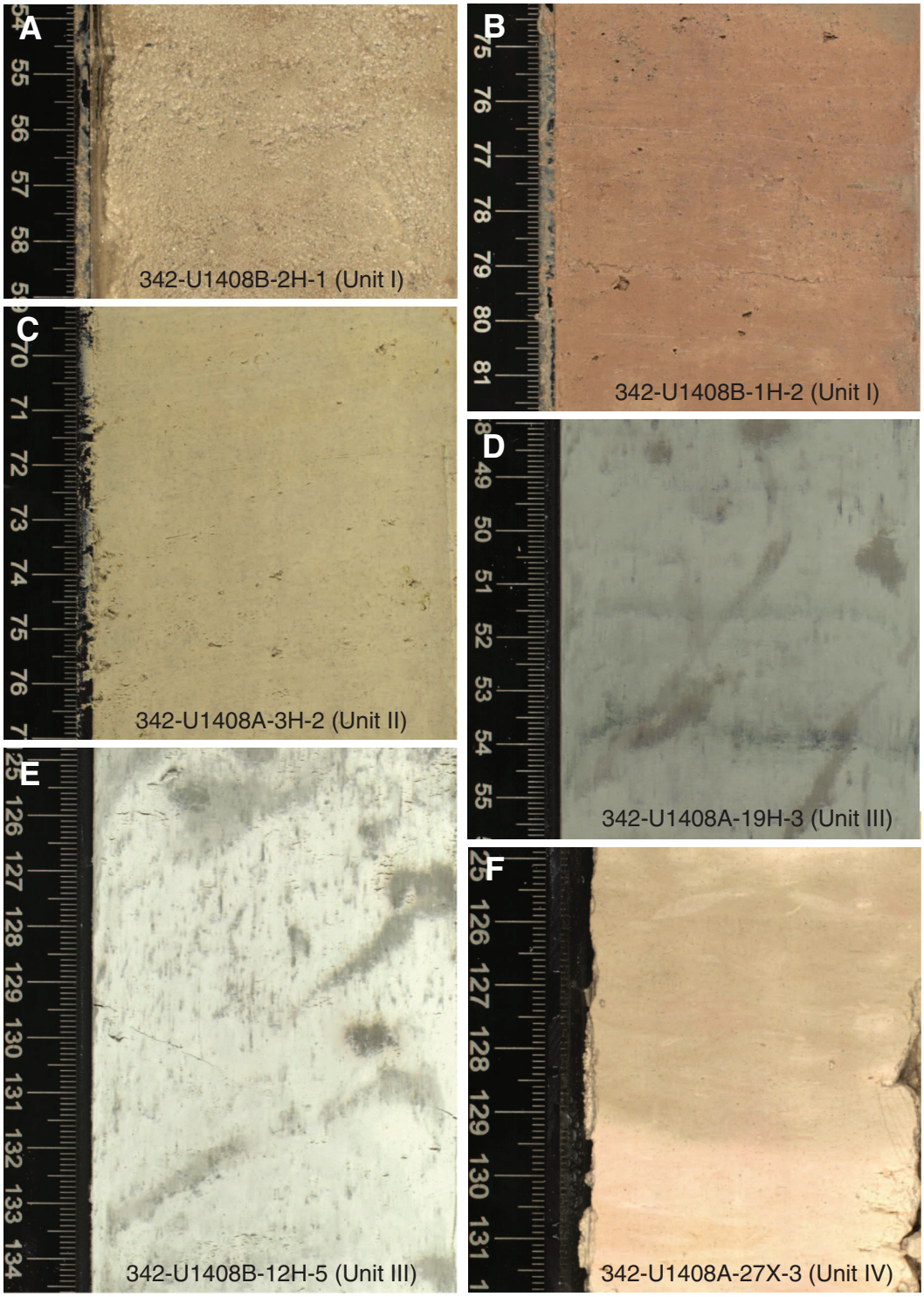

Figure F6. Photomicrographs of smear slides indicating the dominant lithologies of Units I–IV, Site U1408. **A.** Nannofossil foraminiferal ooze, Unit I. **B.** Silty clay, Unit II. **C.** Nannofossil ooze with foraminifers, Unit III. **D.** Nannofossil chalk, Unit IV.

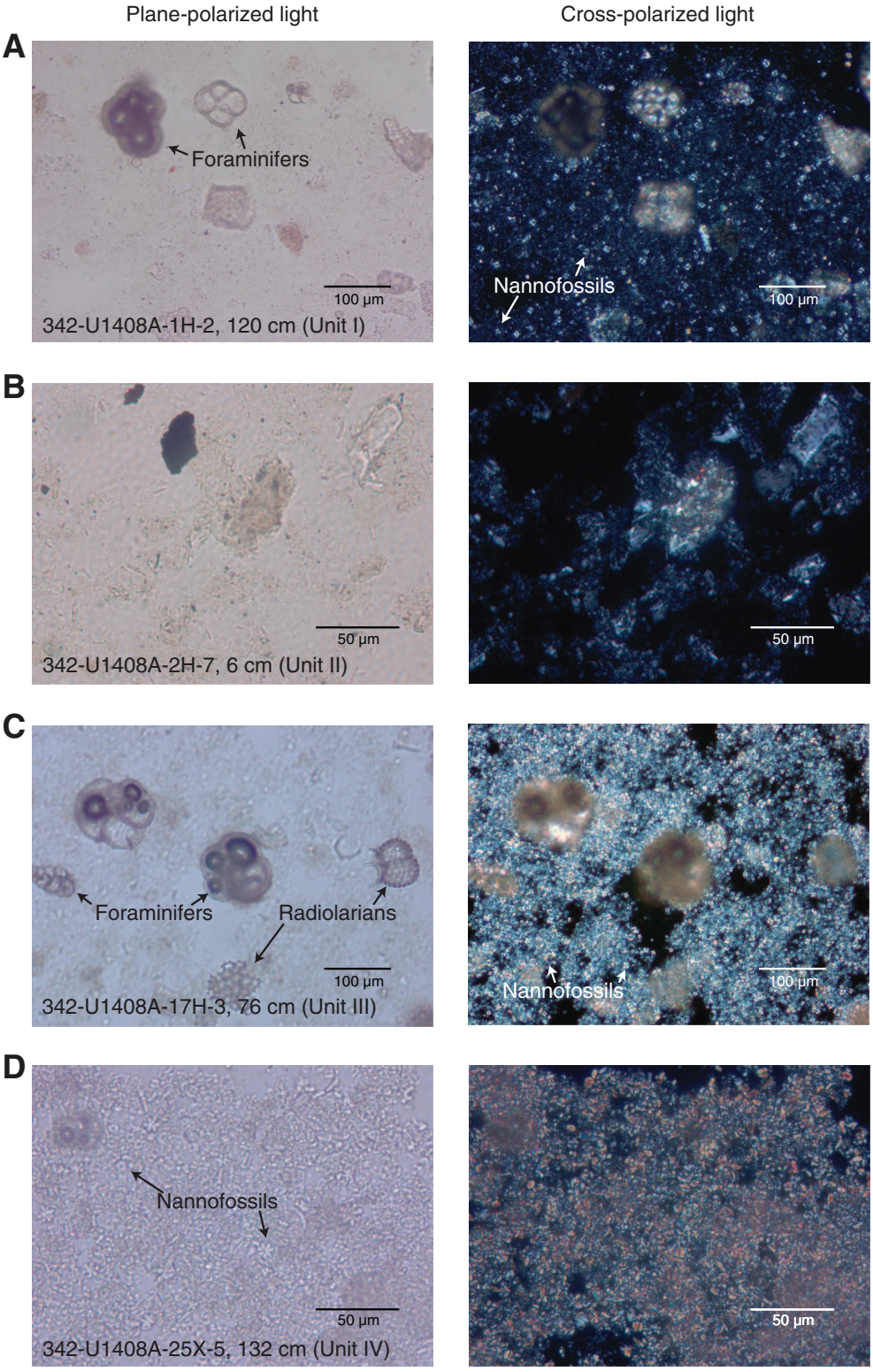

Figure F7. Plots of smear slide results of major biogenic and lithologic components and their relative abundance, Hole U1408A. VA = very abundant, A = abundant, C = common, F = few, P = present.

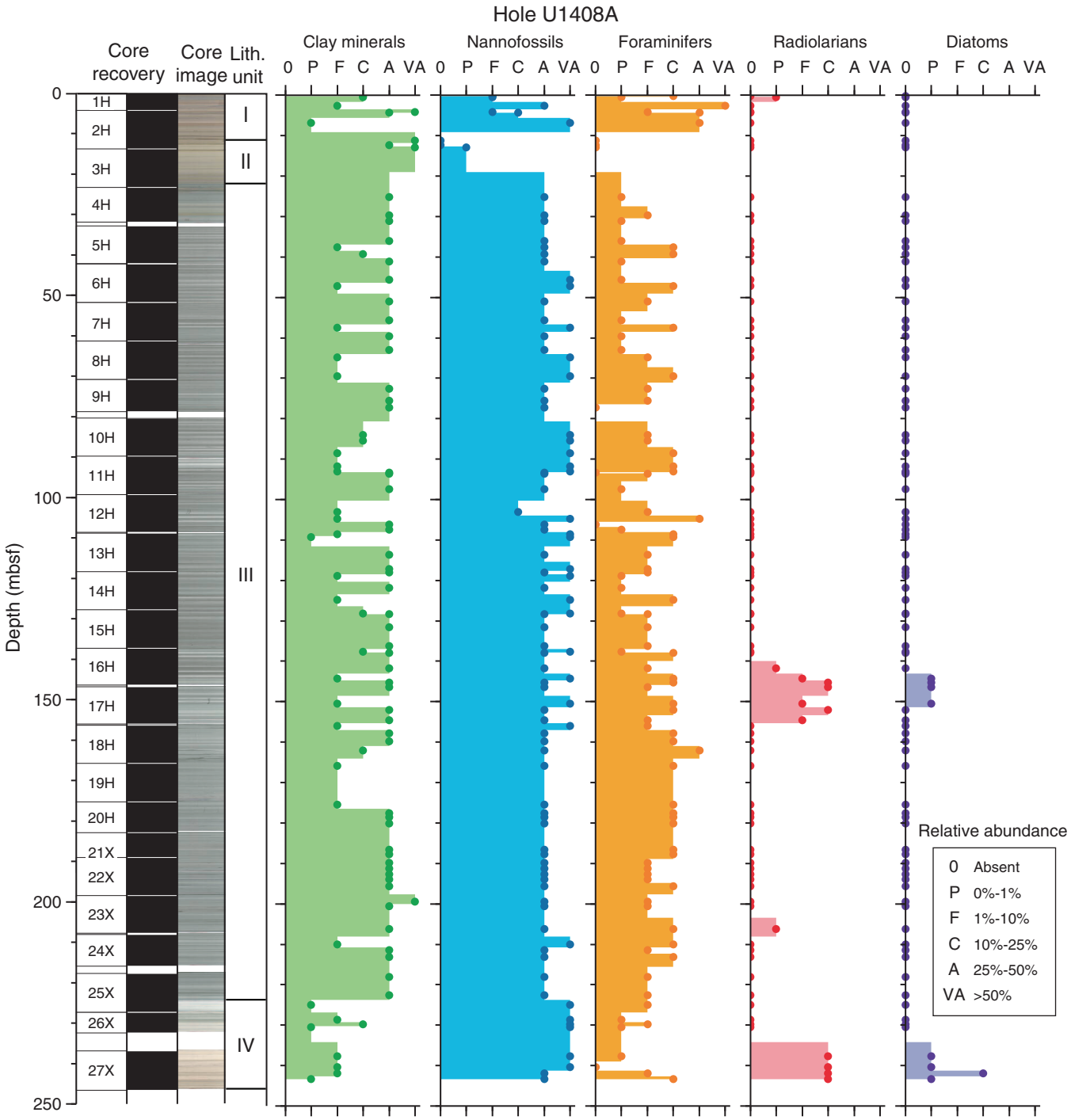

Figure F8. Plots of smear slide results of major biogenic and lithologic components and their relative abundance, Hole U1408B. VA = very abundant, A = abundant, C = common, F = few, P = present.

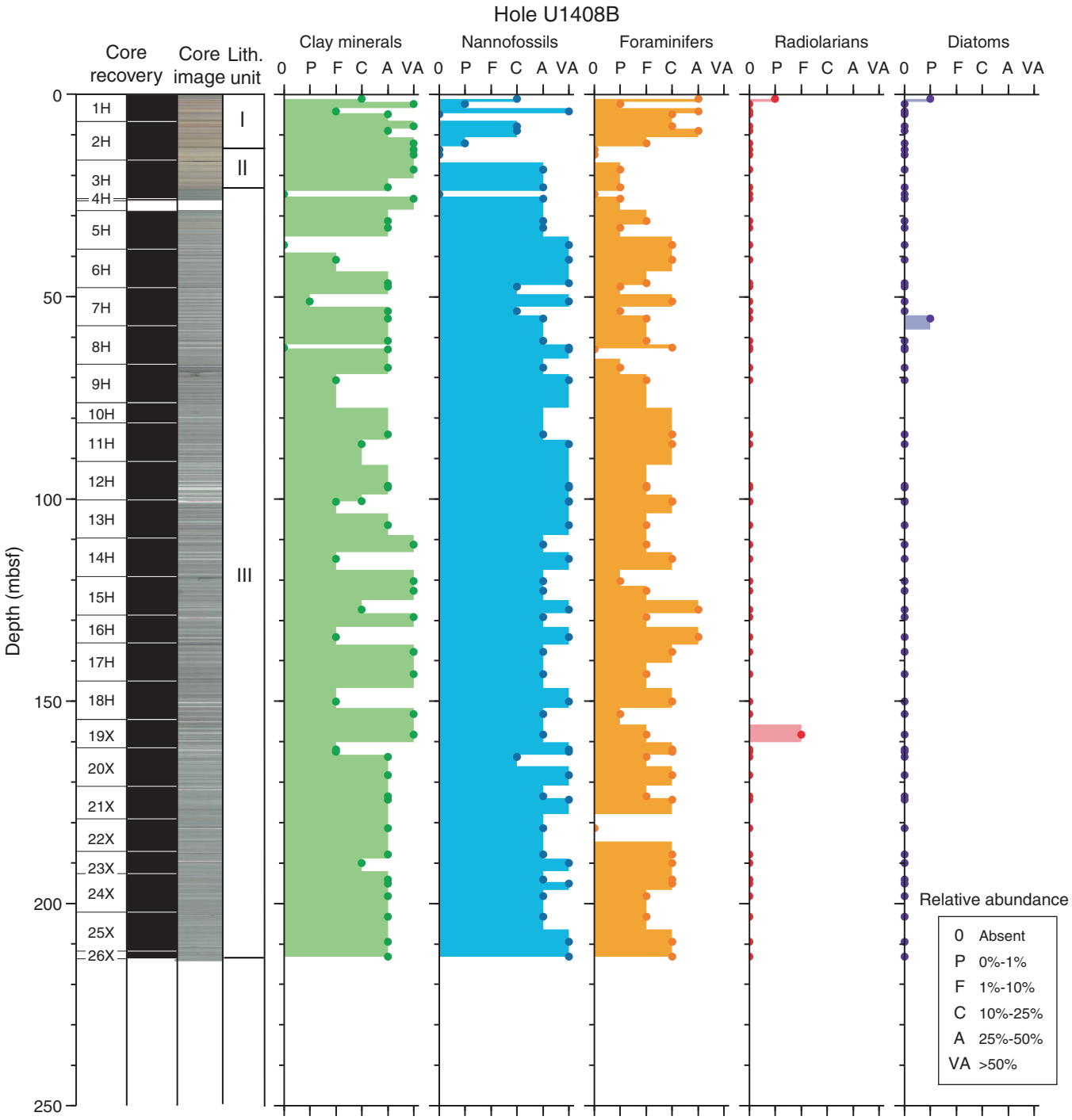

Figure F9. Plots of smear slide results of major biogenic and lithologic components and their relative abundance, Hole U1408C. VA = very abundant, A = abundant, C = common, F = few, P = present.

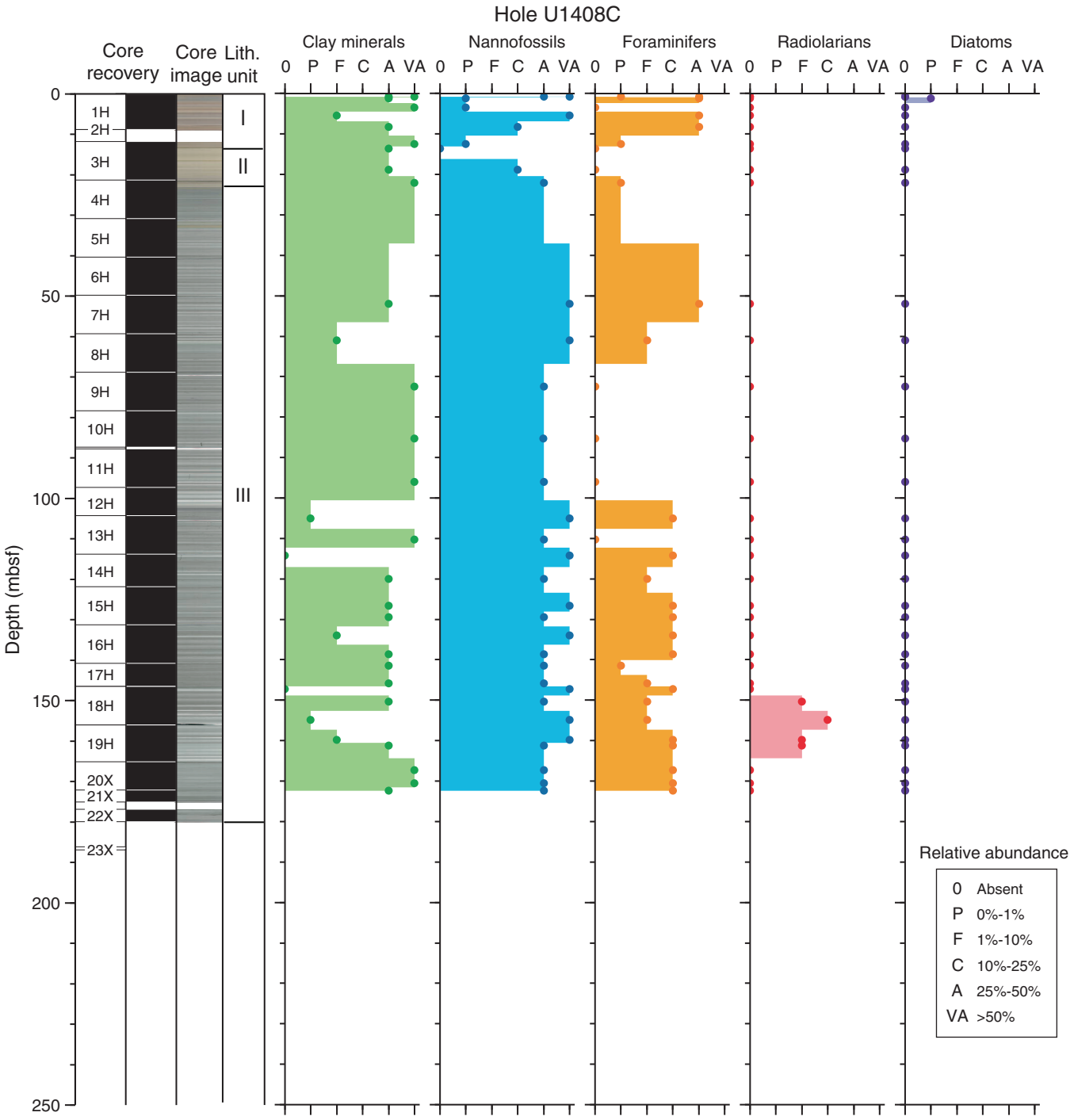

Figure F10. Lithologic expression and physical property data of cyclicity across the Middle Eocene Climatic Optimum, Hole U1408B. The Chron C18r/C18n.2n boundary is correlated from Hole U1408A because the boundary was not identified in Hole U1408B. NGR = natural gamma radiation.

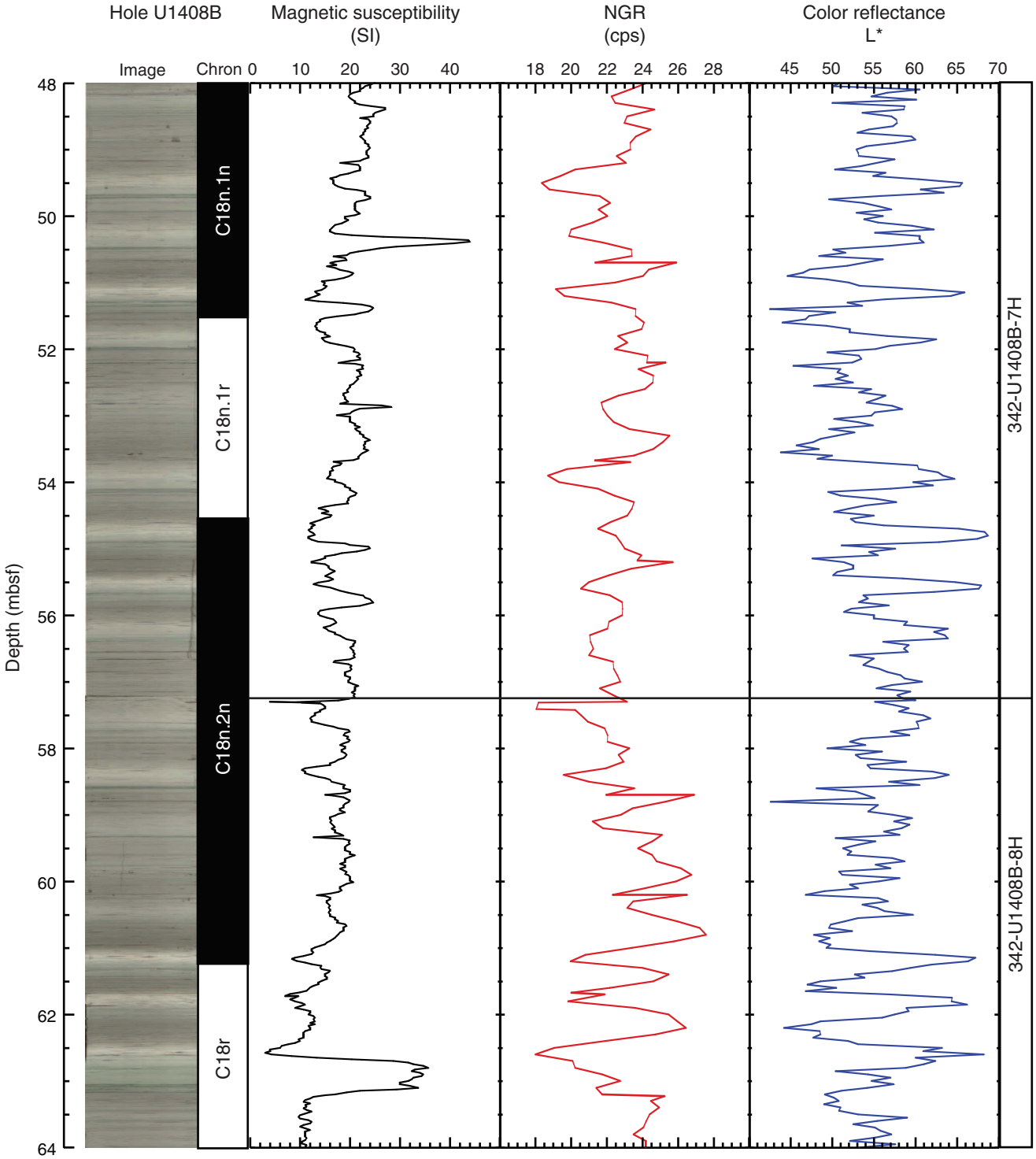

Figure F11. X-ray diffractograms (XRD) of mineralogical changes throughout a typical light gray to grayish green to dark green sequence within Unit III, Hole U1408A. XRD results suggest a rather uniform mineralogical composition. Only the calcite peak suggests differences between the studied lithologies, with more calcite in the whitish interval compared to the greenish and greenish gray levels.

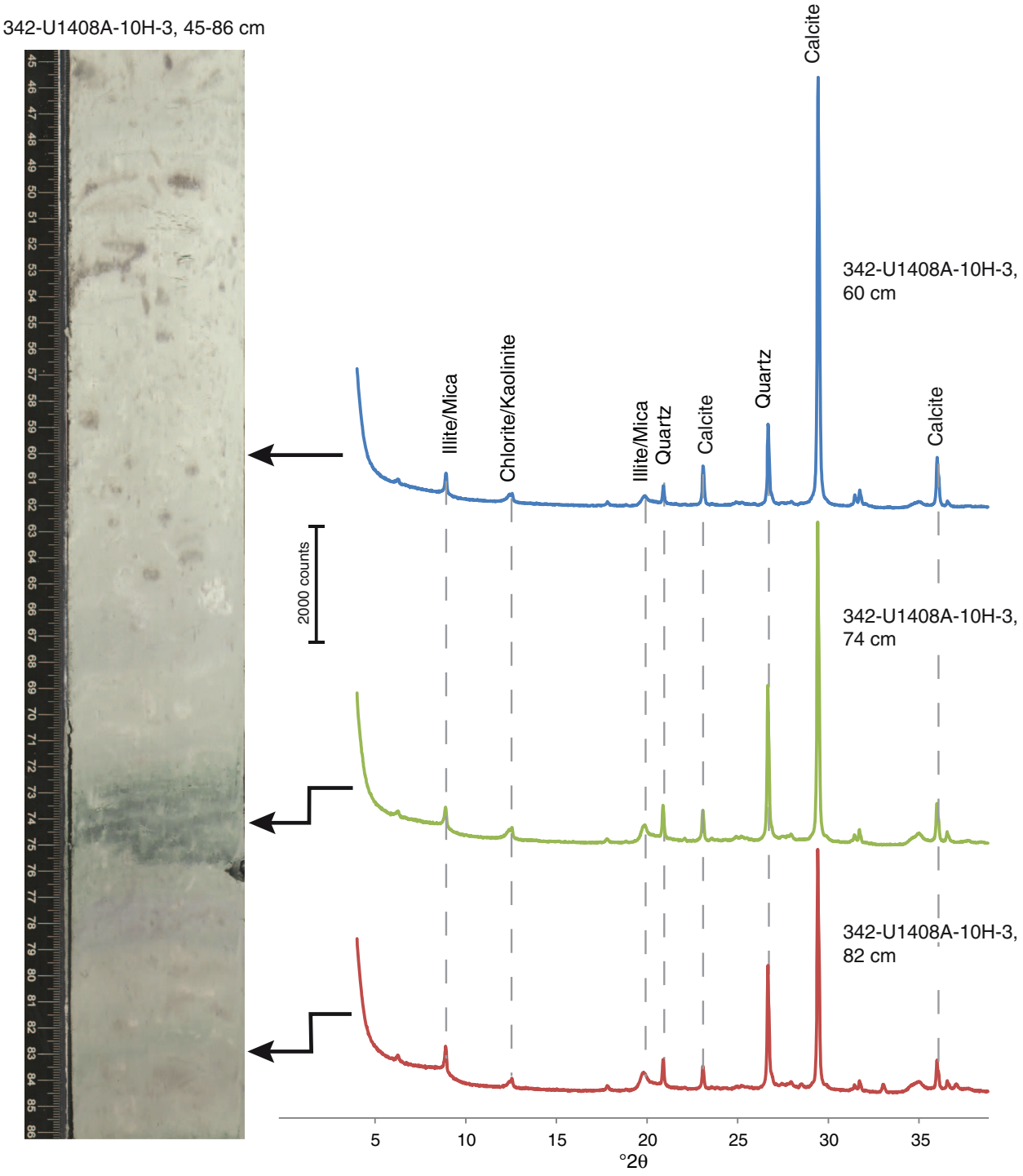

Figure F12. Core images of examples of green glauconitic and black sulfitic horizons, Site U1408. Note the crosscutting relationship between the green and black horizons and the *Zoophycos* burrows. The crosscutting relationship indicates that the diagenetic horizons were not formed at the sediment/water interface. Rather, they must have been formed at some time and depth below the zone of active bioturbation.

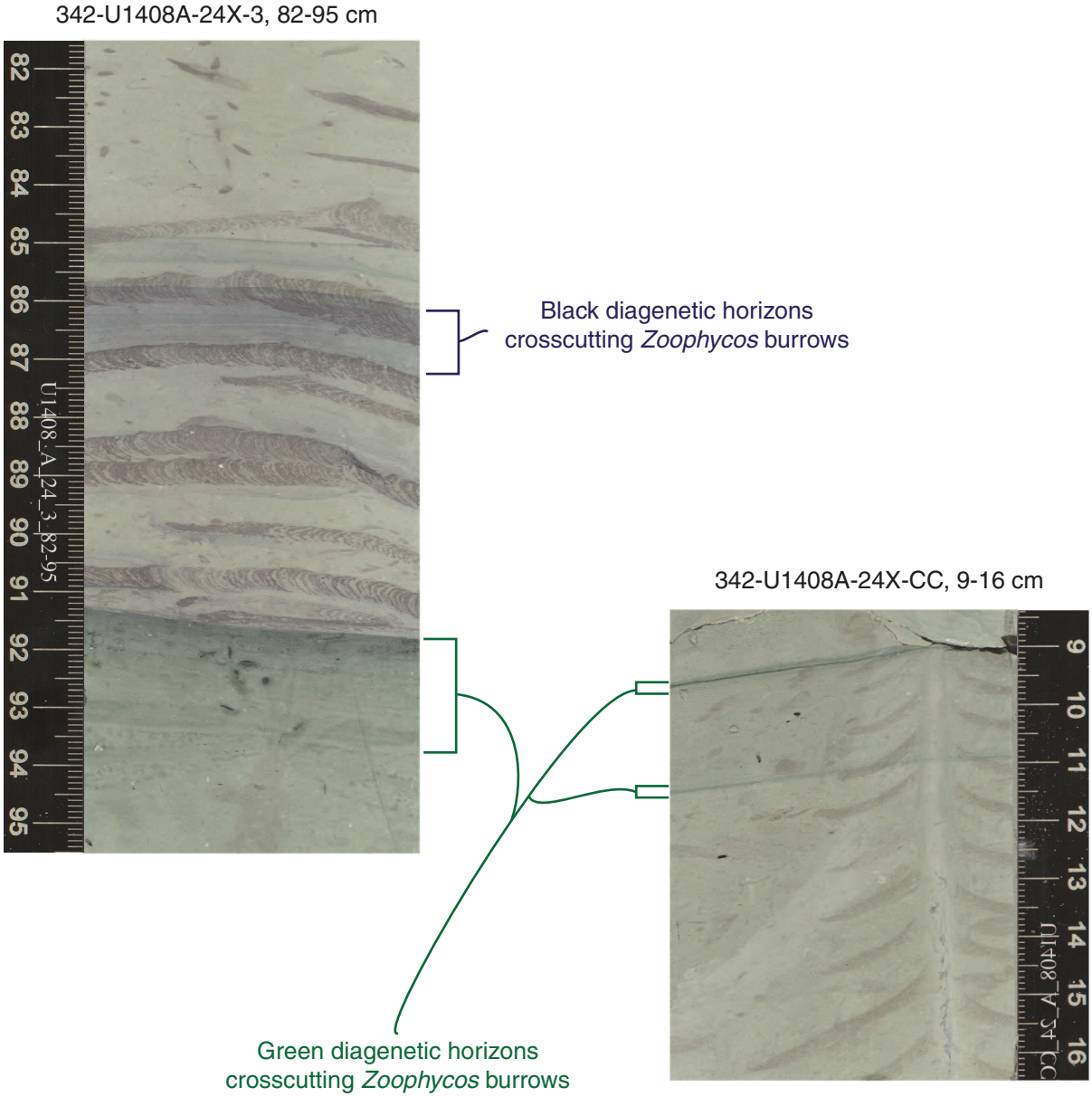

Figure F13. Photomicrographs of sand-sized lithic grains from upper nannofossil Zone NP23 (Oligocene; Sample 342-U1408A-4H-2, 100–101 cm). **A.** Overview of lithic grain types on a picking tray, showing abundant (angular) quartz grains and other mineral phases. **B.** Pinkish quartz grain. **C.** Two yellow quartz grains. **D.** Rock fragment and several quartz grains. **E.** Orange-brown rock fragment.

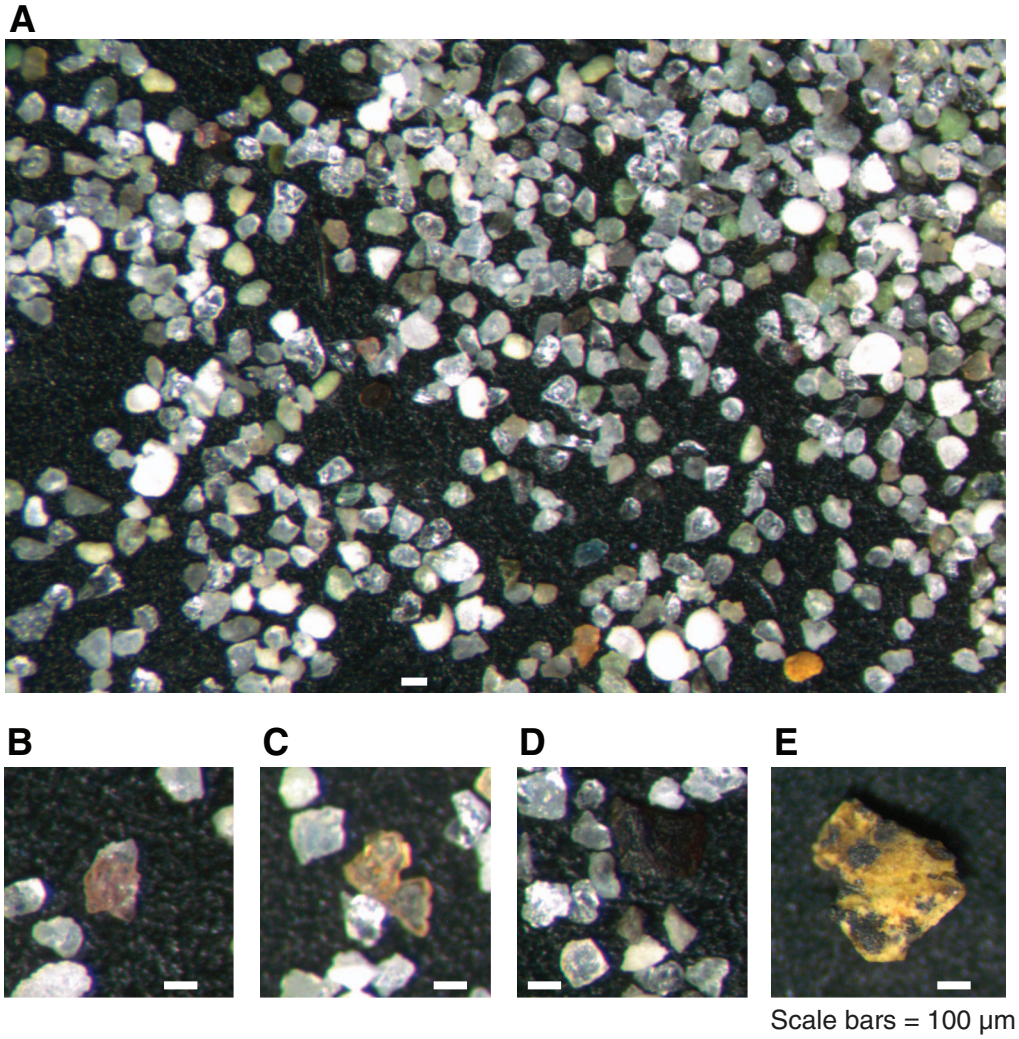

Figure F14. Integrated calcareous and siliceous microfossil biozonation, Site U1408.

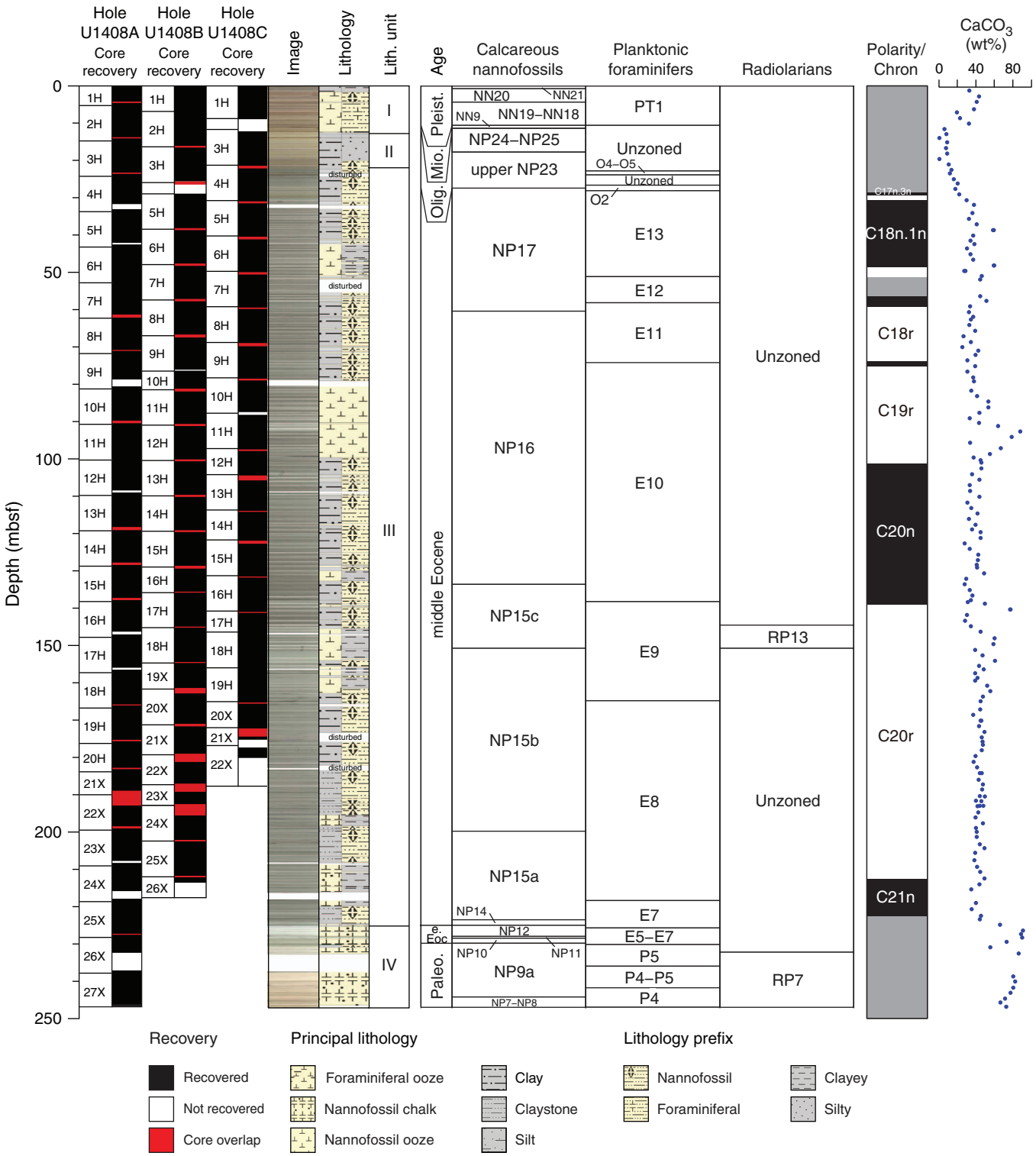

Figure F15. Age-depth model for Site U1408 showing biostratigraphic and magnetostratigraphic datums. Also shown are estimated linear sedimentation rates for line segments based on the datums listed in Table T16.

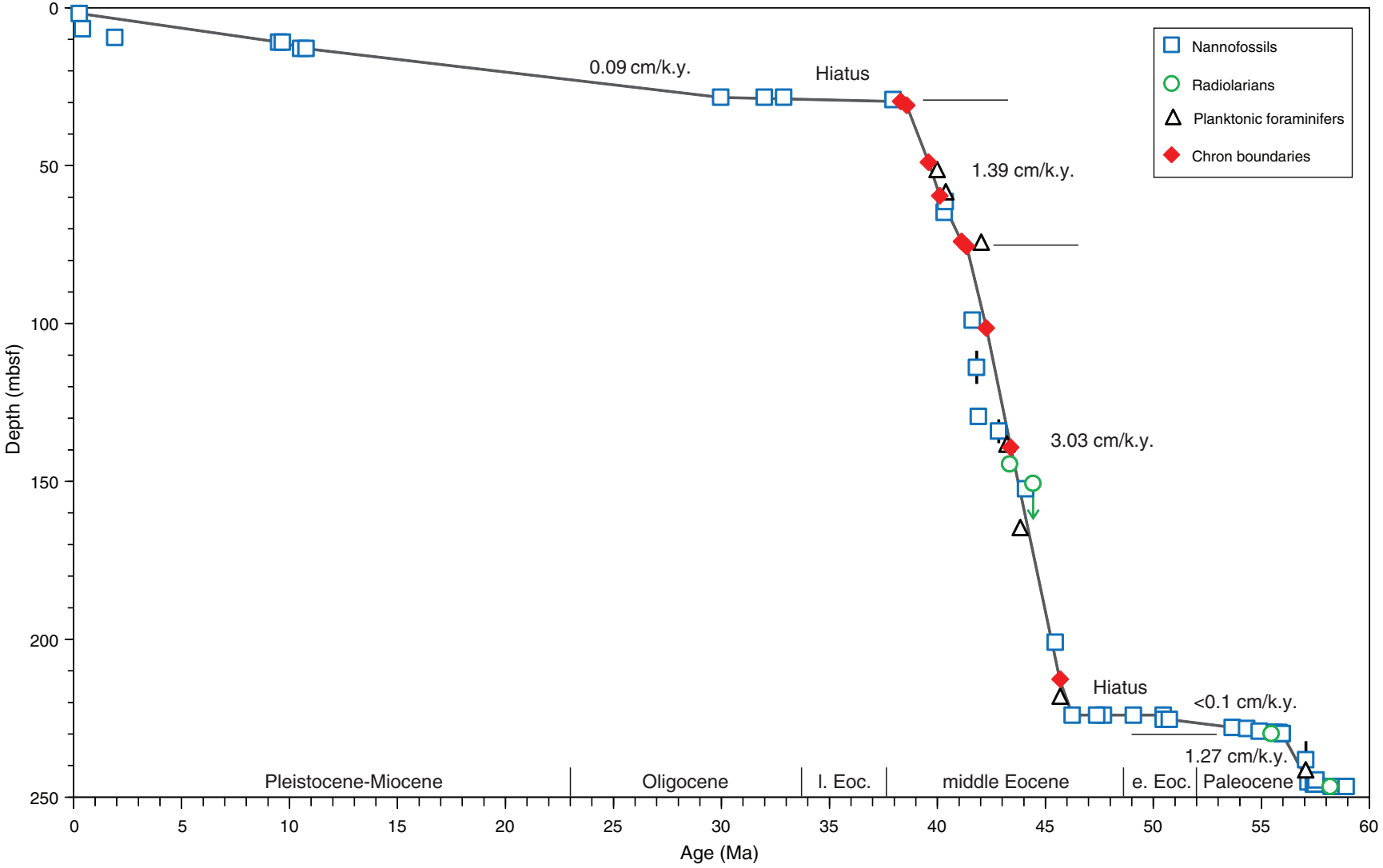

Figure F16. Group abundance and preservation of calcareous and siliceous microfossils, Site U1408. Solid and open symbols represent Holes U1408A and U1408B, respectively. Abundance: B = barren, P = present, R = rare, F = few, C = common, A = abundant, D = dominant. Preservation: P = poor, M = moderate, G = good, VG = very good.

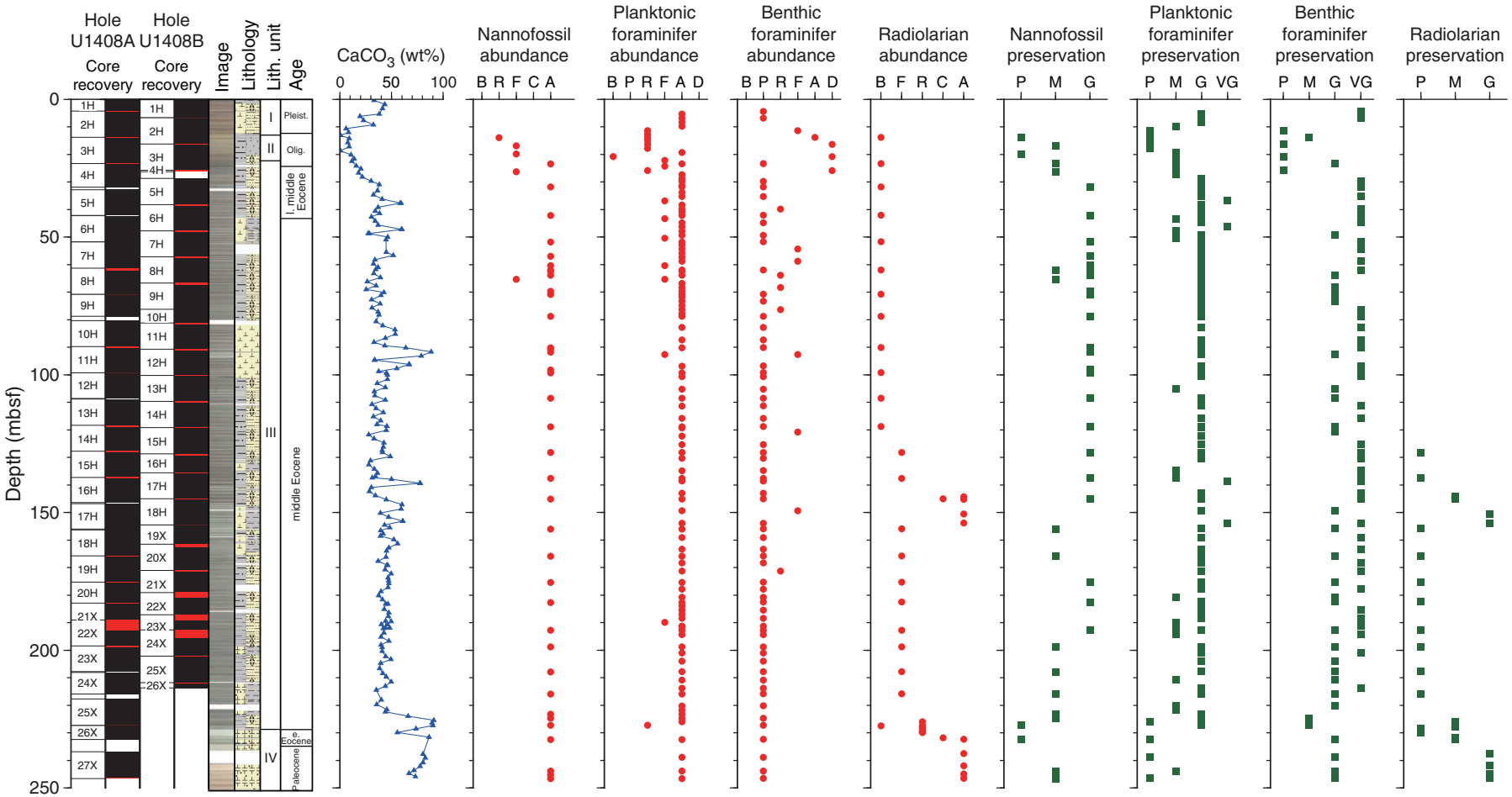

Figure F17. Photomicrographs of exceptionally well preserved planktonic foraminifers from the upper middle Eocene, Site U1408. **A.** *Hantkenina compressa, Hantkenina dumblei,* and *Hantkenina liebusi* reveal a glassy, transparent taphonomy, particularly in their final few chambers, and intact tubulospines, a rarity in typical pelagic deep-sea sequences (Sample 342-U1408A-6H-CC). **B.** *Globigerinatheka index* displaying semiglassy taphonomy and the presence of relict spines within the apertural opening. **C, D.** *Orbulinoides superbeckmanni,* characterized by a completely spherical test, which likely marks the acme of the Middle Eocene Climatic Optimum (MECO). **E–G.** *Orbulinoides beckmanni* (ancestor of C, D), which has a comparatively short (~1.6–1.0 m.y.) total range concurrent with the MECO (Edgar et al., 2010).

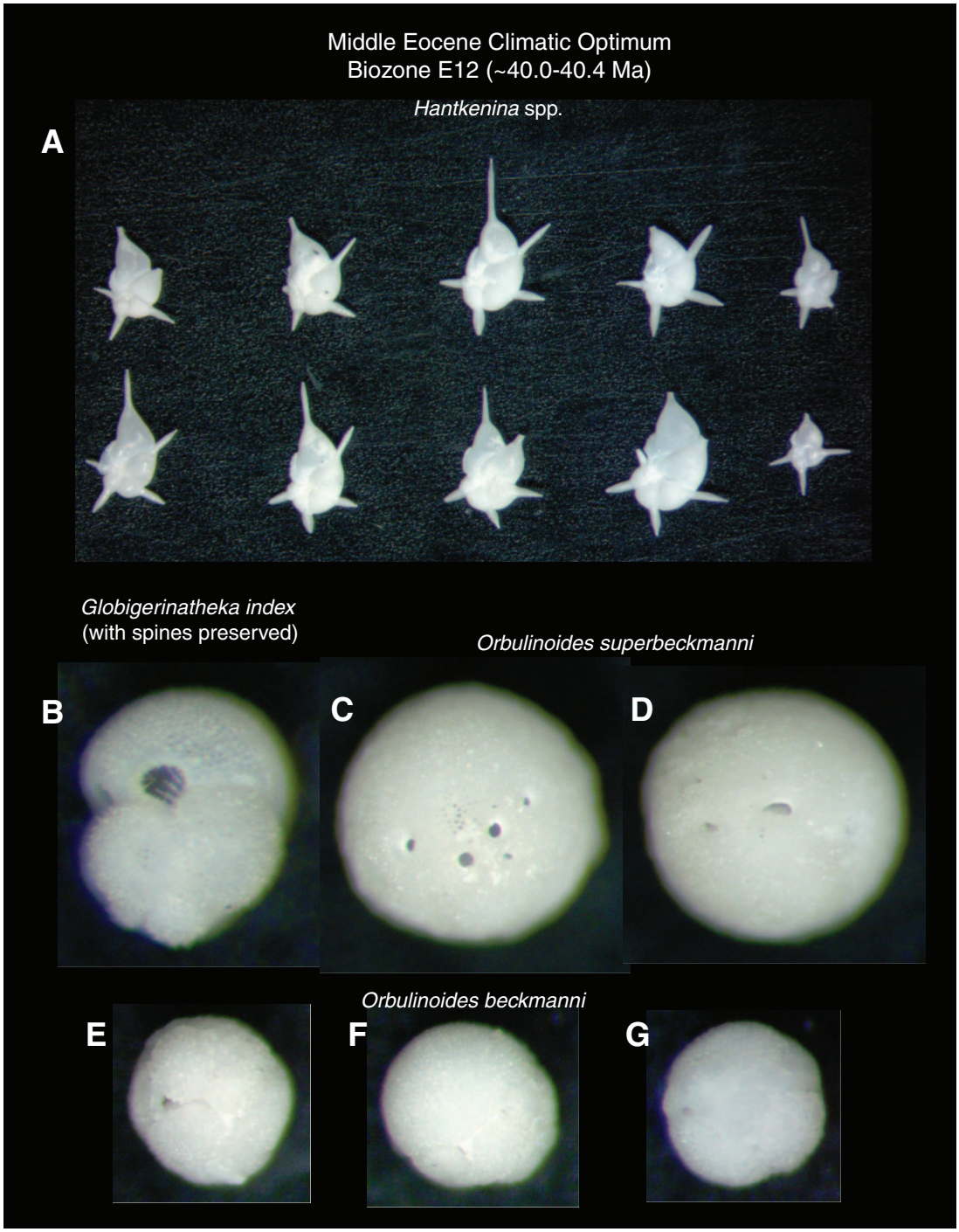

Figure F18. Photomicrographs of selected benthic foraminiferal taxa, Site U1408. Scale bar = 100 µm. **A, B.** *Anomalinoides semicribratus* (Sample 342-U1408A-6H-CC). **C, D.** *Nuttallides truempyi* (Sample 342-U1408A-10H-CC). **E.** *Praeglobobulimina* cf. *spinescens* (Sample 342-U1408A-10H-CC). **F, G.** *Oridorsalis umbonatus* (Sample 342-U1408A-9H-CC). **H.** *Pullenia quinqueloba*? (Sample 342-U1408A-9H-CC). **I.** *Cibicidoides subspiratus* (Sample 342-U1408A-6H-CC). **J.** *Dentalina* sp. (Sample 342-U1408A-6H-CC). **K.** *Pleurostomella tenius* (Sample 342-U1408A-11H-CC). **L–N.** *Cibicidoides praemundulus* (Sample 342-U1408A-10H-CC). **O.** *Cibicidoides grimsdalei* (Sample 342-U1408A-9H-CC). **P.** *Stilostomella subspinosa*.

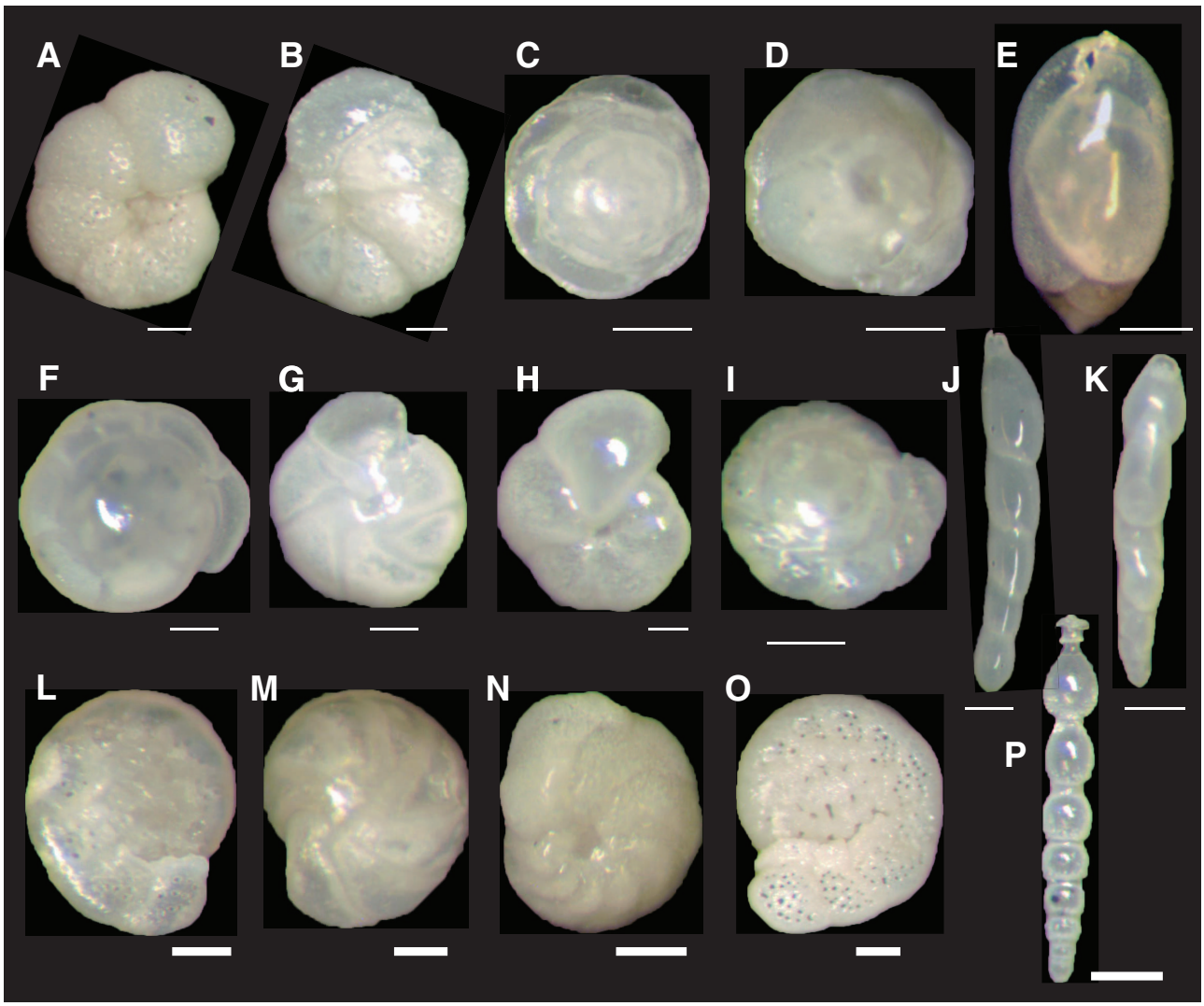

Figure F19. Plots of downhole variation of magnetic susceptibility and paleomagnetism data, Hole U1408A. Magnetization intensity, inclination, and declination are after 20 mT demagnetization. Only oriented advanced piston corer (APC) intervals show directions in geographic coordinates. Directions from all other intervals are shown in sample coordinates. For discrete sample data, if the samples were analyzed by principal component analysis (PCA; Kirschvink, 1980), then directions are shown according to PCA declination and inclination. Otherwise, directions following 20 mT demagnetization are shown. XCB = extended core barrel. Polarity: black = normal chron, white = reversed chron, gray = unidentified interval.

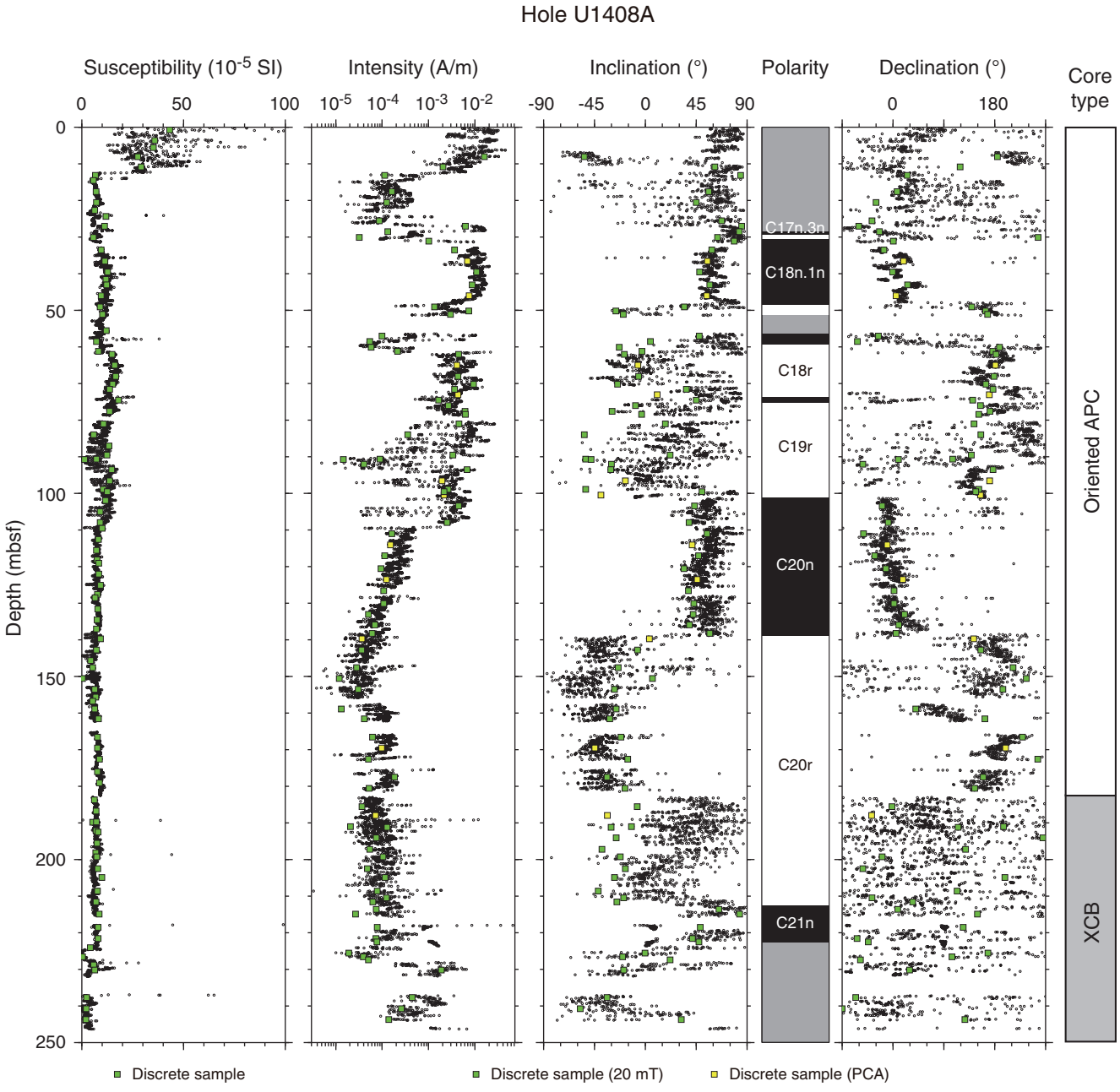

Figure F20. Plots of downhole variation of magnetic susceptibility and paleomagnetism data, Hole U1408B. Magnetization intensity, inclination, and declination are after 20 mT demagnetization. Only oriented advanced piston corer (APC) intervals show directions in geographic coordinates. Directions all other intervals are shown in sample coordinates. For discrete sample data, if the samples were analyzed by principal component analysis (PCA; Kirschvink, 1980), then directions are shown according to PCA declination and inclination. Otherwise, directions following 20 mT demagnetization are shown. XCB = extended core barrel. Polarity: black = normal chron, white = reversed chron, gray = unidentified interval.

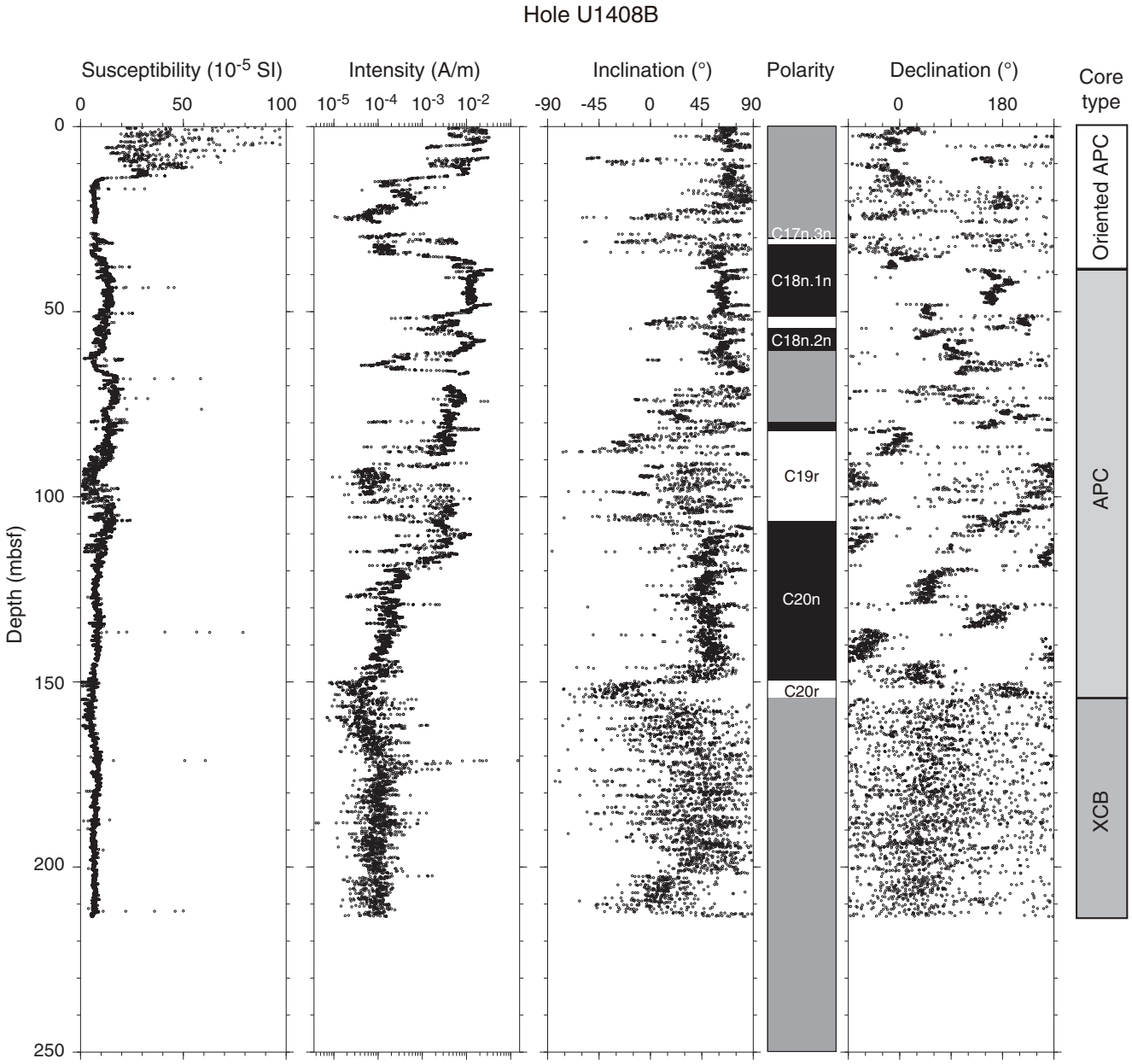

Figure F21. Plots of downhole variation of magnetic susceptibility and paleomagnetism data, Hole U1408C. Magnetization intensity, inclination, and declination are 20 mT demagnetization. Only oriented advanced piston corer (APC) intervals show directions in geographic coordinates. Directions from all other intervals are shown in sample coordinates. For discrete sample data, if the samples were analyzed by principal component analysis (PCA; Kirschvink, 1980), then directions are shown according to PCA declination and inclination. Otherwise, directions following 20 mT demagnetization are shown. XCB = extended core barrel. Polarity: black = normal chron, white = reversed chron, gray = unidentified interval.

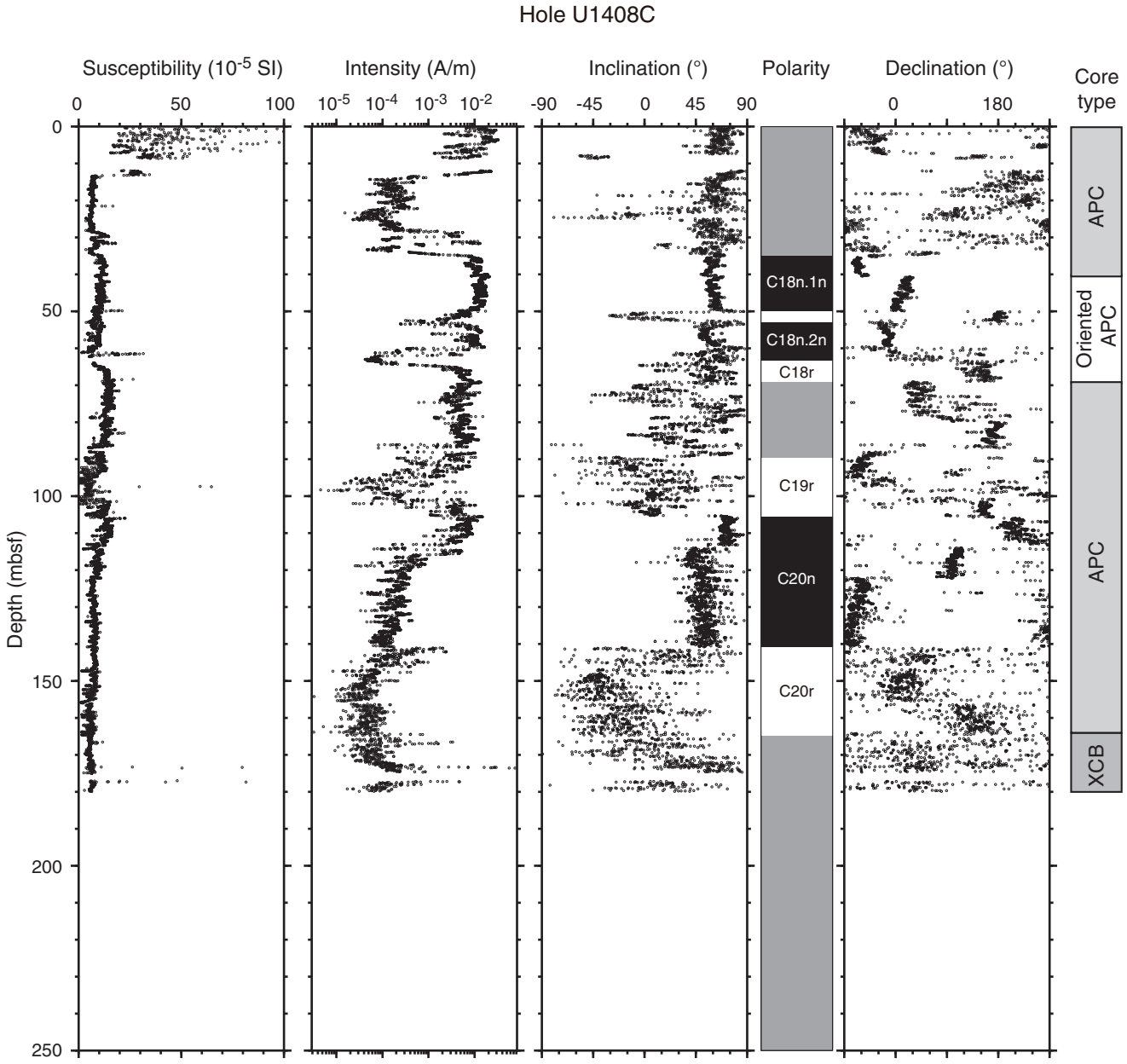

Figure F22. Plots of representative alternating field (AF) demagnetization results for discrete paleomagnetism samples, Site U1408. Upper plots show intensity variation with progressive demagnetization, and lower plots show vector endpoints of paleomagnetism directions on orthogonal vector diagrams (i.e., Zijderveld plots). Vector diagrams indicate reasonably resolved characteristic remanent magnetization (ChRM) directions for the (**A**) normal and (**B**) reversed chrons from the advanced piston core intervals, whereas (**C**) some samples do not show a stable component. Solid circles = horizontal projections, open circles = vertical projections, gray circles = data not used to calculate ChRM direction, black dashed line = ChRM direction. Inc = inclination, Dec = declination, MAD = maximum angle of deviation.

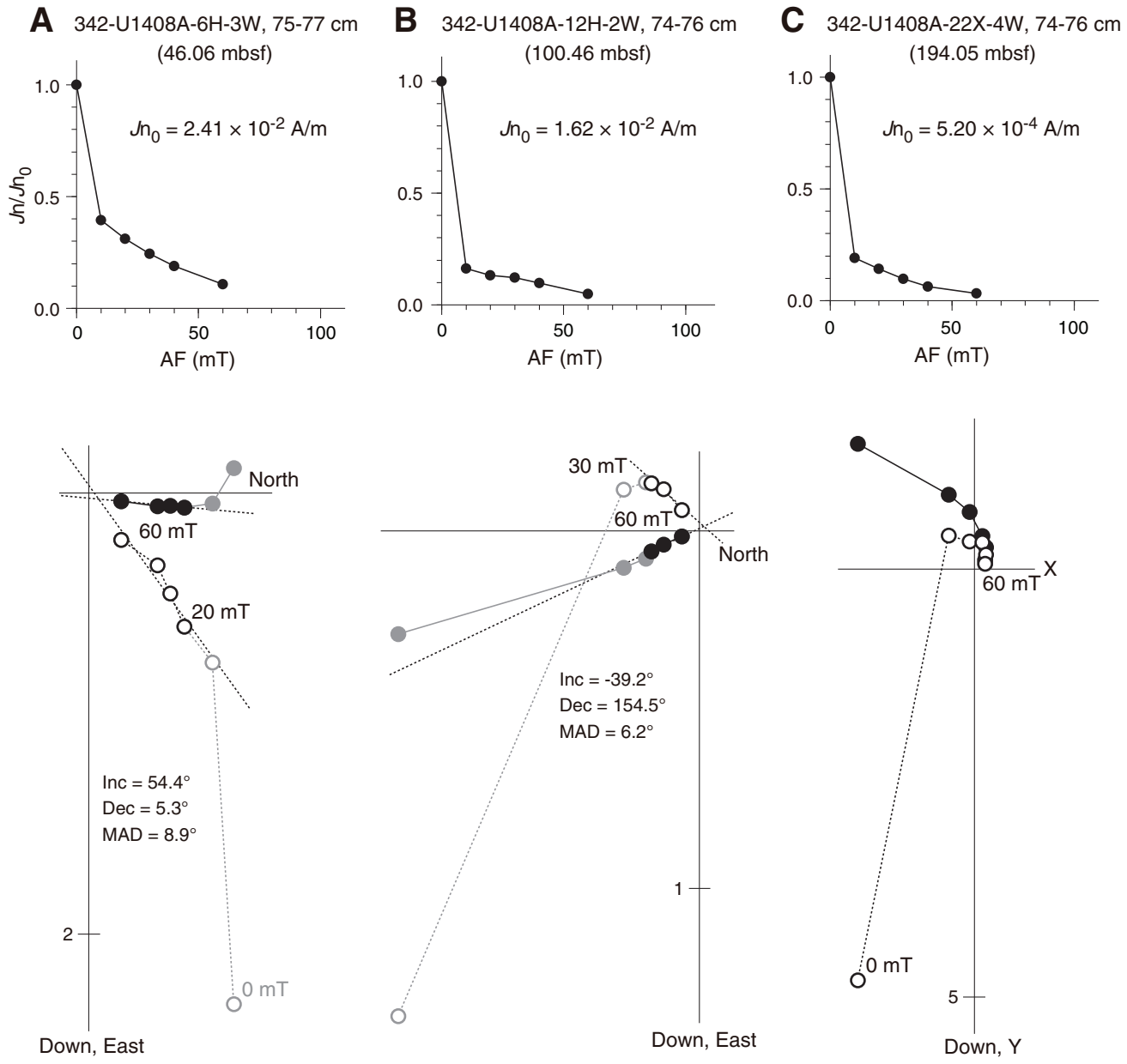

Figure F23. Illustration of magnetostratigraphy, Site U1408. Core recovery: black = recovered, white = not recovered, red = core overlap.

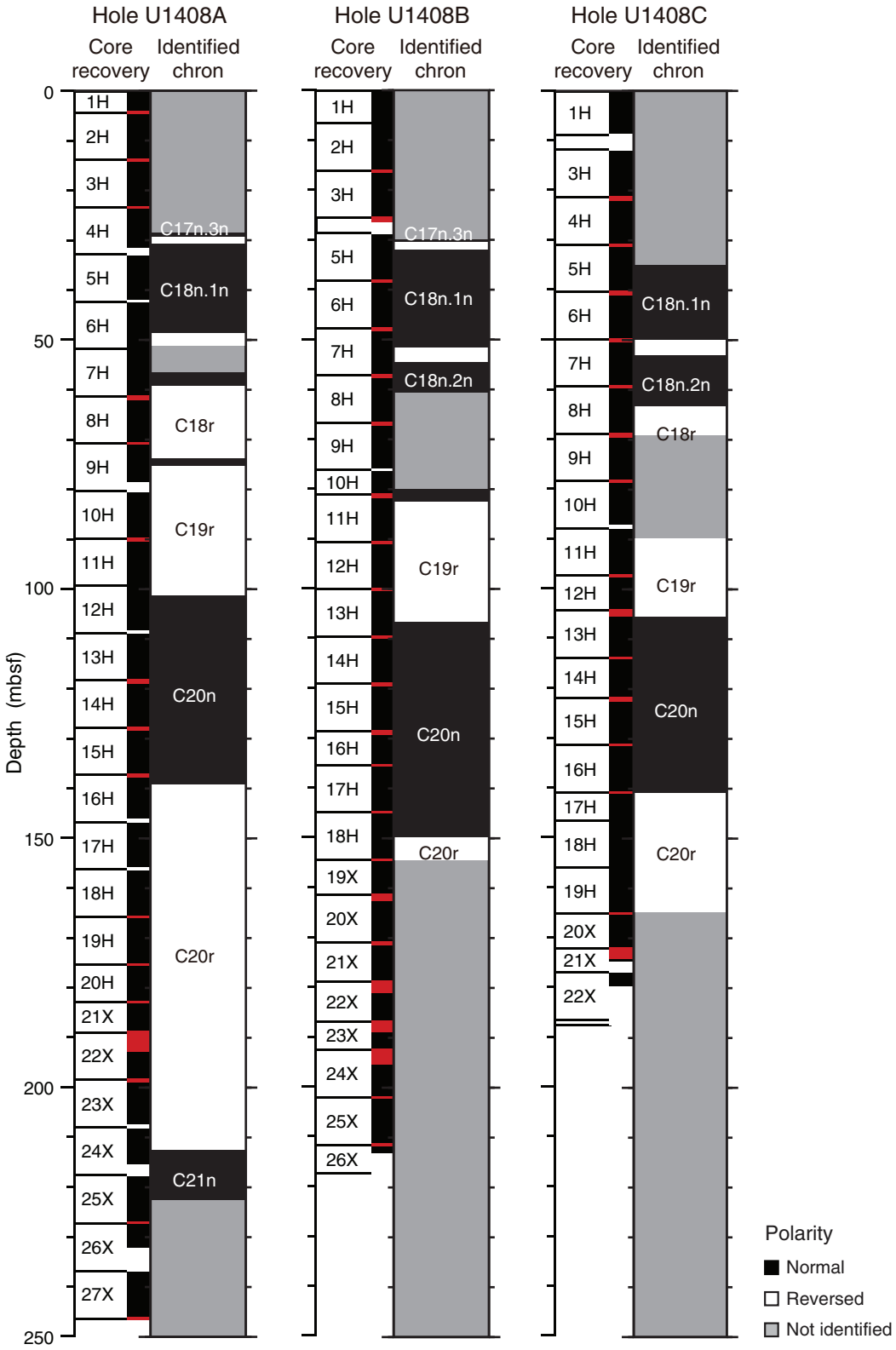

Figure F24. Plots of downhole variation of declination, inclination, and magnetization intensity after 20 mT demagnetization during the Chron C18n.1n–C18n.1r–C18n.2n geomagnetic field transitions. Plots are primarily shown for the Hole U1408B data (green), and data from Holes U1408A and U1408C are shown for the offset depth scale based on the adjusted horizons indicated by arrows (red = Hole U1408A, blue = Hole U1408C) in intensity. Polarity: black = normal chron, white = reversed chron, gray = transitional period.

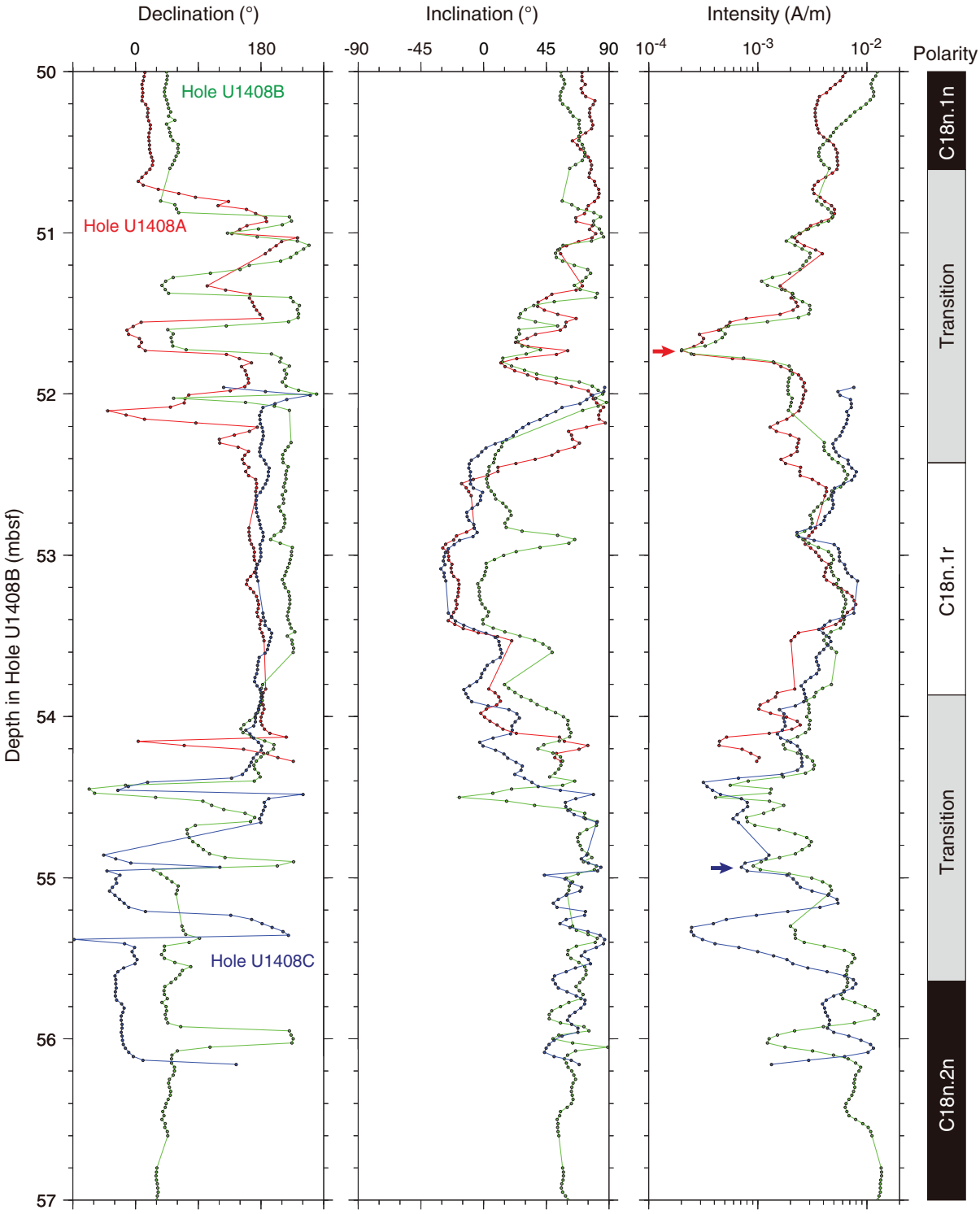

Figure F25. Plots of anisotropy of magnetic susceptibility vs. depth, Hole U1408A. Separation of eigenvalues is related to the shape and degree of the magnetic fabric (see **"Paleomagnetism"** in the "Methods" chapter [Norris et al., 2014a]). For example, if τ_1 and τ_2 are close or indistinguishable but distinct from τ_3, then the bulk fabric is oblate. Lithostratigraphic units are described in **"Lithostratigraphy."** Eigenvalues: τ_1 = maximum, τ_2 = intermediate, τ_3 = minimum. V_3 = minimum eigenvector, P = degree of anisotropy (τ_1/τ_3). APC = advanced piston corer, XCB = extended core barrel.

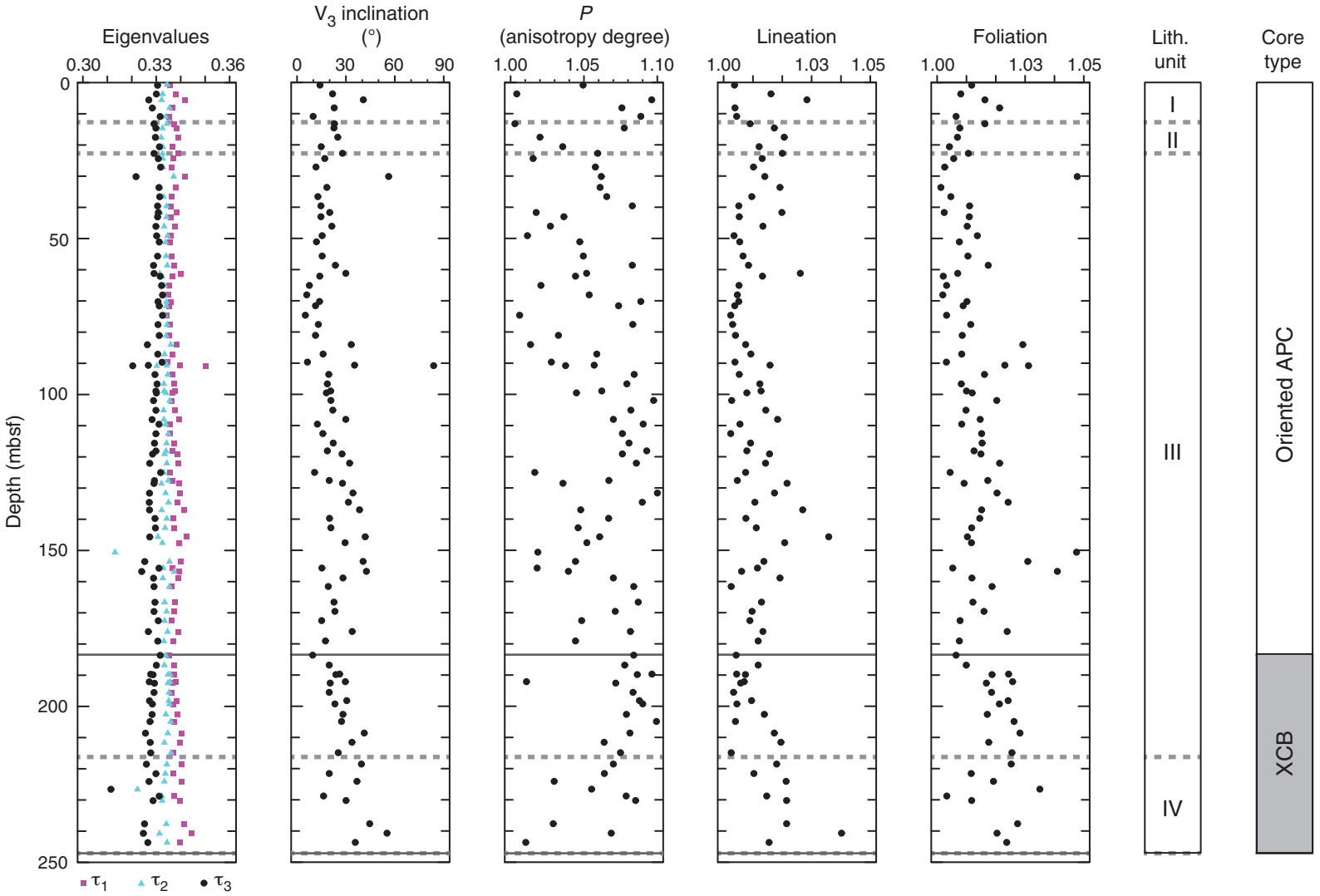

Figure F26. Plots of linear sedimentation rate (LSR), dry bulk density (DBD), carbonate content, and mass accumulation rate (MAR) at a 200 k.y. time step, Hole U1408A. Solid black diamonds are the inflection points in estimated LSR, DBD, and carbonate content. Geologic ages are shown on the GTS2012 timescale (Gradstein et al., 2012). CAR = carbonate mass accumulation rate, nCAR = noncarbonate mass accumulation rate.

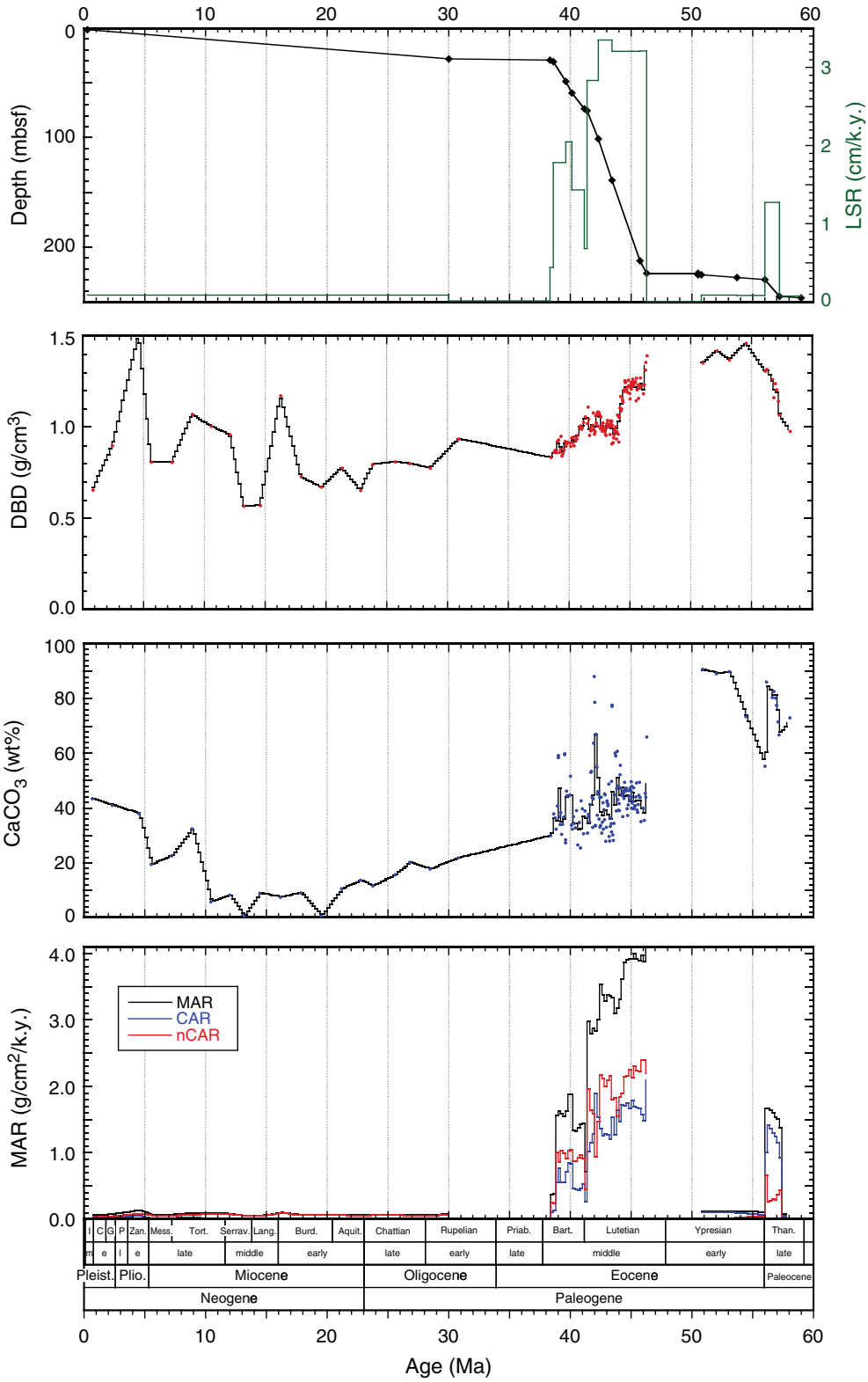

Figure F27. Plots of interstitial water constituent concentrations, Hole U1408A.

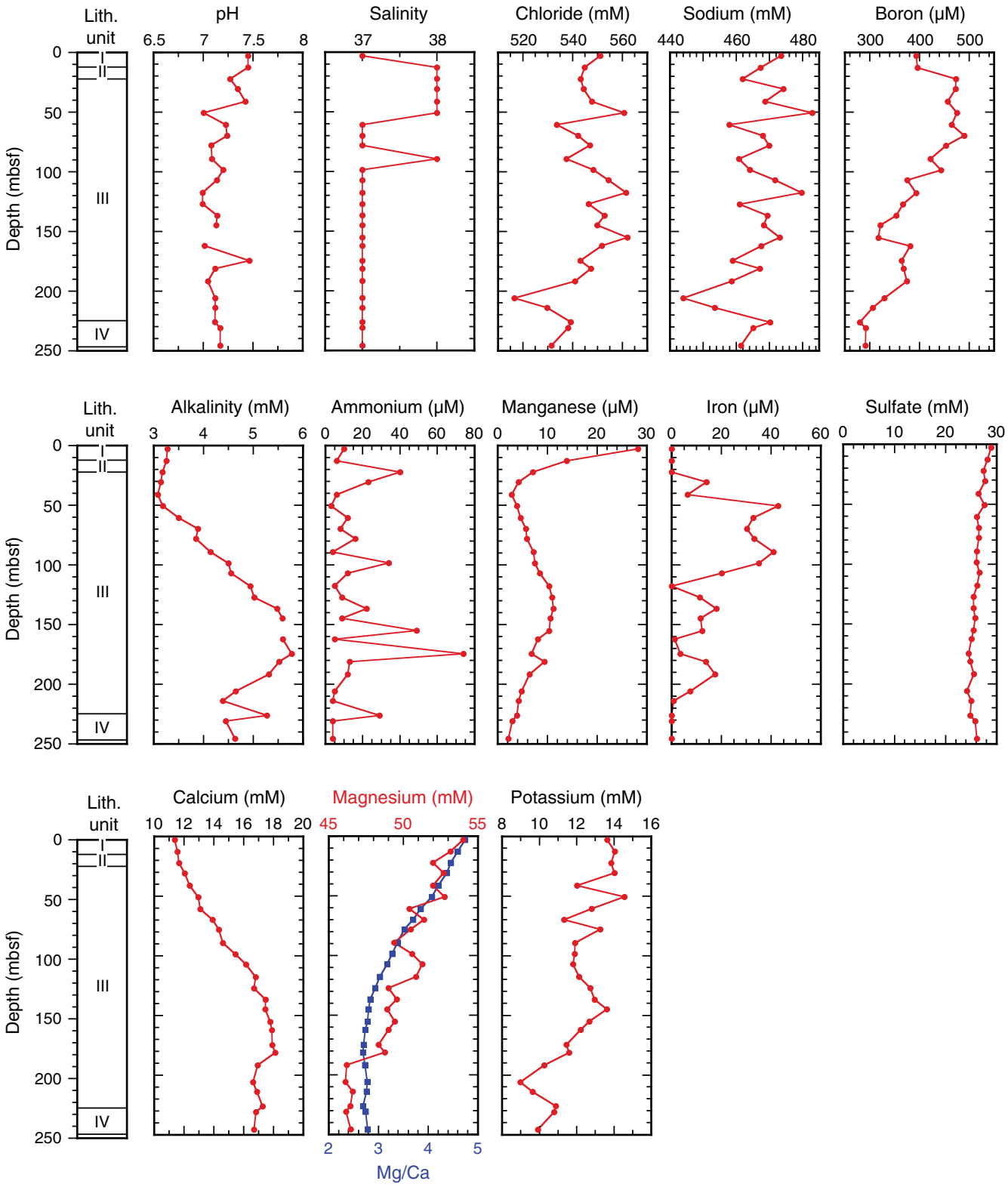

Figure F28. Plots of sedimentary carbonate, total organic carbon (TOC), and total nitrogen, Hole U1408A. Core recovery: black = recovered, white = not recovered, red = core overlap.

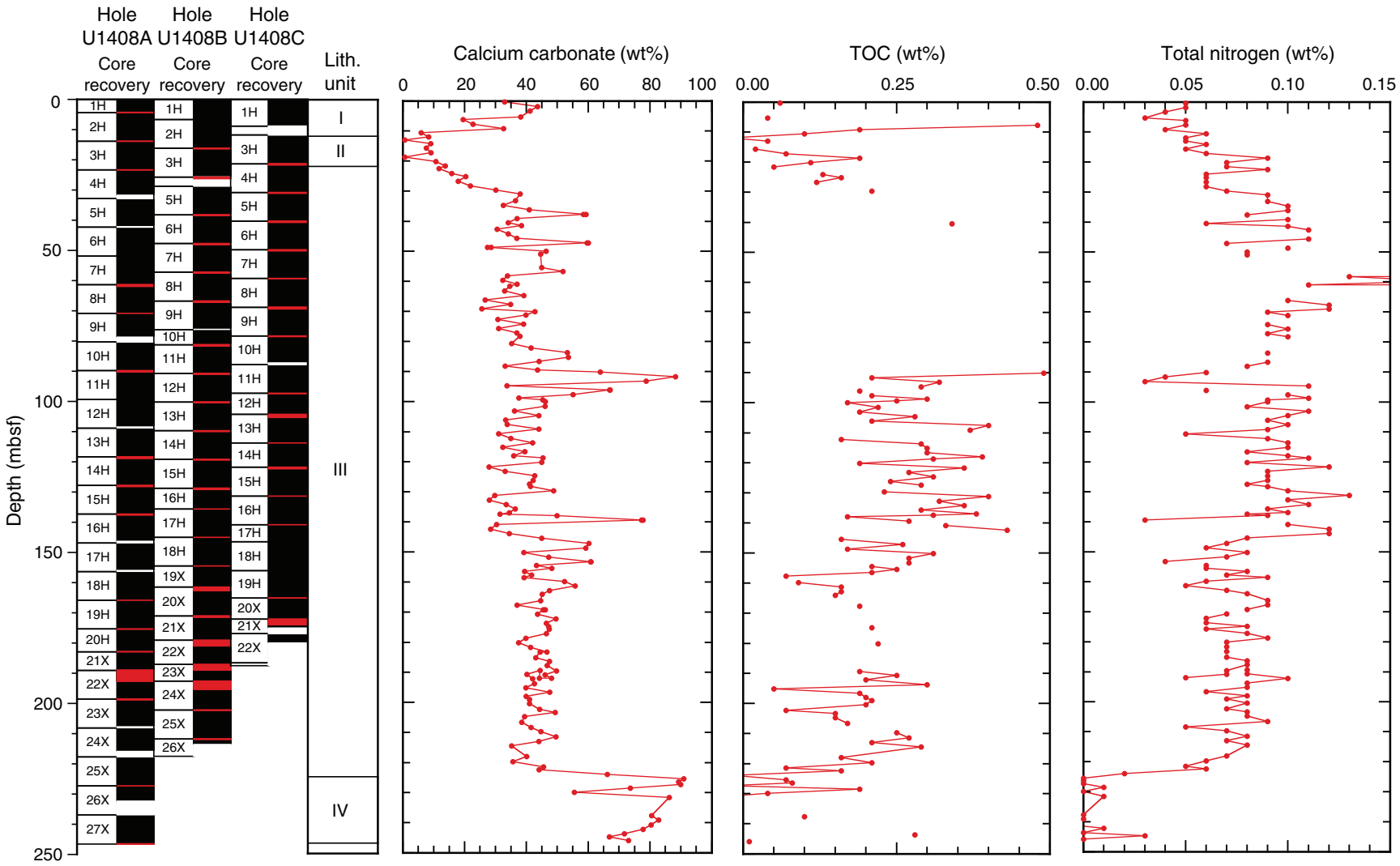

Figure F29. Plots of magnetic susceptibility (MS; truncated at 160 IU), bulk density (gray line = gamma ray attenuation bulk density from Whole-Round Multisensor Logger data, black circles = moisture and density analysis from discrete samples), water content, porosity, and grain density, Site U1408. Core recovery: black = recovered, white = not recovered, red = core overlap. Horizontal gray lines indicate lithostratigraphic unit boundaries (see "Lithostratigraphy"). APC = advanced piston corer, DI = drilled interval, XCB = extended core barrel.

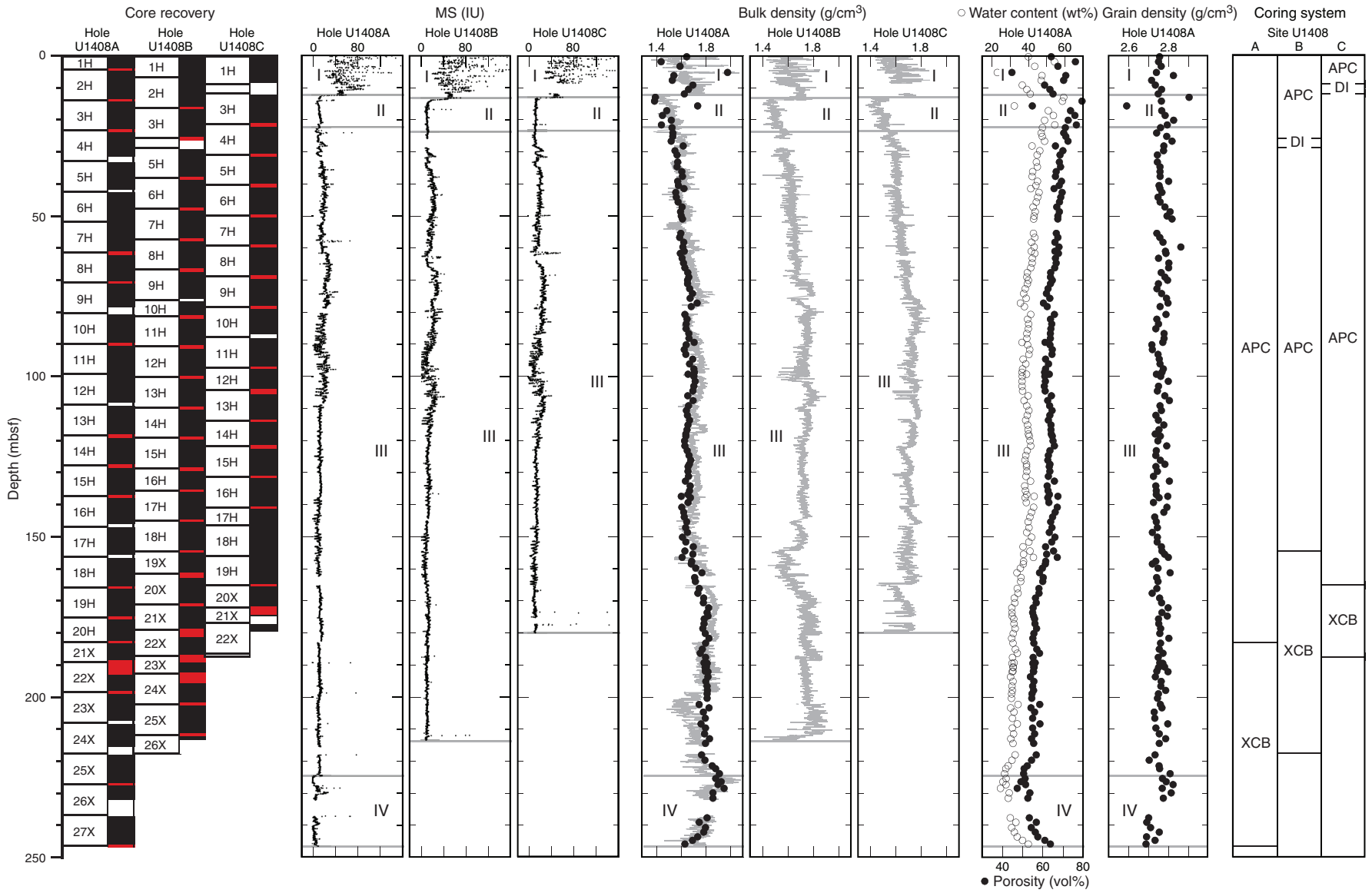

Figure F30. Plots of magnetic susceptibility (MS), *P*-wave velocity (gray line = *P*-wave logger data from whole-round sections, black circles = *P*-wave caliper probe data from section halves), and natural gamma radiation (NGR), Site U1408. Core recovery: black = recovered, white = not recovered, red = core overlap. Horizontal gray lines indicate lithostratigraphic unit boundaries (see **"Lithostratigraphy"**). APC = advanced piston corer, DI = drilled interval, XCB = extended core barrel.

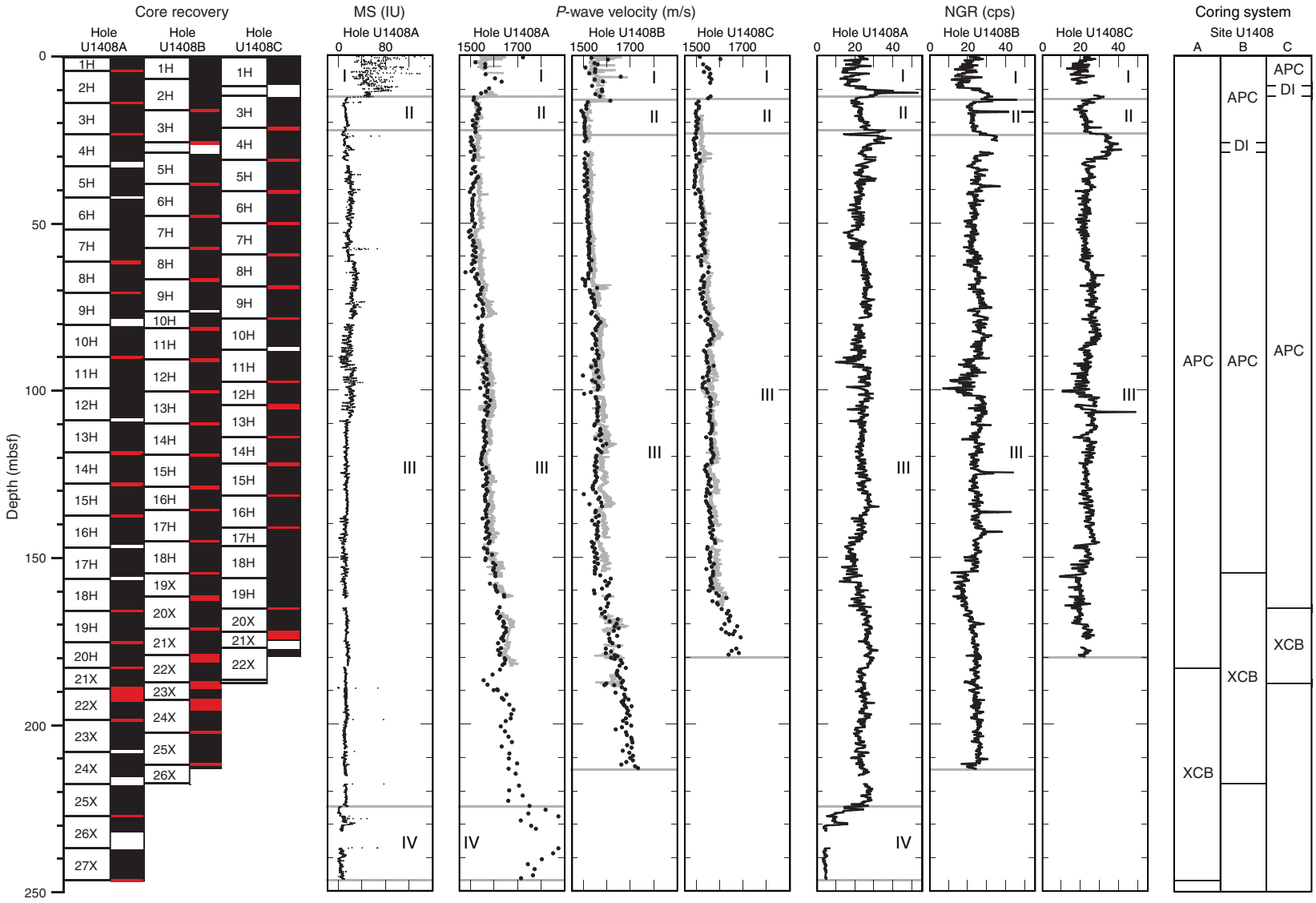

Figure F31. Plots of magnetic susceptibility (MS) and color reflectance (a*, b*, and L*), Site U1408. Core recovery: black = recovered, white = not recovered, red = core overlap. Horizontal gray lines indicate lithostratigraphic unit boundaries (see **"Lithostratigraphy"**). APC = advanced piston corer, DI = drilled interval, XCB = extended core barrel.

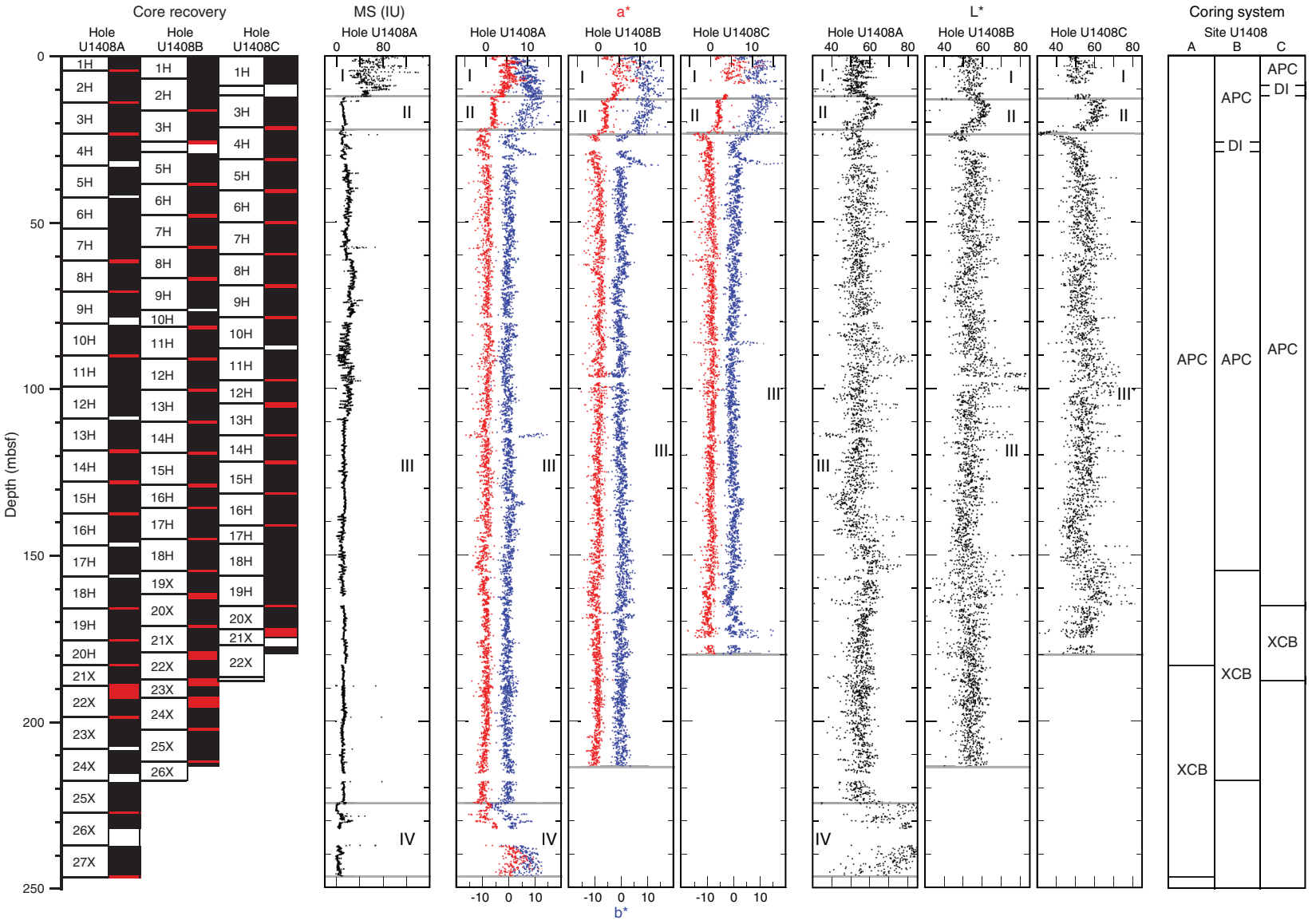

Figure F32. Plot of thermal conductivity measurements, Hole U1408A. Core recovery: black = recovered, white = not recovered, red = core overlap. Blue line is the smooth-curve fit for this data set. Horizontal gray lines indicate lithostratigraphic unit boundaries (see **"Lithostratigraphy"**).

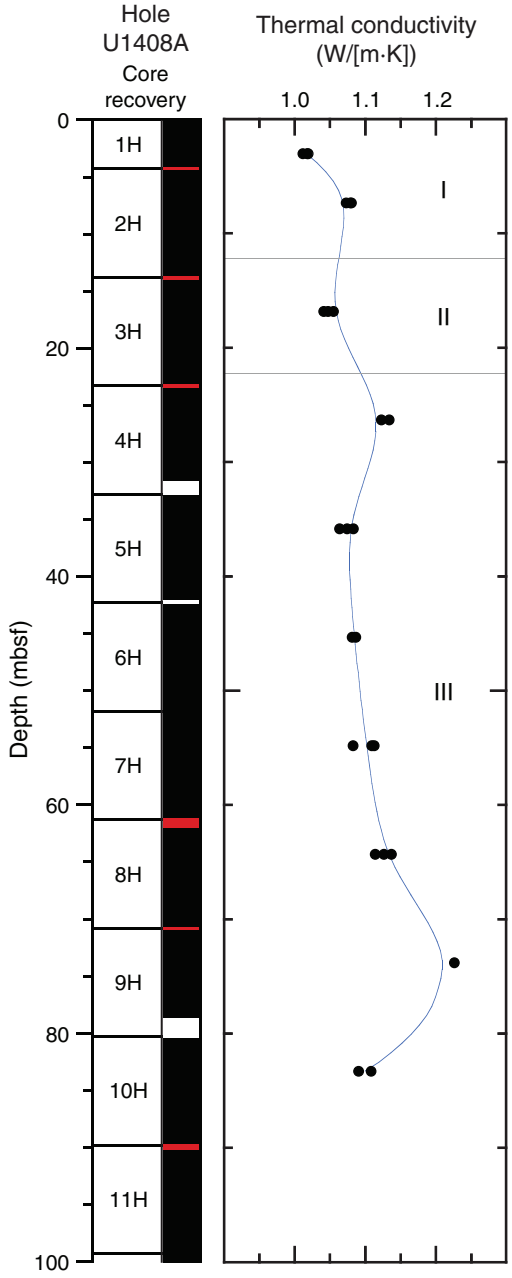

Figure F33. Plot of thermal conductivity vs. gamma ray attenuation (GRA) bulk density, Hole U1408A. Black line is the linear-curve fit for this data set, and R^2 is the correlation coefficient.

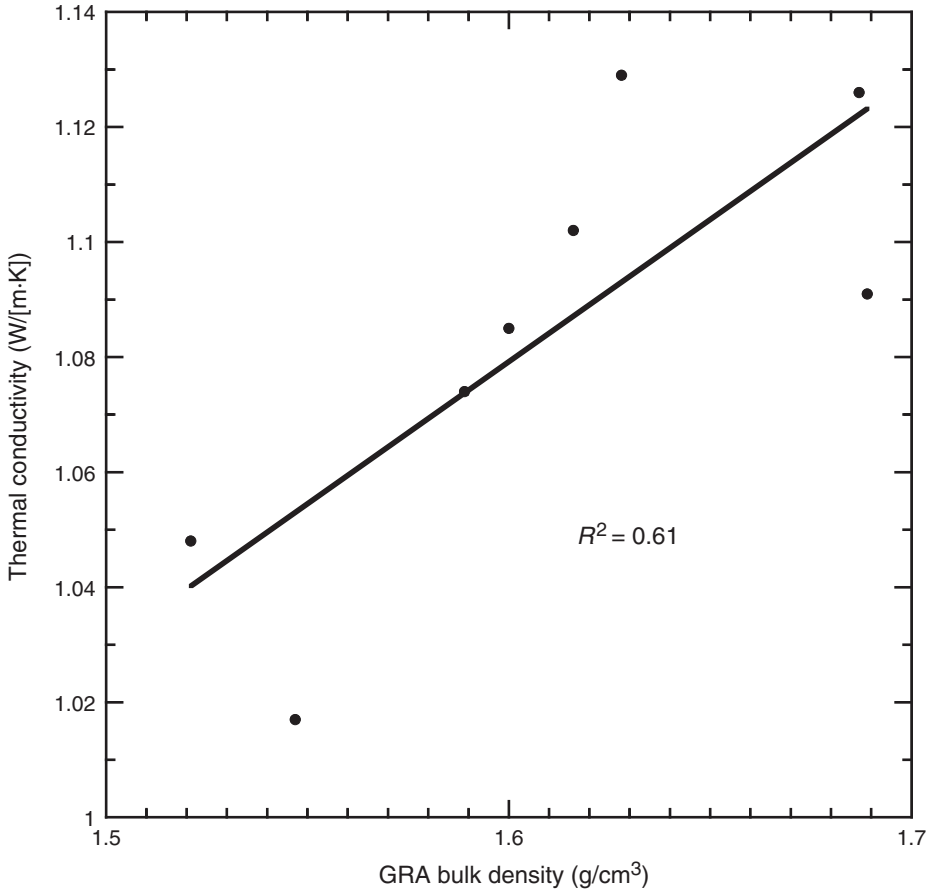

Figure F34. Plots of magnetic susceptibility data, Site U1408. Top panels show the spliced section for each interval of the splice. Bottom panels show complete magnetic susceptibility records. Open circles indicate core tops, excluding culled data from disturbed intervals. **A.** 0–25 m CCSF. Data for Holes U1408B and U1408C are offset by 200 and 400 IU, respectively, to aid visualization. (Continued on next five pages.)

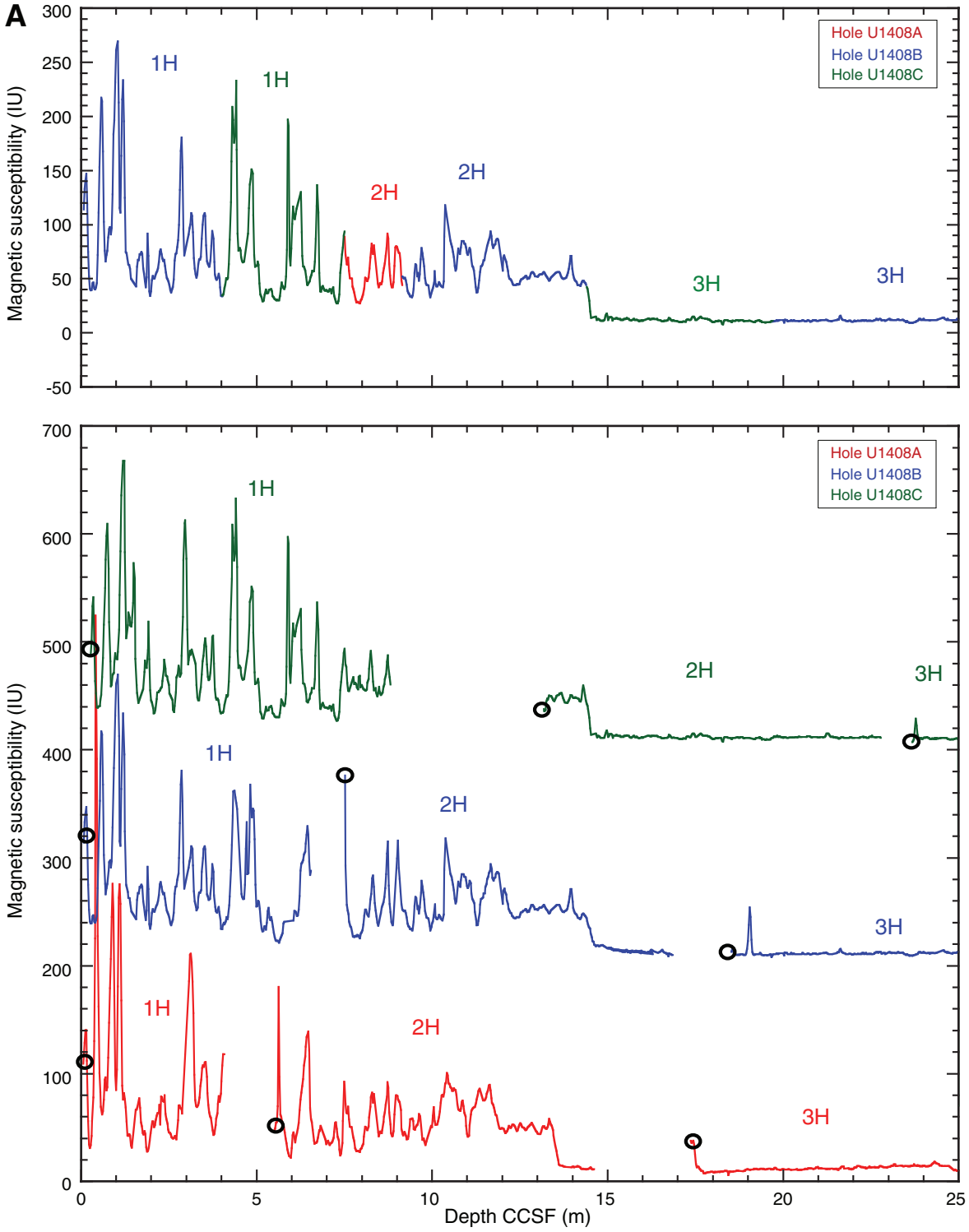

Figure F34 (continued). B. 25–75 m CCSF. Data for Holes U1408B and U1408C are offset by 30 and 60 IU, respectively, to aid visualization. (Continued on next page.)

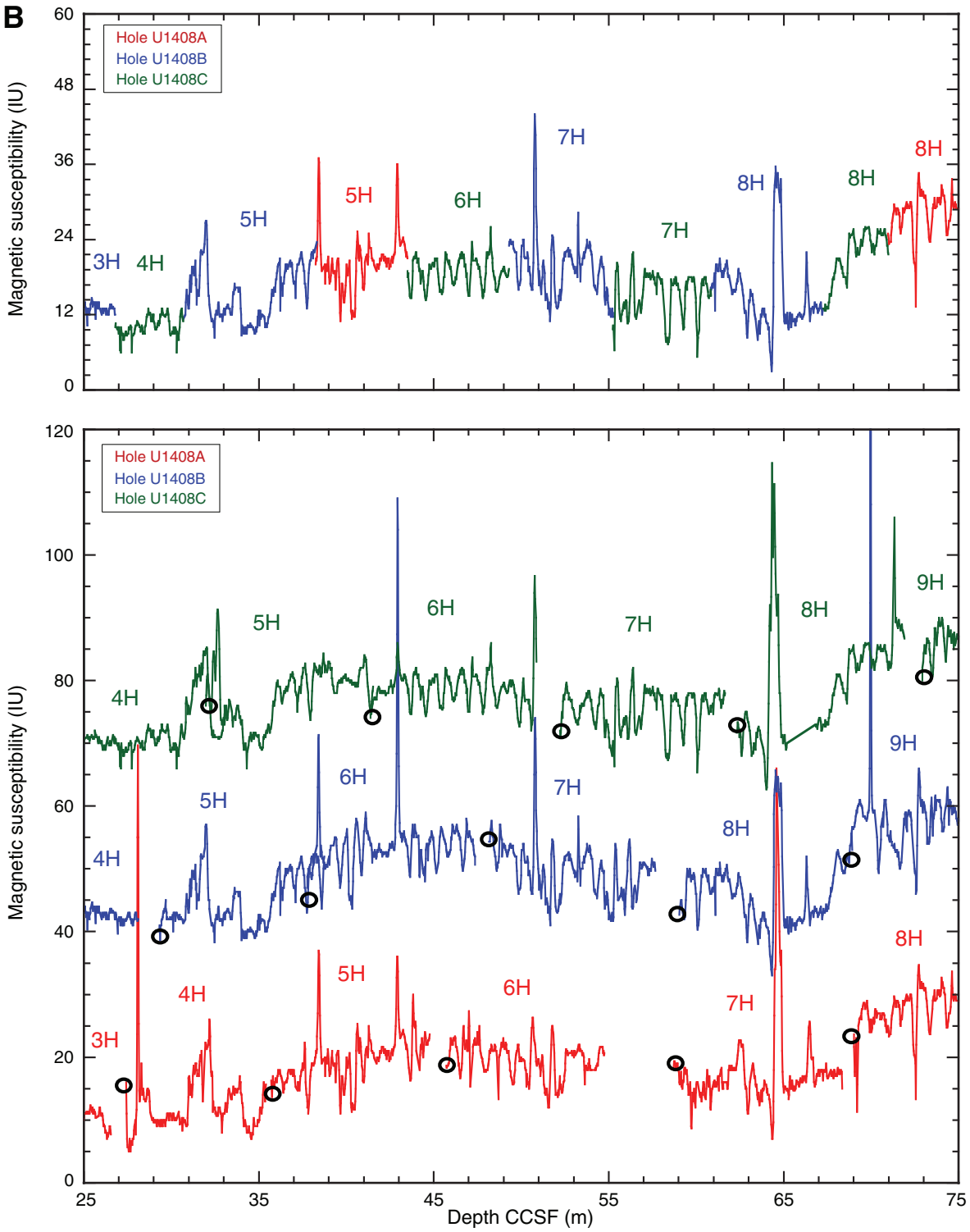

Figure F34 (continued). C. 75–125 m CCSF. Data for Holes U1408B and U1408C are offset by 30 and 60 IU, respectively, to aid visualization. (Continued on next page.)

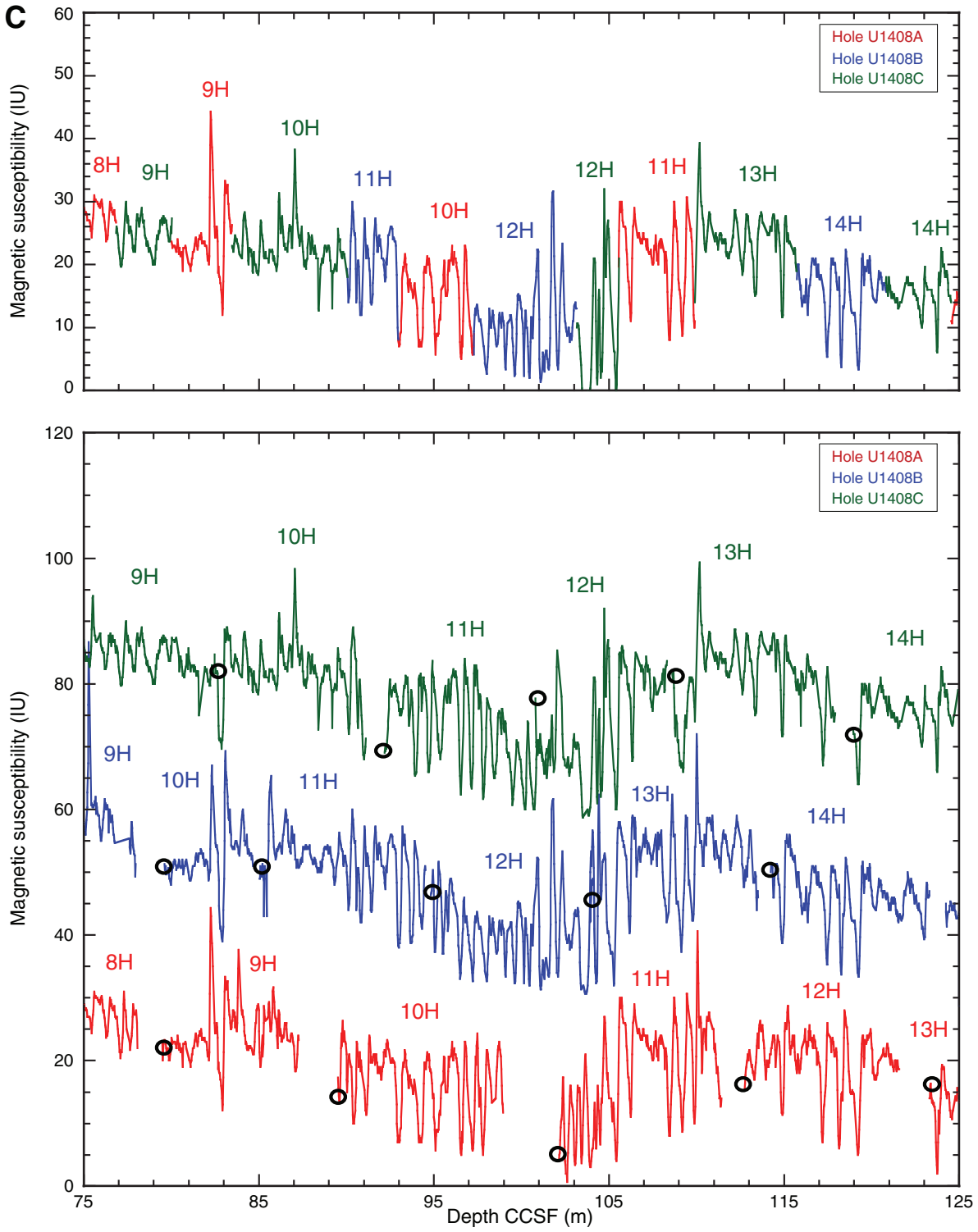

Figure F34 (continued). D. 125–175 m CCSF. Data for Holes U1408B and U1408C are offset by 15 and 30 IU, respectively, to aid visualization. (Continued on next page.)

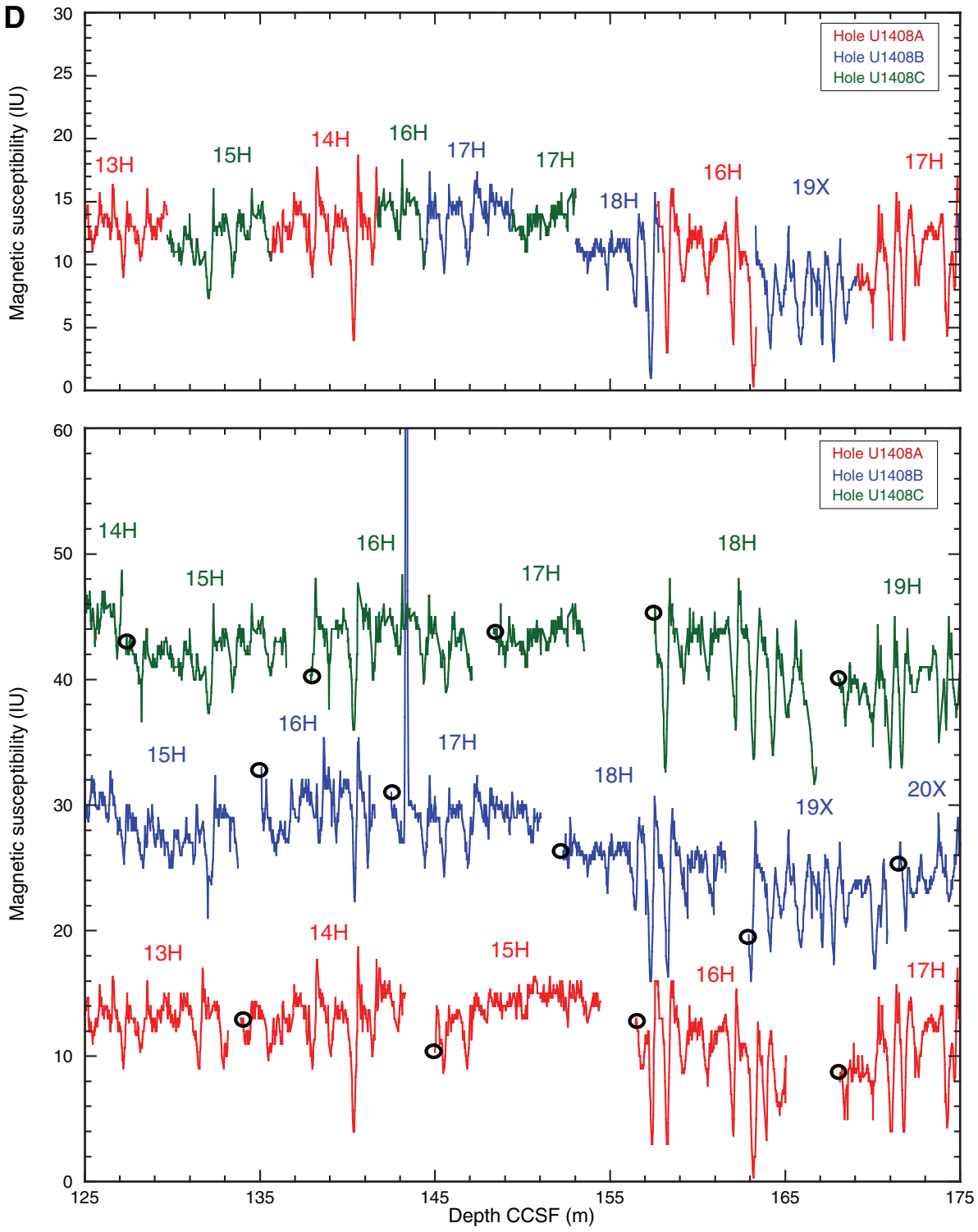

Figure F34 (continued). E. 175–225 m CCSF. Data for Holes U1408B and U1408C are offset by 15 and 30 IU, respectively, to aid visualization. (Continued on next page.)

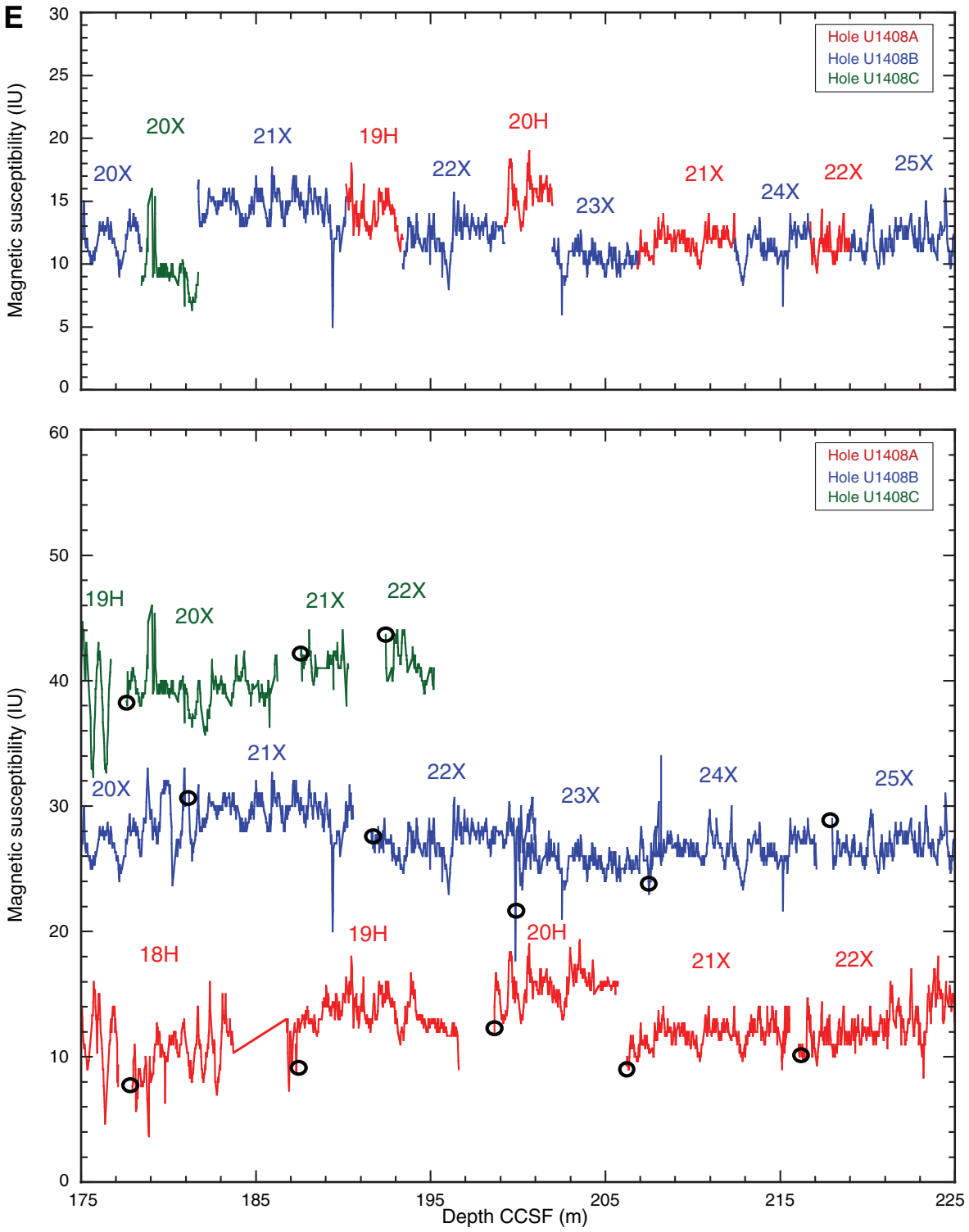

Figure F34 (continued). F. 225–275 m CCSF. Data for Holes U1408B and U1408C are offset by 15 and 30 IU, respectively, to aid visualization.

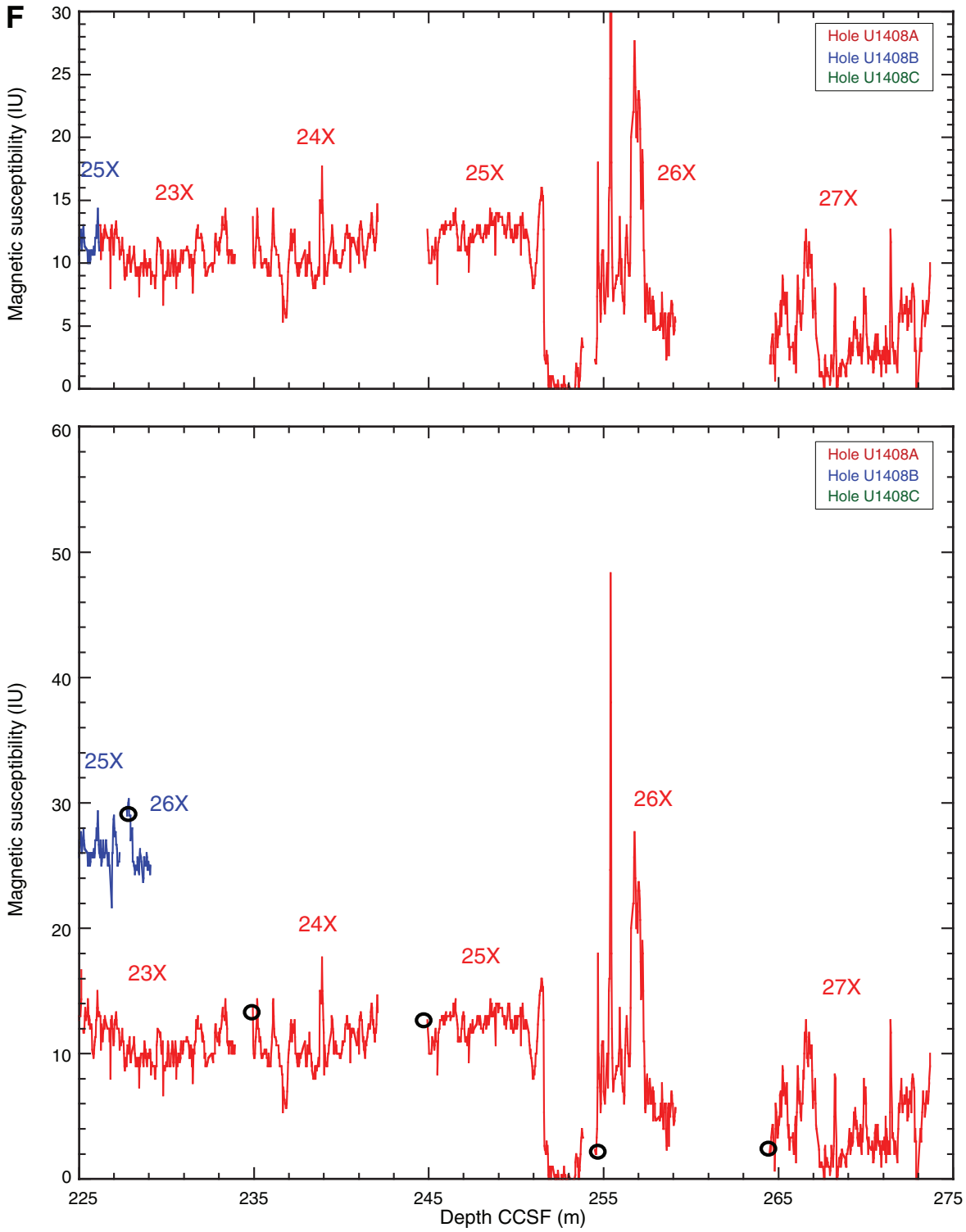

Figure F35. Plot of mbsf depth vs. CCSF depth, Site U1408. The growth factor is equal to the slope of the regression line.

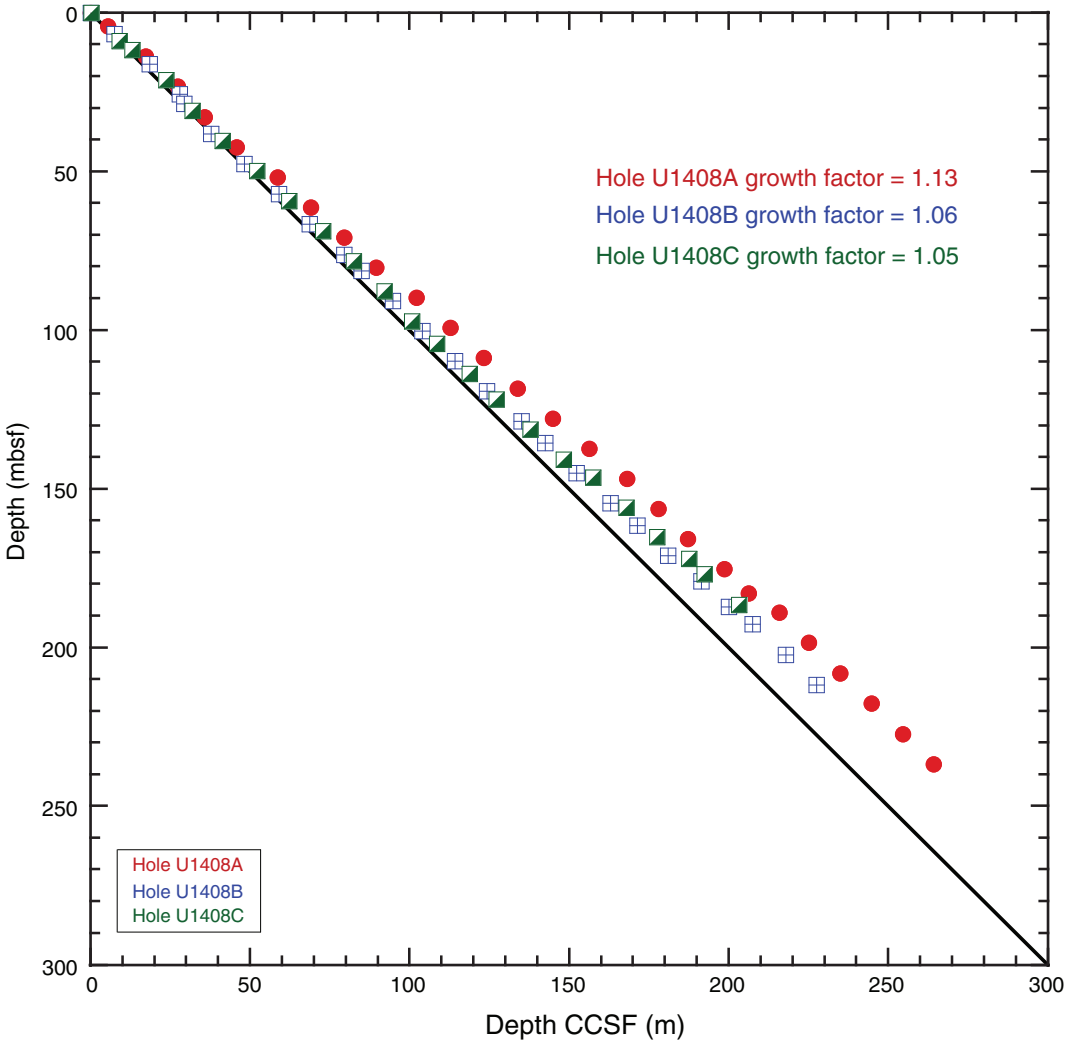

Figure F36. Plots of heat flow calculation, Hole U1408A. **A.** Advanced piston corer temperature tool (APCT-3) sediment temperatures. **B.** Temperature gradient. **C.** Bullard plot in which heat flow is calculated from a linear fit of the temperature data.

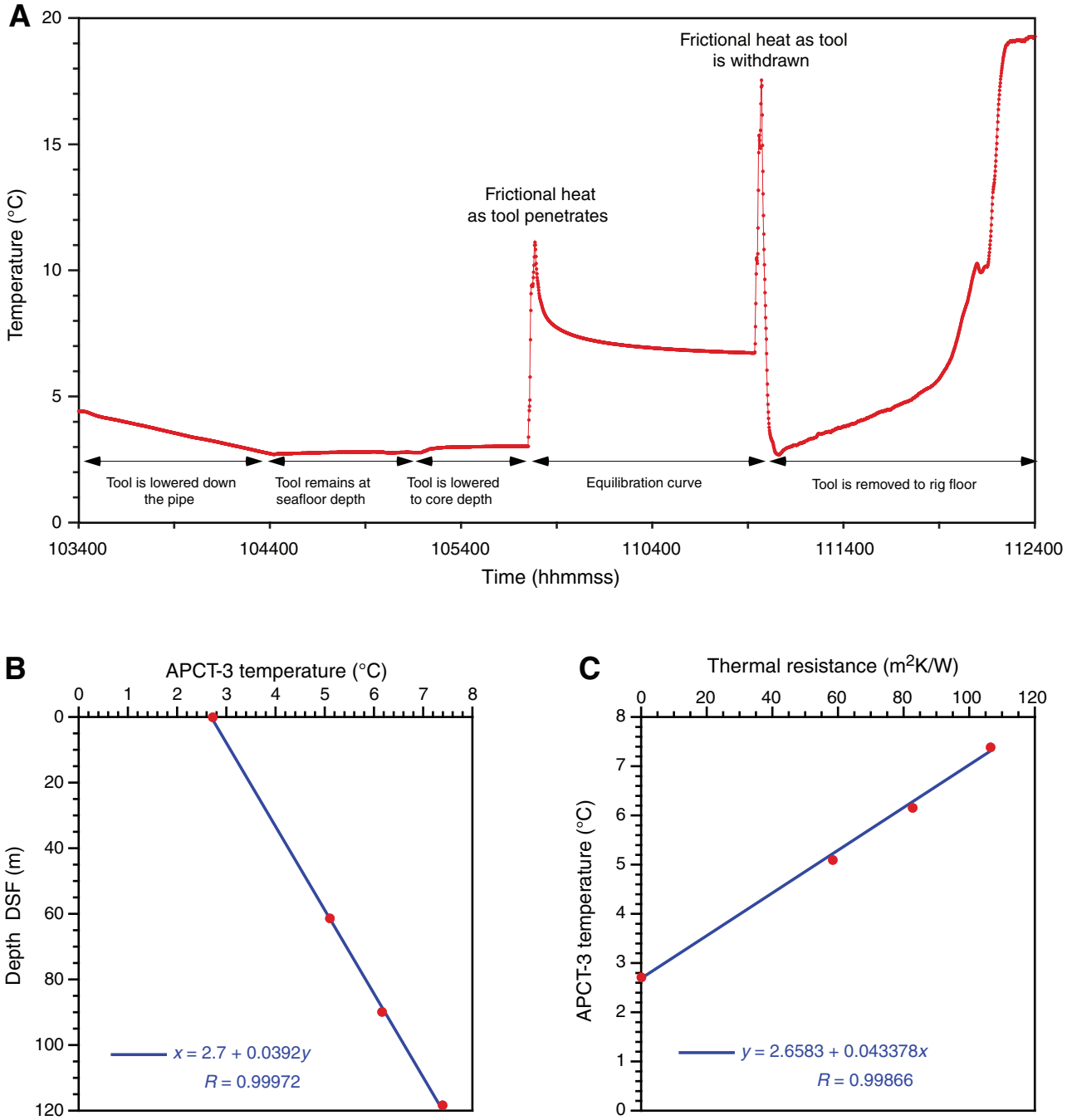

Table T1. Coring summary, Site U1408. (Continued on next page.)

Core	Date (2012)	Time UTC (h)	Depth DSF (m) Top of cored interval	Depth DSF (m) Bottom of cored interval	Interval cored (m)	Curated length (m)	Depth CSF-A (m) Top of core	Depth CSF-A (m) Bottom of core	Recovery (%)	Sections (*N*)
342-U1408A-										
1H	12 Jul	0220	0.0	4.3	4.3	4.38	0.00	4.38	102	4
2H	12 Jul	0320	4.3	13.8	9.5	9.62	4.30	13.92	101	8
3H	12 Jul	0405	13.8	23.3	9.5	9.62	13.80	23.42	101	8
4H	12 Jul	0510	23.3	32.8	9.5	8.53	23.30	31.83	90	7
5H	12 Jul	0555	32.8	42.3	9.5	9.39	32.80	42.19	99	8
6H	12 Jul	0645	42.3	51.8	9.5	9.50	42.30	51.80	100	8
7H	12 Jul	0745	51.8	61.3	9.5	10.19	51.80	61.99	107	8
8H	12 Jul	0925	61.3	70.8	9.5	9.56	61.30	70.86	101	8
9H	12 Jul	1015	70.8	80.3	9.5	8.00	70.80	78.80	84	7
10H	12 Jul	1125	80.3	89.8	9.5	9.93	80.30	90.23	105	8
11H	12 Jul	1235	89.8	99.3	9.5	9.52	89.80	99.32	100	8
12H	12 Jul	1325	99.3	108.8	9.5	9.28	99.30	108.58	98	8
13H	12 Jul	1430	108.8	118.3	9.5	10.07	108.80	118.87	106	8
14H	12 Jul	1525	118.3	127.8	9.5	9.92	118.30	128.22	104	8
15H	12 Jul	1615	127.8	137.3	9.5	9.84	127.80	137.64	104	8
16H	12 Jul	1705	137.3	146.8	9.5	9.14	137.30	146.44	96	7
17H	12 Jul	1755	146.8	156.3	9.5	9.26	146.80	156.06	97	7
18H	12 Jul	1855	156.3	165.8	9.5	9.55	156.30	165.85	101	8
19H	12 Jul	2050	165.8	175.3	9.5	9.64	165.80	175.44	101	8
20H	12 Jul	2200	175.3	182.9	7.6	7.66	175.30	182.96	101	6
21X	13 Jul	2350	182.9	189.0	6.1	9.85	182.90	192.75	161	8
22X	13 Jul	0130	189.0	198.5	9.5	9.81	189.00	198.81	103	8
23X	13 Jul	0340	198.5	208.1	9.6	9.32	198.50	207.82	97	7
24X	13 Jul	0545	208.1	217.7	9.6	7.84	208.10	215.94	82	6
25X	13 Jul	0805	217.7	227.3	9.6	9.64	217.70	227.34	100	8
26X	13 Jul	1005	227.3	236.9	9.6	5.12	227.30	232.42	53	5
27X	13 Jul	1155	236.9	246.5	9.6	9.74	236.90	246.64	101	8
				Totals:	265.5	243.92			100	200
342-U1408B-										
1H	13 Jul	1520	0.0	6.7	6.7	6.74	0.00	6.74	101	6
2H	13 Jul	1715	6.7	16.2	9.5	9.72	6.70	16.42	102	8
3H	13 Jul	1825	16.2	25.7	9.5	10.05	16.20	26.25	106	8
41	13 Jul	1845			****Drilled from 25.7 to 28.7 m DSF****					
5H	13 Jul	1955	28.7	38.2	9.5	9.81	28.70	38.51	103	8
6H	13 Jul	2105	38.2	47.7	9.5	9.93	38.20	48.13	105	8
7H	13 Jul	2150	47.7	57.2	9.5	9.87	47.70	57.57	104	8
8H	13 Jul	2030	57.2	66.7	9.5	10.09	57.20	67.29	106	8
9H	13 Jul	2315	66.7	76.2	9.5	9.48	66.70	76.18	100	9
10H	14 Jul	0100	76.2	81.2	5.0	5.51	76.20	81.71	110	5
11H	14 Jul	0205	81.2	90.7	9.5	9.86	81.20	91.06	104	8
12H	14 Jul	0245	90.7	100.2	9.5	9.75	90.70	100.45	103	8
13H	14 Jul	0330	100.2	109.7	9.5	9.80	100.20	110.00	103	8
14H	14 Jul	0415	109.7	119.2	9.5	9.72	109.70	119.42	102	8
15H	14 Jul	0500	119.2	128.7	9.5	9.99	119.20	129.19	105	8
16H	14 Jul	0545	128.7	135.6	6.9	6.96	128.70	135.66	101	6
17H	14 Jul	0640	135.6	145.0	9.4	9.47	135.60	145.07	101	8
18H	14 Jul	0755	145.0	154.5	9.5	9.59	145.00	154.59	101	8
19X	14 Jul	0915	154.5	161.5	7.0	8.16	154.50	162.66	117	7
20X	14 Jul	1010	161.5	171.1	9.6	9.97	161.50	171.47	104	8
21X	14 Jul	1105	171.1	179.1	8.0	9.93	171.10	181.03	124	8
22X	14 Jul	1210	179.1	187.1	8.0	9.94	179.10	189.04	124	8
23X	14 Jul	1315	187.1	192.6	5.5	8.35	187.10	195.45	152	7
24X	14 Jul	1430	192.6	202.2	9.6	9.71	192.60	202.31	101	8
25X	14 Jul	1610	202.2	211.8	9.6	9.79	202.20	211.99	102	8
26X	14 Jul	1800	211.8	217.5	5.7	1.90	211.80	213.70	33	3
				Totals:	217.5	224.09			101	187
342-U1408C-										
1H	14 Jul	2155	0.0	8.8	8.8	8.85	0.00	8.85	101	7
21	14 Jul	2215			****Drilled from 8.8 to 11.8 m DSF****					
3H	14 Jul	2240	11.8	21.3	9.5	9.99	11.80	21.79	105	8
4H	14 Jul	2320	21.3	30.8	9.5	9.84	21.30	31.14	104	8
5H	15 Jul	0009	30.8	40.3	9.5	9.97	30.80	40.77	105	8
6H	15 Jul	0130	40.3	49.8	9.5	9.90	40.30	50.20	104	8
7H	15 Jul	0220	49.8	59.3	9.5	9.62	49.80	59.42	101	7
8H	15 Jul	0310	59.3	68.8	9.5	10.07	59.30	69.37	106	8

Table T1. (continued).

Core	Date (2012)	Time UTC (h)	Depth DSF (m) Top of cored interval	Depth DSF (m) Bottom of cored interval	Interval cored (m)	Curated length (m)	Depth CSF-A (m) Top of core	Depth CSF-A (m) Bottom of core	Recovery (%)	Sections (*N*)
9H	15 Jul	0455	68.8	78.3	9.5	9.79	68.80	78.59	103	7
10H	15 Jul	0830	78.3	87.8	9.5	9.04	78.30	87.34	95	7
11H	15 Jul	1235	87.8	97.3	9.5	9.70	87.80	97.50	102	7
12H	15 Jul	1325	97.3	104.3	7.0	8.03	97.30	105.33	115	7
13H	15 Jul	1410	104.3	113.8	9.5	9.59	104.30	113.89	101	8
14H	15 Jul	1455	113.8	121.8	8.0	8.55	113.80	122.35	107	6
15H	15 Jul	1530	121.8	131.3	9.5	9.59	121.80	131.39	101	7
16H	15 Jul	1615	131.3	140.8	9.5	9.55	131.30	140.85	101	7
17H	15 Jul	1655	140.8	146.5	5.7	5.71	140.80	146.51	100	5
18H	15 Jul	1740	146.5	156.0	9.5	9.54	146.50	156.04	100	7
19H	15 Jul	1830	156	165.1	9.1	9.19	156.00	165.19	101	7
20X	15 Jul	2010	165.1	172.1	7.0	9.19	165.10	174.04	128	7
21X	15 Jul	2135	172.1	176.9	4.8	3.00	172.10	175.10	63	3
22X	15 Jul	2355	176.9	186.5	9.6	3.06	176.90	179.96	32	3
23X	16 Jul	0125	186.5	187.5	1.0	3.06	186.50	189.56		0
				Totals:	187.5	184.83			94	142
				Site U1408 totals:	651.5	652.84			98	529

DSF = drilling depth below seafloor, CSF-A = core depth below seafloor, method A. H = advanced piston core, X = extended core barrel core, numeric core type = drilled interval.

Table T2. Lithostratigraphic unit intervals, Site U1408.

Lith. unit	Core, section, interval (cm) Top	Core, section, interval (cm) Bottom	Depth (mbsf) Top	Depth (mbsf) Bottom
	342-U1408A-	342-U1408A-		
I	1H-1, 0	2H-6, 42	0.00	12.22
II	2H-6, 42	3H-6, 92	12.22	22.22
III	3H-6, 92	25X-5, 94	22.22	224.64
IV	25X-5, 94	27X-CC, 25	224.64	246.64
	342-U1408B-	342-U1408B-		
I	1H-1, 0	2H-5, 52	0.00	13.22
II	2H-5, 52	3H-5, 150	13.22	23.72
III	3H-5, 150	26X-CC, 25*	23.72	213.70*
	342-U1408C-	342-U1408C-		
I	1H-1, 0	3H-1, 113	0.00	12.93
II	3H-1, 113	4H-2, 57	12.93	23.37
III	4H-2, 57	22X-CC, 51	23.37	179.96*

* = base of Unit III not recovered

Table T3. Calcareous nannofossil datums, Site U1408. (Continued on next page.)

Core, section, interval (cm)		Age	Zone/ Subzone	Marker species	Age (Ma)	Depth (mbsf)			
Top	Bottom					Top	Bottom	Midpoint	±
342-U1408A-	342-U1408A-								
		Pleistocene							
1H-1, 75	1H-2, 75		NN21	Ba *Emiliania huxleyi*	0.29	0.75	2.25	1.50	0.75
1H-CC	2H-3, 100		NN20	T *Pseudoemiliania lacunosa*	0.44	4.33	8.30	6.32	1.99
2H-3, 100	2H-4, 100		NN19	T *Discoaster brouweri*	1.93	8.30	9.80	9.05	0.75
		Miocene							
2H-4, 100	2H-5, 100		NN9	T *Discoaster hamatus*	9.53	9.80	11.30	10.55	0.75
2H-4, 100	2H-5, 100			T *Catinaster coalitus*	9.69	9.80	11.30	10.55	0.75
2H-5, 100	2H-CC			B *Discoaster hamatus*	10.55	11.30	13.87	12.59	1.29
2H-5, 100	2H-CC			B *Catinaster calyculus*	10.79	11.30	13.87	12.59	1.29
		Oligocene							
4H-3, 100	4H-4, 100			B *Sphenolithus distentus*	30.00	27.31	28.81	28.06	0.75
4H-3, 100	4H-4, 100		NP23	T *Reticulofenestra umbilicus* (>14 µm)	32.02	27.31	28.81	28.06	0.75
4H-3, 100	4H-4, 100		NP22	T *Coccolithus formosus*	32.92	27.31	28.81	28.06	0.75
		Eocene							
4H-4, 100	4H-4, 100			T *Chiasmolithus grandis*	37.98	28.81	28.81	28.81	0.00
8H-2, 100	8H-3, 100			B *Dictyococcites bisectus* (>10 µm)*	40.36	63.81	65.31	64.56	0.75
7H-6, 100	7H-CC		NP17	T *Chiasmolithus solitus*	40.40	60.31	61.94	61.13	0.81
11H-6, 90	11H-CC			B *Reticulofenestra reticulata*	41.66	98.22	99.27	98.75	0.52
12H-CC	13H-4, 56			T *Nannotetrina* spp.	41.85	108.53	118.84	113.69	5.16
14H-CC	15H-2, 100			B *Reticulofenestra umbilicus* (>14 µm)	41.94	128.20	130.31	129.25	1.06
15H-2, 100	15H-CC			T *Nannotetrina fulgens*	42.87	130.31	137.61	133.96	3.65
17H-3, 75	17H-5, 110		NP15c	T *Chiasmolithus gigas*	44.12	150.55	153.92	152.24	1.68
20H-CC	21X-CC			B *Sphenolithus furcatolithoides*		182.74	192.725	187.73	4.99
23X-1, 75	23X-3, 75		NP15b	B *Chiasmolithus gigas*	45.49	199.49	202.25	200.87	1.38
25X-4, 100	25X-5, 100		NP15a	B *Nannotetrina fulgens*	46.29	223.21	224.70	223.96	0.75
25X-4, 100	25X-5, 100			B *Nannotetrina cristata*	47.73	223.21	224.70	223.96	0.75
25X-4, 100	25X-5, 100			T *Discoaster lodoensis*	47.41	223.21	224.70	223.96	0.75
25X-5, 100	25X-6, 80		NP14	B *Discoaster sublodoensis* (5 rayed)	49.11	224.70	226.00	225.35	0.65
25X-4, 100	25X-5, 100			B *Dictyococcites/Reticulofenestra*	50.50	223.21	224.70	223.96	0.75
25X-5, 100	25X-6, 80		NP13	T *Tribrachiatus orthostylus*	50.50	224.70	226.00	225.35	0.65
25X-5, 100	25X-6, 80			T *Toweius* spp.†	50.78	224.70	226.00	225.35	0.65
26X-1, 34	26X-2, 13		NP12	B *Discoaster lodoensis*	53.70	227.64	228.12	227.88	0.24
26X-2, 13	26X-2, 35			B *Tribrachiatus orthostylus*	54.37	228.12	228.34	228.23	0.11
26X-2, 86	26X-2, 128			B *Discoaster diastypus*	54.95	228.85	229.27	229.06	0.21
26X-2, 137	26X-2, 145			T *Fasciculithus* spp.	55.64	229.36	229.44	229.40	0.04
26X-2, 145	26X-2, 150		NP10	B *Rhomboaster bramlettei*	55.86	229.44	229.49	229.47	0.03
		Paleocene							
26X-3, 16	26X-3, 44			*Fasciculithus* diversity decline‡	56.00	229.93	229.93	229.93	0.00
26X-3, 16	26X-3, 44			T *Fasciculithus alanii*‡	56.00	229.65	229.93	229.79	0.14
26X-CC	27X-5, 97			T *Ericsonia robusta* (>9 µm)‡	57.10	232.38	243.88	238.13	5.75
27X-5, 97	27X-6, 79		NP9	B *Discoaster multiradiatus*	57.21	243.88	245.19	244.54	0.66
27X-5, 97	27X-6, 79			Tc *Sphenolithus anarrhopus*		243.88	246.59	245.23	1.36
27X-6, 79	27X-CC			B *Discoaster delicatus*‡	57.45	245.19	246.59	245.89	0.70
27X-6, 79	27X-CC			B *Ericsonia robusta* (>9 µm)‡	57.54	245.19	246.59	245.89	0.70
27X-5, 97	27X-6, 79			Tc *Discoaster backmanii*‡	57.57	243.88	245.19	244.53	0.66
27X-CC	27X-CC			B *Discoaster backmanii*‡	58.28	246.59	246.59	246.59	0.00

Table T3 (continued).

Core, section, interval (cm)			Zone/		Age	Depth (mbsf)			
Top	Bottom	Age	Subzone	Marker species	(Ma)	Top	Bottom	Midpoint	±
		Paleocene							
27X-CC	27X-CC		NP7	B *Discoaster mohleri*	58.97	246.59	246.59	246.59	0.00

* = from Fornaciari et al. (2010) recalibrated to GTS2012. † = from Agnini et al. (2006) recalibrated to GTS2012. ‡ = from Agnini et al. (2007) recalibrated to GTS2012. B = base, Ba = base of acme, Bc = base common, T = top, Tc = top common.

Table T4. Nannofossils distribution, Site U1408. This table is available in an **oversized format.**

Table T5. Radiolarian datums, Site U1408.

Core, section, interval (cm)				Age	Depth (mbsf)			
Top	Bottom	Zone	Marker species	(Ma)	Top	Bottom	Mid-point	±
342-U1408A-	342-U1408A-							
16H-6W, 78–80			T *Calocyclas tripocha*	43.38	144.29		144.29	
16H-7-CC	17H-3W, 69–71	RP13	T *Podocyrtis dorus*	43.81	145.09	150.50	147.80	
17H-3W, 69–71	25X-CC		B *Calocyclas tripocha*	44.46	150.50	227.29	188.90	38.40
26X-1W, 54–55	26X-4W, 85–86		T *Amphisphaera goruna*	55.50	227.85	231.85	229.85	2.00
27X-CC		RP7	X *Bekoma campechensis – Bekoma bidartensis*	58.23	246.59		246.59	
		Unzoned			0.00	144.29		
		RP13			144.29	150.50		
		Unzoned			150.50	231.85		
		RP7			231.85	246.59		

B= base, T = top, X = faunal crossover.

Table T6. Radiolarian distribution, Site U1408.

Core, section, interval (cm)	Depth (mbsf)	Age	Zone/ Subzone	Preservation	Abundance	*Amphicraspedum murrayanum*	*Ampicraspedum prolixum*	*Amphipternis alamedaensis*	*Amphisphaera coronata*	*Amphisphaera goruna*	*Amphisphaera macrosphaera*	*Axoprunum pierinae*	*Bekoma bidartensis*	*Buryella tetradica*	*Calocyclas hispida*	*Calocyclas trichopa*	*Calocycloma ampulla*	*Calocycloma castum*	*Cassideus mariae*	*Clathrocyclas australis*	*Clathrocyclas universa*	*Dictyophimus craticula*	*Dictyoprora amphora*	*Dictyoprora mongolfieri*	*Diplocyclas bicorona bicorona*	*Dorcadospyris platyacantha*	*Eusyringium fistuligerum*	*Eusyringium lagena*	*Lamptonium pennatum*	*Lithapium aneoctum*	*Lithapium plegmacantha*	*Lithochytris vespertilio*	*Lithomespilus mendosa*	*Lophocyrtis klydus*	*Lophocyrtis semipolita* gr.	*Lophocyrtis? biaurita*	*Lophocyrtis? pseudojacchia*	*Lychnocanoma amphitrite*	*Lychnocanoma auxilla*	*Lychnocanoma bajunensis*	*Lychnocanoma bellum*	*Lychnocanoma carinatum*	*Orbula comitata*
342-U1408A-																																									
16H-6, 78–80	144.29	middle Eocene	RP12	M	A				F							R	R	R				F		R			P	P			C				P		F		R	F		
16H-7-CC	145.09	middle Eocene	RP13	G	A				F						R	F					F	R	F	F			P	R					P		R				R	R		
17H-3, 69–71	150.50	middle Eocene	RP13	G	A				F					R	R	R	F	R					F	F				R		R	P			P		R		R	P	R			
25X-CC	227.29	Eocene	?	M	R									P						P			P																			
26X-1, 54–55	227.85	Eocene	?	M	R																		P																			
26X-4, 85–86	231.85	late Paleocene	RP7	M	C				P	P	P		P	P						R	R				R							P			P			P		P	P	
26X-CC	232.38	late Paleocene	RP7	M	A	R	P		R	R	R		F	F						R	R				R	R			P			R			P			R		F		
27X-CC	246.59	late Paleocene	RP7	G	A	R		R	R	R	F	P	F	C						R					R	R						R						R		F		

Preservation: G = good, M = moderate. Abundance: A = abundant, C = common, F = few, R = rare, P = present, ? = questionable. See **"Biostratigraphy"** in the "Methods" chapter (Norris et al., 2014a) for preservation and abundance definitions.

Core, section, interval (cm)	Depth (mbsf)	Age	Zone/ Subzone	Preservation	Abundance	*Periphaena decora*	*Periphaena heliasteriscus*	*Periphaena tripyramis triangula*	*Phormocyrtis cubensis*	*Phormocyrtis striata exquisita*	*Phormocyrtis striata praexquisita*	*Phormocyrtis striata striata*	*Phormocyrtis turgida*	*Podocyrtis acelles*	*Podocyrtis dorus*	*Podocyrtis papalis*	*Podocyrtis sinuosa*	*Pterocodon poculum*	*Pterocyrtidium genriettae*	*Sethochytris babylonis*	*Spongatractus balbis*	*Stylotrochus nitidis*	*Theocorys phyzella*	*Theocorys* aff. *phyzella*	*Theocotyle nigriniae*	*Theocotylissa ficus*	*Thyrsocyrtis rhizodon*	*Thyrsocyrtis triacantha*	*Xiphospira circularis*
342-U1408A-																													
16H-6, 78–80	144.29	middle Eocene	RP12	M	A		P										C			R	R						F	R		
16H-7-CC	145.09	middle Eocene	RP13	G	A	R	R	R				R				F	F			F						R	F	C		
17H-3, 69–71	150.50	middle Eocene	RP13	G	A	P	R	P				R			R	R	F			F	R				P	R	F	F		
25X-CC	227.29	Eocene	?	M	R																									
26X-1, 54–55	227.85	Eocene	?	M	R									?												P				
26X-4, 85–86	231.85	late Paleocene	RP7	M	C					P										P	P			P						
26X-CC	232.38	late Paleocene	RP7	M	A				R	F		R	R			R		F	R	R	P	F	F	C					F	
27X-CC	246.59	late Paleocene	RP7	G	A					F	R	R				R		R				F	F	C					F	

Table T7. Planktonic foraminifer datums, Site U1408.

Core, section, interval (cm)		Age	Zone	Marker event	Age (Ma)	Depth (mbsf)			
Top	Bottom					Top	Bottom	Mid-point	±
342-U1408A-	342-U1408A-								
6H-6, 60–62	6H-CC	middle Eocene	E13/E12	T *Orbulinoides beckmanni*	40.03	50.40	51.68	51.04	0.64
7H-4, 100–102	7H-5, 100–102	middle Eocene	E12/E11	B *Orbulinoides beckmanni*	40.43	57.30	58.80	58.05	0.75
9H-2, 100–102	9H-3, 100–102	middle Eocene	E11/E10	T *Guembelitrioides nuttalli*	42.07	73.30	74.80	74.05	0.75
15H-CC	16H-2, 100–102	middle Eocene	E10/E9	T *Morozovella aragonensis*	43.26	137.57	138.51	138.04	0.47
18H-6, 100–102	18H-CC	middle Eocene	E9/E8	B *Globigerinatheka kugleri*	43.88	163.33	165.78	164.56	1.22
24X-CC	25X-2, 100–102	middle Eocene	E8/E7	B *Guembelitrioides nuttalli*	45.70	215.82	220.2	218.01	2.19
27X-2, 48–49	27X-5, 97–98	late Paleocene	P4/P5	T *Globanomalina pseudomenardii*	57.10	238.88	243.87	241.38	2.50

T = top, B = base.

Table T8. Planktonic foraminifer distribution, Site U1408. This table is available in an **oversized format.**

Table T9. Abundance and preservation of benthic foraminifers, Site U1408.

Core, section, interval (cm)	Depth (mbsf)	Preservation	Group abundance
342-U1408A-			
2H-2W, 100–102	6.81	VG	P
2H-5W, 100–102	11.31	P	F
3H-2W, 100–102	16.31	P	D
3H-5W, 100–102	20.81	P	D
4H-2W, 100–102	25.81	P	D
4H-5W, 50–52	29.81	VG	P
5H-2W, 100–102	35.31	VG	P
5H-5W, 100–102	39.81	VG	R
6H-2W, 100–102	44.81	VG	P
6H-5W, 100–102	49.31	G	P
7H-2W, 100–102	54.31	VG	F
7H-5W, 100–102	58.81	VG	F
8H-2W, 100–102	63.81	G	R
8H-5W, 100–102	68.31	G	R
9H-2W, 100–102	73.31	G	P
9H-4W, 100–102	76.31	VG	R
10H-2W, 100–102	82.81	VG	P
10H-5W, 100–102	87.31	VG	P
11H-2W, 130–132	92.61	G	F
11H-5W, 100–102	96.81	VG	P
12H-2W, 100–102	100.72	VG	P
12H-5W, 100–102	105.22	G	P
13H-2W, 100–102	111.31	VG	P
13H-5W, 100–102	115.81	VG	P
14H-2W, 100–102	120.81	G	F
14H-5W, 100–102	125.31	VG	P
15H-2W, 100–102	130.31	VG	P
15H-5W, 100–102	134.81	VG	P
16H-2W, 100–102	138.52	VG	P
16H-5W, 100–102	143.01	VG	P
17H-2W, 101–103	149.32	G	F
17H-5W, 110–112	153.91	VG	P
18H-3W, 100–102	159.14	VG	P
18H-6W, 100–102	163.34	VG	P
19H-2W, 100–102	168.31	VG	P
19H-4W, 100–102	171.31	VG	R
20H-2W, 100–102	177.81	VG	P
20H-4W, 100–102	180.81	G	P
21X-2W, 100–102	185.41	VG	P
21X-4W, 100–102	188.41	VG	P
22X-2W, 100–102	191.31	VG	P
22X-4W, 100–102	194.31	VG	P
23X-2W, 100–102	201.01	VG	P
23X-4W, 100–102	204.01	G	P
24X-2W, 120–122	210.81	G	P
24X-4W, 120–122	213.81	VG	P
25X-2W, 100–102	220.21	G	P
25X-5W, 100–102	224.71	M	P
27X-2W, 48–49	238.89	G	P
27X-5W, 97–98	243.88	G	P

Preservation: VG = very good, G = good, M = moderate, P = poor. Abundance: D = dominant, F = few, R = rare, P = present. See **"Biostratigraphy"** in the "Methods" chapter (Norris et al., 2014a) for preservation and abundance definitions.

Table T10. Benthic foraminifer distribution, Site U1408. (Continued on next page.)

Core, section, interval (cm)	Depth (mbsf)	Preservation	Group abundance	*Abyssamina quadrata*	*Alabamina dissonata*	*Alabamina* sp.	*Ammodiscus cretaceus*	*Anomalina* sp.	*Anomalinoides semicribratus*	*Anomalinoides* sp.	*Aragonia aragonensis*	*Aragonia velascoensis*	*Astacolus parallelus*	*Bathysiphon* sp.	*Bolivina* sp.	*Bulbobaculites?*	*Bulimina* sp.	*Cassidulina subglobosa*	*Chilostomella* sp.	*Chrysalogonium* sp.	*Cibicidoides* aff. *laurisae*	*Cibicidoides* cf. *eocaenus*	*Cibicidoides* cf. *havanensis*	*Cibicidoides eocaenus*	*Cibicidoides grimsdalei*	*Cibicidoides havanensis*	*Cibicidoides incrassatus*	*Cibicidoides kullenbergi*	*Cibicidoides praemundulus*	*Cibicidoides* sp.	*Cibicidoides subspiratus*	*Cibicidoides wuellerstorfi*	*Dentalina* sp.	*Dorothia trochoides*	*Ehrenbergina trigona*	*Ellipsodimorphina macrocephala*	*Ellipsodimorphina* spp.	*Epistominella* sp.	*Eponides* sp.	*Fissurina* sp.	*Gaudryina pyramidata*	*Gavelinella beccariiformis*	*Gavelinella* sp.	*Guttulina* sp.	*Gyroidina* sp.	*Gyroidinoides* spp.	*Kalamopsis* (?)	*Karreriella* sp.
342-U1408A-																																																		
1H-CC	4.36	VG	P						P								P											P				F		P				P						P					
2H-CC	13.87	M	A				P		P					D	P	F	F	A									F					F												F					
3H-CC	23.37	G	P						F	F						F		A	F	P		P	P						P				F	P										F	P				
4H-CC	31.79	VG	P					P	F	F								F		A					P				P				F	P			P							F	P		F	
5H-CC	42.14	VG	P		P			F	P	P							F							F					F				F	F			P	F						P	F	P	P	
6H-CC	51.74	VG	P					F	F	F							F	P		P	F			F					F	F			F	F				P							F		F	
7H-CC	61.94	VG	P		F	P			P					F				P		F			P						F				D	P			P				P				F			
8H-CC	70.81	G	P		F			P	P	F							F				F	P		F	P				P				A				P		P					F		F	
9H-CC	78.76	VG	P					F		F				P			F	F		P				P	P								F				F		P				P			P	
10H-CC	90.18	VG	P		F				F								F			F				F	P								F	P			P	F						F		F	
11H-CC	99.27	VG	P			P		F	F	P							F	P						P					F				F	P			P		P	F			P	F			
12H-CC	108.53	G	P		F				F	F							F			F	F			F					P	F			F	A					P							F	
13H-CC	118.84	G	P	A					P						P									F			P						F	P								P						P	
14H-CC	128.20	VG	P														P			A				F									F				F							F			P	
15H-CC	137.61	VG	P					F	F	F							F	P						F									F				P							P				
16H-7, 0–18	145.09	VG	P					P		F	A						F			F	P			P					F				F											P				
17H-7, 62–75	156.00	G	P	F	P			F		F							F	F		P	F			P	F				F				F						F	F				P				
18H-CC	165.82	G	P							F	A									P				F					F				F	P			P		F	F			P	F		P	
19H-CC	175.36	G	P					F	P	F										P										P				F					P				P			P	
20H-CC	182.74	G	P					F		F	F						F			F				F					F		F		F	F			P		F						F	
21X-CC	192.73	G	P					F		F							F	P						P					P		F		F	F		F	P		F				P	F		F	
22X-CC	198.79	G	P					F		F							F	A		F	F			P					F				F				P	F	F					F		P	
23X-CC	207.77	G	P		P					F							F	F		P	F			P					P	F	F		P					F	F				P				
24X-CC	215.88	G	P		P	P		P		P	A						P	P					P	F			P			F		F	P					P								
25X-CC	227.29	M	P					P	P	F							P				F			A						F	P		F	P			P	P									
26X-CC	232.38	G	P					F	F	F		F	P		P		F							F						F			F	F			P		F	A	F		F	F			
27X-CC	246.59	G	P		P			F					F		F		P							F						F			F	P						A	F							

Preservation: VG = very good, G = good, M = moderate. Abundance: A = abundant, D = dominant, F = few, P = present. See "**Biostratigraphy**" in the "Methods" chapter (Norris et al., 2014a) for preservation and abundance definitions.

Table T10 (continued).

Core, section, interval (cm)	Depth (mbsf)	Preservation	Group abundance	*Lagena* sp.	*Lenticulina* cf. *adenalensis*	*Lenticulina* sp.	*Lenticulina whitei*	*Marssonella oxycona*	*Nodosaria aspera*	*Nodosaria* sp.	*Nonion* spp.	*Nuttallides truempyi*	*Oridorsalis* sp.	*Oridorsalis umbonatus*	*Planulina* sp.	*Pleurostomella acuta*	*Pleurostomella* sp.	*Pleurostomella tenuis*	*Polymorphina* sp.	*Praeglobobulimina* cf. *spinescens*	*Pullenia bulloides*	*Pullenia* cf. *jarvisi*	*Pullenia coryelli*	*Pullenia quinqueloba*	*Pyramidina* sp.	*Pyrgo* sp.	*Pyrulina* sp.	*Quadrimorphina* sp.	*Quinqueloculina* sp.	*Reophax* sp.	*Saracenaria* sp.	*Spiroloculina depressa*	*Spiroplectammina spectabilis*	*Stilostomella gracillima*	*Stilostomella lepidula*	*Stilostomella* sp.	*Stilostomella subspinosa*	*Strictocostella scharbergana*	*Tritaxia* sp.	*Uvigerina elongata*	*Uvigerina* sp.	*Valvulina spinosa*	Others
342-U1408A-																																											
1H-CC	4.33	VG	P			P					P	P	P	P							F			F		A		P												P		P
2H-CC	13.82	M	A	P							P	P				P		P				P		P								F	F						F		P
3H-CC	23.32	G	P	P						P	P	P		P							P	P		F						P		F		A	F	A			A	F	
4H-CC	31.75	VG	P								P	A	F	F		P		F	P		F	P		P								F	F	F	A				F	F
5H-CC	42.09	VG	P	F		P				P	P	A	P	F		F		P			F	P		P	F		P			P	P	A	F	F	F				F	
6H-CC	51.68	VG	P			P				P		A		A	A	F			P		F						F		P					P	F				P	F
7H-CC	61.89	VG	P		P	P				F		P	P	P		F		P			P			F			F						P	F	F			F		
8H-CC	70.76	G	P	F							F	A	P	F		F		F			F	P					F					F	F	P	F		P		P	P
9H-CC	78.72	VG	P			P			F	P	P	F		A		F		F			F	P		P			F						F	F	D	P				P
10H-CC	90.13	VG	P			P				P		A	P					F		P	P			F	F						P		F	F	A	P			P	F
11H-CC	99.22	VG	P	F	P					P	P	A		F		F	F	F			F			F	P							F	A	F	F	A				P
12H-CC	108.48	G	P							P		A										P											F			F	P				
13H-CC	118.81	G	P			F						A		A							F	F		A	P							P	P			F					
14H-CC	128.17	VG	P			P						A		P		P	P				A			P	P							P		F	P	P				F
15H-CC	137.57	VG	P	P		P			P		P	F	P	F		F		F			F			F	F		P	P			P	F								F
16H-7, 0–18	145.00	VG	P			F						A		A		F		F			A			F			F				F		F		P	F				P
17H-7, 62–75	155.93	G	P		P							A		F		F		F			P			P												P			P	F
18H-CC	165.78	G	P							F	P	F		F							F	P		P							P			A	F	P	F			F
19H-CC	175.27	G	P	P		P			P		P	A		A		F					P	F		F								F			F	P	F				P
20H-CC	182.52	G	P	P		F						A		F				F											F							F					F
21X-CC	192.70	G	P	F		P					F	D		A		F					F			F							P	F		F		F	A				P
22X-CC	198.76	G	P			P				P	P	F	P	A		F		P			P										P	F		P		A				P
23X-CC	207.72	G	P	F		P				P		F		A				P	P			P												P	P					P
24X-CC	215.82	G	P	P								A		A								P											F		F					F
25X-CC	227.24	M	P			F						F		F																				P					F
26X-CC	232.33	G	P				P		P			F	F					P					F	P							P					P		P	P
27X-CC	246.54	G	P				F	P	P			A	P									P	P																	P

Table T11. Core orientation data, Site U1408.

Hole U1408A		Hole U1408B		Hole U1408C	
Core	MTF (°)	Core	MTF (°)	Core	MTF(°)
342-U1408A-		342-U1408B-		342-U1408C-	
1H	100	1H	185	6H	221
2H	116	2H	296	7H	257
3H	299	3H	36	8H	349
4H	294	4H	—		
5H	103	5H	7		
6H	106				
7H	251				
8H	185				
9H	118				
10H	252				
11H	263				
12H	315				
13H	219				
14H	282				
15H	80				
16H	100				
17H	224				
18H	275				
19H	291				
20H	156				

MTF = magnetic tool face orientation from geomagnetic north. — = no tool data.

Table T12. Summary of AF demagnetization results for discrete samples, Hole U1408A. (Continued on next page.)

Core, section, interval (cm)	Depth (mbsf)	Declination 20 mT or PCA (°)	Inclination 20 mT or PCA (°)	PCA MAD (°)	PCA range (mT)	NRM 20 mT (A/m)	Measurement error (%)
342-U1408A-							
2H-3W, 75–77	8.06	184.7	–54.0			1.58E–02	3.1
2H-5W, 55–57	10.86	119.1	61.5			2.06E–03	3.9
2H-7W, 35–37	13.17	25.0	84.4			1.14E–04	5.4
3H-3W, 75–77	17.56	7.2	56.2			1.63E–04	4.8
3H-5W, 75–77	20.56	–29.9	45.1			1.25E–04	3.7
4H-2W, 75–77	25.56	–37.4	67.6			8.66E–05	6.4
4H-3W, 75–77	27.06	–60.4	85.2			6.17E–03	3.3
4H-4W, 75–77	28.56	–24.1	83.2			1.32E–04	6.1
4H-5W, 75–77	30.06	256.7	64.0			3.24E–05	11.8
4H-6W, 30–32	31.12	0.9	78.6			1.02E–03	3.5
5H-1W, 75–77	33.56	–16.4	58.7			3.60E–03	3.3
5H-3W, 75–77	36.56	18.5	55.0	6.1	20–60	6.82E–03	4.6
5H-5W, 75–77	39.56	–0.4	48.0			1.08E–02	3.9
6H-1W, 75–77	43.06	25.7	57.0			8.73E–03	4.0
6H-3W, 75–77	46.06	5.3	54.4	8.9	20–60	7.46E–03	3.7
6H-5W, 75–77	49.06	139.3	34.4			1.35E–03	3.3
6H-6W, 42–44	50.23	163.7	–26.0			7.40E–03	3.7
6H-7W, 30–32	51.11	167.3	–19.6			2.99E–03	4.0
7H-4W, 75–77	57.06	–25.6	47.8			10.00E–05	6.4
7H-5W, 75–77	58.56	–63.2	4.4			5.37E–05	9.5
7H-6W, 75–77	60.06	188.5	–23.0			5.76E–05	6.9
7H-7W, 35–37	61.16	176.2	–2.9			2.16E–04	7.9
8H-1W, 75–77	62.06	182.4	–18.6			4.42E–03	5.5
8H-3W, 70–72	65.01	180.9	–6.5	5.7	20–60	4.08E–03	5.5
8H-5W, 75–77	68.06	179.0	–5.9			4.26E–03	5.7
8H-7W, 30–32	70.23	164.7	–24.7			9.26E–03	5.6
9H-1W, 75–77	71.56	177.2	36.3			3.65E–03	3.7
9H-2W, 75–77	73.06	170.4	10.5	2.9	20–60	4.30E–03	3.2
9H-3W, 75–77	74.56	140.8	45.1			1.65E–03	3.5
9H-4W, 75–77	76.06	155.0	–8.6			2.69E–03	3.0
9H-5W, 75–77	77.56	171.5	–29.5			6.16E–03	3.8
9H-6W, 30–32	78.42	151.7	–3.2			6.17E–03	3.3
10H-1W, 75–77	81.06	143.4	17.6			4.50E–03	5.0
10H-3W, 65–67	83.96	155.2	–54.0			3.58E–04	4.5
10H-5W, 75–77	87.06	153.3	–33.7	4.4	20–60	8.78E–03	5.7
10H-7W, 27–29	89.58	138.7	21.8			3.34E–03	4.9
11H-1W, 82–84	90.63	105.8	–52.8			9.03E–05	3.7
11H-1W, 97–99	90.78	9.6	–48.0			1.47E–05	16.0
11H-2W, 74–76	92.05	–53.6	–30.1			4.09E–05	9.6
11H-3W, 74–76	93.55	177.2	–30.6			6.79E–03	6.3
11H-5W, 76–78	96.57	171.1	–17.8	8.3	30–60	1.96E–03	7.9
11H-7W, 24–26	98.86	152.1	–52.8			2.64E–03	4.7
12H-1W, 19–21	99.50	146.1	50.0			2.17E–03	4.4
12H-2W, 74–76	100.46	154.5	–39.2	6.2	30–60	2.16E–03	5.1
12H-4W, 74–76	103.46	–19.5	43.6			4.45E–03	3.2
12H-7W, 74–76	107.96	–8.6	38.8			2.49E–03	3.4
13H-2W, 74–76	111.05	–52.0	54.6			1.61E–04	7.0
13H-4W, 74–76	114.05	–10.1	41.3	4.2	10–60	1.52E–04	6.5
13H-6W, 74–76	117.05	–32.5	47.1			1.14E–04	7.7
14H-2W, 74–76	120.55	–12.4	34.1			9.45E–05	9.4
14H-4W, 74–76	123.55	17.2	45.9	2.0	10–30	1.23E–04	8.6
14H-6W, 74–76	126.55	1.6	38.1			1.07E–04	6.8
15H-2W, 74–76	130.05	2.0	42.9			1.07E–04	9.9
15H-4W, 74–76	133.05	20.7	42.3			5.09E–05	9.1
15H-6W, 66–68	135.97	10.1	38.9			6.95E–05	13.8
16H-2W, 74–76	138.26	5.3	57.0			6.07E–05	13.4
16H-3W, 74–76	139.75	142.9	3.6	23.2	10–60	3.70E–05	13.1
16H-5W, 74–76	142.75	155.5	–6.8			3.63E–05	9.8
17H-1W, 74–76	147.55	212.2	–24.0			2.83E–05	12.9
17H-3W, 76–78	150.57	235.8	6.3			1.18E–05	29.2
17H-5W, 74–76	153.55	194.3	–27.2			3.04E–05	12.8
18H-3W, 74–76	158.88	40.3	–25.9			1.31E–05	15.6
18H-5W, 70–72	161.62	162.4	–31.4			4.11E–05	10.4
19H-1W, 74–76	166.55	229.2	–21.5			6.17E–05	14.7
19H-3W, 74–76	169.55	199.2	–44.7	10.0	20–60	9.81E–05	5.1

Table T12. (continued).

Core, section, interval (cm)	Depth (mbsf)	Declination 20 mT or PCA (°)	Inclination 20 mT or PCA (°)	PCA MAD (°)	PCA range (mT)	NRM 20 mT (A/m)	Measurement error (%)
19H-5W, 74–76	172.55	256.4	–15.5			5.02E–05	16.6
20H-2W, 68–70	177.49	159.8	–33.8			1.83E–04	4.5
20H-4W, 75–77	180.56	144.4	–18.0			5.25E–05	3.8
21X-2W, 110–112	185.51	–2.0	–7.2			3.69E–05	15.4
21X-4W, 51–53	187.92	–37.8	–33.6	19.8	10–60	7.17E–05	4.8
21X-6W, 78–80	191.19	114.9	–30.3			1.28E–04	6.2
22X-2W, 72–74	191.03	195.3	–12.4			2.09E–05	18.7
22X-4W, 74–76	194.05	265.2	–25.7			7.41E–05	8.2
22X-6W, 88–90	197.21	128.5	–38.5			5.44E–05	4.6
23X-1W, 73–75	199.24	–19.5	–22.4			1.05E–04	6.0
23X-3W, 103–105	202.54	–53.1	–17.6			4.83E–05	11.7
23X-5W, 37–39	204.88	198.1	–27.2			1.15E–04	4.7
24X-1W, 49–51	208.60	113.6	–41.6			7.86E–05	4.5
24X-2W, 83–85	210.44	–37.5	–19.3			1.24E–04	8.7
24X-3W, 48–50	211.59	34.6	–25.3			6.30E–05	2.6
24X-4W, 99–101	213.60	8.6	65.0			7.42E–05	2.5
24X-5W, 76–78	214.87	149.4	83.3			2.69E–05	12.4
25X-1W, 85–87	218.56	124.5	48.5			7.78E–05	8.0
25X-3W, 84–86	221.55	–63.9	41.6			7.37E–05	9.1
25X-4W, 33–35	222.54	–43.8	47.3			7.72E–05	8.1
25X-6W, 38–40	225.59	167.7	–0.3			1.92E–05	19.8
25X-7W, 41–43	226.62	104.1	–20.2			3.93E–05	11.3
26X-1W, 11–13	227.42	–57.9	22.0			5.07E–05	12.2
26X-3W, 70–72	230.20	29.5	–19.2			1.89E–03	2.6
27X-1W, 78–80	237.69	–66.2	–33.9			4.41E–04	7.5
27X-3W, 84–86	240.75	–90.0	–57.5			2.61E–04	7.3
27X-5W, 75–77	243.66	127.2	31.7			1.39E–04	6.1

Declinations for Cores 1H through 20H are in geographic coordinates. PCA = principal component analysis, MAD = maximum angle of deviation, NRM = natural remanent magnetism.

Table T13. Magnetostratigraphic tie points, Site U1408.

Chron boundary	Age (Ma)	Hole U1408A Top Core, section, interval (cm)	Hole U1408A Top Depth (mbsf)	Hole U1408A Bottom Core, section, interval (cm)	Hole U1408A Bottom Depth (mbsf)	Hole U1408A Mid-point (mbsf)	Hole U1408B Top Core, section, interval (cm)	Hole U1408B Top Depth (mbsf)	Hole U1408B Bottom Core, section, interval (cm)	Hole U1408B Bottom Depth (mbsf)	Hole U1408B Mid-point (mbsf)
		342-U1408A-		342-U1408A-			342-U1408B-		342-U1408B-		
C17n.3n/C17r	38.333	4H-4, 140.0	29.20	4H-5, 27.5	29.58	29.39	5H-2, 22.5	30.425	5H-2, 32.5	30.53	30.48
C17r/C18n.1n	38.615	4H-5, 105.0	30.35	4H-6, 10.0	30.91	30.63	5H-2, 122.5	31.43	5H-3, 85.0	32.55	31.99
C18n.1n/C18n.1r	39.627	6H-4, 95.0	47.75	6H-5, 135.0	49.65	48.70	7H-3, 10.0	50.80	7H-4, 10.0	52.30	51.55
C18n.1r/C18n.2n	39.698	NI	NI	NI	NI	NI	7H-4, 140.0	53.60	7H-6, 22.5	55.43	54.51
C18n.2n/C18r	40.145	7H-5, 75.0	58.55	7H-6, 75.0	60.05	59.30	NI	NI	NI	NI	NI
C18r/C19n	41.154	9H-2, 122.5	73.53	9H-3, 20.0	74.00	73.77	NI	NI	NI	NI	NI
C19n/C19r	41.390	9H-3, 140.0	75.20	9H-4, 25.0	75.55	75.38	11H-1, 80.0	82.00	11H-2, 47.5	83.175	82.59
C19r/C20n	42.301	12H-2, 140.0	101.11	12H-3, 10.0	101.31	101.21	13H-5, 30.0	106.29	13H-5, 95.0	106.94	106.62
C20n/C20r	43.432	16H-2, 87.5	138.39	16H-3, 75.0	139.75	139.07	18H-3, 120.0	149.20	18H-4, 105.0	150.55	149.88
C20r/C21n	45.724	24X-3, 49.0	211.59	24X-4, 100.0	213.60	212.60	NI	NI	NI	NI	NI

Ages from Gradstein et al. (2012). NI = not identified.

Chron boundary	Age (Ma)	Hole U1408C Top Core, section, interval (cm)	Hole U1408C Top Depth (mbsf)	Hole U1408C Bottom Core, section, interval (cm)	Hole U1408C Bottom Depth (mbsf)	Hole U1408C Mid-point (mbsf)
		342-U1408C-		342-U1408C-		
C17n.3n/C17r	38.333	NI	NI	NI	NI	NI
C17r/C18n.1n	38.615	NI	NI	NI	NI	NI
C18n.1n/C18n.1r	39.627	6H-7, 50.0	49.84	7H-1, 32.5	50.13	49.98
C18n.1r/C18n.2n	39.698	7H-2, 110.0	52.40	7H-3, 85.0	53.65	53.03
C18n.2n/C18r	40.145	8H-3, 82.5	63.13	8H-3, 127.5	63.58	63.35
C18r/C19n	41.154	NI	NI	NI	NI	NI
C19n/C19r	41.390	NI	NI	NI	NI	NI
C19r/C20n	42.301	13H-1, 82.5	105.13	13H-2, 12.5	105.93	105.53
C20n/C20r	43.432	16H-7, 40.0	140.7	17H-1, 20.0	141	140.85
C20r/C21n	45.724	NI	NI	NI	NI	NI

Table T14. Summary of anisotropy of magnetic susceptibility of discrete samples, Hole U1408A. (Continued on next page.)

Core, section, interval (cm)	Depth (mbsf)	τ_3	V_3 (°)		τ_2	V_2 (°)		τ_1	V_1 (°)		Bulk susceptibility (SI)	Anisotropy (%)	*P*	L	F
			Declination	Inclination		Declination	Inclination		Declination	Inclination					
342-U1408A-															
1H-1W, 74–76	0.75	0.3303	170.5	44.5	0.3342	59.3	20.2	0.3355	312.2	38.7	4.31E–04	0.5	1.016	1.004	1.012
1H-3W, 61–63	3.62	0.3298	304.4	3.7	0.3324	211.3	40.1	0.3378	38.8	49.7	3.59E–04	0.8	1.024	1.016	1.008
2H-1W, 120–122	5.51	0.3267	26.8	86.5	0.3320	124.0	0.4	0.3414	214.0	3.5	3.52E–04	1.5	1.045	1.028	1.016
2H-3W, 75–77	8.06	0.3282	163.0	68.3	0.3352	332.5	21.4	0.3365	63.9	3.6	2.75E–04	0.8	1.025	1.004	1.021
2H-5W, 55–57	10.86	0.3314	128.2	79.8	0.3336	280.3	9.0	0.3350	11.0	4.7	2.91E–04	0.4	1.011	1.004	1.006
2H-7W, 35–37	13.17	0.3288	268.6	2.6	0.3341	4.0	64.4	0.3371	177.4	25.5	6.64E–05	0.8	1.025	1.009	1.016
3H-1W, 75–77	14.56	0.3297	295.6	69.6	0.3323	78.7	16.6	0.3380	172.2	11.6	5.59E–05	0.8	1.025	1.017	1.008
3H-3W, 75–77	17.56	0.3295	117.8	18.0	0.3318	355.2	58.8	0.3387	216.3	24.5	6.94E–05	0.9	1.028	1.021	1.007
3H-5W, 75–77	20.56	0.3311	256.4	31.9	0.3325	157.3	14.3	0.3365	46.6	54.3	7.10E–05	0.5	1.016	1.012	1.004
3H-7W, 38–40	22.69	0.3288	269.1	53.4	0.3323	2.6	2.6	0.3389	94.6	36.5	6.31E–05	1.0	1.031	1.020	1.011
4H-1W, 102–104	24.33	0.3306	83.8	13.8	0.3325	180.6	25.9	0.3369	328.4	60.2	1.19E–04	0.6	1.019	1.013	1.006
4H-3W, 75–77	27.06	0.3316	316.5	52.0	0.3325	54.6	6.3	0.3359	149.4	37.3	1.11E–04	0.4	1.013	1.010	1.003
4H-5W, 75–77	30.06	0.3215	248.8	55.6	0.3369	359.9	13.8	0.3416	98.3	30.8	5.65E–05	2.0	1.062	1.014	1.048
5H-1W, 75–77	33.56	0.3309	198.4	54.9	0.3313	67.9	24.5	0.3377	326.5	23.4	9.53E–05	0.7	1.020	1.019	1.001
5H-3W, 75–77	36.56	0.3312	350.5	59.0	0.3328	110.1	16.5	0.3360	208.2	25.5	1.14E–04	0.5	1.014	1.010	1.005
5H-5W, 75–77	39.56	0.3303	215.8	74.7	0.3340	36.1	15.3	0.3357	306.1	0.1	1.27E–04	0.5	1.016	1.005	1.011
5H-7W, 30–32	41.61	0.3306	31.1	15.6	0.3314	180.5	72.1	0.3380	298.7	8.7	1.18E–04	0.7	1.022	1.020	1.002
6H-1W, 75–77	43.06	0.3303	207.1	32.7	0.3340	58.8	52.9	0.3357	307.3	15.5	1.22E–04	0.5	1.016	1.005	1.011
6H-3W, 75–77	46.06	0.3296	302.5	24.4	0.3330	211.4	2.5	0.3374	115.8	65.5	9.42E–05	0.8	1.024	1.013	1.010
6H-5W, 75–77	49.06	0.3299	333.4	10.3	0.3344	71.6	38.1	0.3356	230.9	50.0	8.93E–05	0.6	1.017	1.003	1.014
6H-7W, 30–32	51.11	0.3310	42.2	42.4	0.3336	180.2	39.1	0.3354	289.9	22.5	1.02E–04	0.4	1.013	1.005	1.008
7H-3W, 75–77	55.56	0.3303	214.0	44.6	0.3338	37.7	45.3	0.3360	305.8	1.9	1.20E–04	0.6	1.017	1.007	1.010
7H-5W, 75–77	58.56	0.3286	270.2	74.7	0.3343	100.5	15.0	0.3371	9.8	2.6	7.09E–05	0.9	1.026	1.008	1.017
7H-7W, 35–37	61.16	0.3289	82.1	46.6	0.3312	262.3	43.4	0.3399	172.2	0.1	8.13E–05	1.1	1.033	1.026	1.007
8H-1W, 75–77	62.06	0.3314	238.1	39.8	0.3321	73.8	49.1	0.3365	334.7	7.8	1.49E–04	0.5	1.015	1.013	1.002
8H-3W, 70–72	65.01	0.3320	56.0	18.5	0.3331	317.6	23.8	0.3349	180.0	59.1	1.61E–04	0.3	1.008	1.005	1.003
8H-5W, 75–77	68.06	0.3324	143.2	48.1	0.3330	26.6	21.9	0.3346	281.1	33.7	1.67E–04	0.2	1.007	1.005	1.002
8H-7W, 30–32	70.23	0.3305	14.9	79.9	0.3339	243.8	6.7	0.3356	152.9	7.5	1.52E–04	0.5	1.015	1.005	1.010
9H-1W, 75–77	71.56	0.3310	227.4	66.3	0.3339	347.9	12.6	0.3352	82.5	19.8	1.37E–04	0.4	1.013	1.004	1.009
9H-3W, 75–77	74.56	0.3323	49.6	5.5	0.3334	141.9	22.5	0.3342	306.6	66.8	1.80E–04	0.2	1.006	1.002	1.003
9H-5W, 75–77	77.56	0.3305	45.8	74.9	0.3342	219.2	15.0	0.3353	309.7	1.7	1.37E–04	0.5	1.015	1.003	1.011
10H-1W, 75–77	81.06	0.3310	105.4	29.4	0.3338	14.8	1.0	0.3352	283.1	60.6	1.06E–04	0.4	1.013	1.004	1.009
10H-3W, 65–66	83.96	0.3261	56.3	12.1	0.3357	183.7	70.6	0.3382	323.0	14.9	5.81E–05	1.2	1.037	1.008	1.029
10H-5W, 75–77	87.06	0.3304	104.9	52.8	0.3332	261.2	34.9	0.3363	359.4	11.5	1.33E–04	0.6	1.018	1.009	1.008
10H-7W, 27–29	89.58	0.3322	47.1	24.9	0.3333	195.6	61.5	0.3345	310.9	13.1	1.24E–04	0.2	1.007	1.004	1.003
11H-1W, 82–84	90.63	0.3266	281.8	51.3	0.3341	87.2	37.8	0.3394	182.8	7.2	7.17E–05	1.3	1.039	1.016	1.023
11H-1W, 97–99	90.78	0.3201	75.4	33.7	0.3300	299.5	47.1	0.3499	182.0	23.2	1.26E–05	3.0	1.093	1.060	1.031
11H-3W, 74–76	93.55	0.3292	187.3	75.9	0.3345	66.8	7.3	0.3363	335.2	12.0	1.47E–04	0.7	1.022	1.005	1.016
11H-5W, 76–78	96.57	0.3301	239.9	71.3	0.3329	100.1	14.5	0.3370	7.1	11.5	1.36E–04	0.7	1.021	1.012	1.008
11H-7W, 24–26	98.86	0.3297	8.7	55.9	0.3330	262.0	11.0	0.3373	165.1	31.8	1.05E–04	0.8	1.023	1.013	1.010
12H-1W, 19–21	99.50	0.3298	86.0	40.3	0.3338	326.6	30.1	0.3364	212.5	35.1	1.25E–04	0.7	1.020	1.008	1.012
12H-3W, 74–76	101.96	0.3286	174.6	87.7	0.3353	84.1	0.0	0.3362	354.1	2.3	1.17E–04	0.8	1.023	1.003	1.020
12H-5W, 81–83	105.03	0.3296	52.0	73.7	0.3328	302.6	5.5	0.3376	211.1	15.3	9.04E–05	0.8	1.024	1.014	1.010
12H-7W, 74–76	107.96	0.3281	228.9	63.1	0.3329	65.3	26.0	0.3390	332.1	6.6	9.03E–05	1.1	1.033	1.018	1.015
13H-1W, 74–76	109.55	0.3309	108.0	81.4	0.3336	315.5	7.6	0.3355	225.0	3.9	9.94E–05	0.5	1.014	1.006	1.008
13H-3W, 74–76	112.55	0.3297	228.1	68.5	0.3347	18.1	18.8	0.3355	111.6	10.0	8.13E–05	0.6	1.018	1.002	1.015
13H-5W, 79–81	115.60	0.3290	65.6	72.7	0.3340	237.9	17.2	0.3371	328.6	2.2	7.24E–05	0.8	1.025	1.009	1.015
13H-7W, 30–32	118.11	0.3297	273.1	83.5	0.3338	54.0	5.1	0.3365	144.4	4.1	7.45E–05	0.7	1.021	1.008	1.013
14H-1W, 74–76	119.05	0.3283	152.5	68.5	0.3332	297.9	18.0	0.3384	31.6	11.4	8.30E–05	1.0	1.031	1.016	1.015

Table T14 (continued).

Core, section, interval (cm)	Depth (mbsf)	τ_3	V_3 (°)		τ_2	V_2 (°)		τ_1	V_1 (°)		Bulk susceptibility (SI)	Anisotropy (%)	*P*	L	F
			Declination	Inclination		Declination	Inclination		Declination	Inclination					
14H-3W, 74–76	122.05	0.3271	335.8	77.1	0.3341	101.1	7.6	0.3388	192.5	10.4	8.27E–05	1.2	1.036	1.014	1.021
14H-5W, 74–76	125.05	0.3315	319.1	14.9	0.3330	205.7	56.1	0.3355	57.9	29.6	9.20E–05	0.4	1.012	1.007	1.004
14H-7W, 25–27	127.56	0.3290	344.9	60.3	0.3347	177.9	29.1	0.3363	84.8	5.6	7.67E–05	0.7	1.022	1.005	1.017
15H-1W, 74–76	128.55	0.3289	85.5	32.1	0.3319	197.1	30.4	0.3391	320.0	42.8	6.42E–05	1.0	1.031	1.022	1.009
15H-3W, 78–80	131.59	0.3270	74.2	90.0	0.3336	292.7	0.0	0.3394	202.7	0.0	7.78E–05	1.2	1.038	1.017	1.020
15H-5W, 74–76	134.55	0.3269	225.5	80.8	0.3348	76.2	8.0	0.3383	345.5	4.7	7.51E–05	1.1	1.035	1.011	1.024
15H-7W, 24–26	137.05	0.3270	220.8	42.9	0.3320	76.0	41.3	0.3410	328.9	18.5	7.15E–05	1.4	1.043	1.027	1.015
16H-3W, 74–76	139.75	0.3293	160.4	60.2	0.3341	259.0	4.9	0.3366	351.8	29.3	9.18E–05	0.7	1.022	1.008	1.014
16H-5W, 74–78	142.75	0.3295	306.1	41.4	0.3334	102.9	46.2	0.3371	205.5	11.8	7.17E–05	0.8	1.023	1.011	1.012
16H-7W, 60–62	145.61	0.3271	299.7	54.6	0.3305	122.2	35.4	0.3423	31.3	1.2	4.35E–05	1.5	1.046	1.036	1.010
17H-1W, 74–76	147.55	0.3285	260.1	46.8	0.3323	29.0	30.6	0.3392	136.8	27.3	5.39E–05	1.1	1.033	1.021	1.012
17H-3W, 76–78	150.57	0.2987	226.1	16.7	0.3129	111.7	54.0	0.3883	326.5	30.9	3.67E–06	9.0	1.300	1.241	1.048
17H-5W, 74–76	153.55	0.3251	138.0	39.9	0.3352	344.7	46.9	0.3397	239.7	13.6	6.31E–05	1.5	1.045	1.014	1.031
17H-7W, 30–32	155.62	0.3309	208.0	16.3	0.3326	13.1	73.2	0.3365	116.8	4.1	6.91E–05	0.6	1.017	1.012	1.005
18H-1W, 48–50	156.79	0.3238	336.8	35.4	0.3371	243.3	5.0	0.3391	146.3	54.2	5.34E–05	1.5	1.047	1.006	1.041
18H-3W, 74–76	158.88	0.3286	98.6	63.0	0.3325	7.5	0.6	0.3389	277.1	27.0	6.40E–05	1.0	1.031	1.019	1.012
18H-5W, 70–72	161.62	0.3289	221.7	75.5	0.3351	73.9	12.4	0.3360	342.2	7.5	8.14E–05	0.7	1.021	1.003	1.019
19H-1W, 74–76	166.55	0.3292	323.3	78.3	0.3332	159.6	11.2	0.3375	68.9	3.2	7.64E–05	0.8	1.025	1.013	1.012
19H-3W, 74–76	169.55	0.3288	109.5	64.1	0.3340	213.0	6.4	0.3372	306.0	24.9	7.69E–05	0.8	1.026	1.010	1.016
19H-5W, 74–76	172.55	0.3306	108.7	43.5	0.3332	260.4	42.9	0.3362	4.4	14.6	8.65E–05	0.6	1.017	1.009	1.008
20H-1W, 75–77	176.06	0.3266	230.3	73.4	0.3344	328.6	2.5	0.3389	59.3	16.4	7.59E–05	1.2	1.038	1.013	1.024
20H-3W, 75–77	179.06	0.3304	219.5	39.8	0.3329	10.9	46.5	0.3368	116.9	14.7	8.67E–05	0.6	1.019	1.012	1.008
21X-1W, 75–77	183.66	0.3314	289.7	75.6	0.3336	33.6	3.5	0.3350	124.4	13.9	6.20E–05	0.4	1.011	1.004	1.006
21X-3W, 86–88	186.77	0.3298	173.3	70.1	0.3331	303.7	13.2	0.3371	37.2	14.6	6.93E–05	0.7	1.022	1.012	1.010
21X-5W, 87–89	189.78	0.3284	72.7	77.7	0.3346	285.5	10.4	0.3371	194.3	6.5	5.32E–05	0.9	1.026	1.007	1.019
21X-7W, 28–30	192.09	0.3269	96.0	9.7	0.3354	188.8	15.8	0.3377	335.7	71.4	7.04E–05	1.1	1.033	1.007	1.026
22X-1W, 72–74	189.73	0.3275	31.2	86.7	0.3355	132.0	0.6	0.3370	222.0	3.2	7.14E–05	0.9	1.029	1.004	1.024
22X-3W, 72–74	192.53	0.3290	102.9	64.5	0.3345	241.8	19.8	0.3365	337.5	15.5	8.05E–05	0.7	1.023	1.006	1.017
22X-5W, 72–74	195.53	0.3289	356.9	75.1	0.3350	170.2	14.9	0.3361	260.7	1.7	7.48E–05	0.7	1.022	1.003	1.019
22X-7W, 34–36	198.17	0.3270	248.2	79.0	0.3349	63.9	11.0	0.3381	154.0	0.8	6.75E–05	1.1	1.034	1.009	1.024
23X-1W, 73–75	199.24	0.3282	207.9	81.0	0.3352	302.1	0.7	0.3367	32.2	9.0	7.36E–05	0.8	1.026	1.004	1.021
23X-3W, 103–105	202.54	0.3281	179.8	71.0	0.3337	309.5	12.4	0.3383	42.7	14.1	7.82E–05	1.0	1.031	1.014	1.017
23X-5W, 37–39	204.88	0.3272	4.2	89.4	0.3357	231.1	0.4	0.3371	141.1	0.4	9.82E–05	1.0	1.030	1.004	1.026
24X-1W, 49–51	208.60	0.3253	119.8	73.2	0.3345	294.0	16.8	0.3402	24.5	1.6	7.59E–05	1.5	1.046	1.017	1.028
24X-3W, 48–50	211.59	0.3273	146.4	57.4	0.3331	245.8	6.0	0.3396	339.6	31.9	6.97E–05	1.2	1.037	1.020	1.018
24X-5W, 76–78	214.87	0.3275	258.6	67.4	0.3358	162.5	2.6	0.3367	71.4	22.5	8.43E–05	0.9	1.028	1.003	1.025
25X-1W, 85–87	218.56	0.3258	186.1	63.0	0.3341	89.2	3.5	0.3401	357.4	26.7	7.98E–05	1.4	1.044	1.018	1.025
25X-3W, 84–86	221.55	0.3296	357.9	57.6	0.3335	104.1	10.0	0.3369	200.1	30.4	8.04E–05	0.7	1.022	1.010	1.012
25X-5W, 35–37	224.06	0.3268	311.9	26.7	0.3331	209.0	24.0	0.3401	83.2	52.8	4.19E–05	1.3	1.041	1.021	1.019
25X-7W, 41–42	226.62	0.3112	339.1	49.7	0.3221	71.5	2.1	0.3667	163.3	40.3	3.87E–06	5.6	1.178	1.139	1.035
26X-2W, 77–78	228.77	0.3310	232.0	70.8	0.3321	34.8	18.4	0.3370	126.6	5.3	5.91E–05	0.6	1.018	1.015	1.003
26X-3W, 70–72	230.20	0.3284	89.4	76.6	0.3322	335.2	5.6	0.3394	244.0	12.1	6.37E–05	1.1	1.033	1.021	1.012
27X-1W, 78–80	237.69	0.3250	325.3	26.1	0.3339	136.0	63.6	0.3411	233.5	3.7	2.40E–05	1.6	1.050	1.022	1.027
27X-3W, 84–82	240.75	0.3245	336.0	61.7	0.3311	94.4	14.4	0.3444	190.9	23.9	2.17E–05	2.0	1.061	1.040	1.020
27X-5W, 75–77	243.66	0.3264	283.4	9.2	0.3342	165.9	70.6	0.3394	16.2	16.9	2.07E–05	1.3	1.040	1.016	1.024

τ_1, τ_2, and τ_3 are eigenvalues, and V_3, V_2, and V_1 are eigenvectors associated with minimum, intermediate, and maximum susceptibility, respectively. Measurement field = 300 A/m, sample volume = 7 cm³. *P* = ansiotropy degree, L = lineation, F = foliation.

Table T15. Biostratigraphic and magnetostratigraphic datums, Hole U1408A.

Datum tie point	Datum	Datum type	Zone/ Subzone	Age (Ma)	Depth (mbsf)		
					Top	Bottom	Mid-point
D01	Ba *Emiliania huxleyi*	Calcareous nannofossil	NN21	0.29	0.75	2.25	1.50
	T *Pseudoemiliania lacunosa*	Calcareous nannofossil	NN20	0.44	4.33	8.30	6.32
	T *Discoaster brouweri*	Calcareous nannofossil	NN19	1.93	8.30	9.80	9.05
D02	T *Discoaster hamatus*	Calcareous nannofossil	NN10	9.53	9.80	11.30	10.55
	T *Catinaster coalitus*	Calcareous nannofossil		9.69	9.80	11.30	10.55
	B *Discoaster hamatus*	Calcareous nannofossil		10.55	11.30	13.87	12.59
D03	B *Catinaster calyculus*	Calcareous nannofossil		10.79	11.30	13.87	12.59
D04	B *Sphenolithus distentus*	Calcareous nannofossil		30.00	27.31	28.81	28.06
	T *Reticulofenestra umbilicus* (>14 µm)	Calcareous nannofossil	NP23	32.02	27.31	28.81	28.06
	T *Coccolithus formosus*	Calcareous nannofossil	NP22	32.92	27.31	28.81	28.06
D05	T *Chiasmolithus grandis*	Calcareous nannofossil		37.98	28.81	28.81	28.81
	B *Dictyococcites bisectus* (>10 µm)	Calcareous nannofossil		40.36	63.81	65.31	64.56
	T *Chiasmolithus solitus*	Calcareous nannofossil	NP17	40.40	60.31	61.94	61.13
	B *Reticulofenestra reticulata*	Calcareous nannofossil		41.66	98.22	99.27	98.75
	T *Nannotetrina* spp.	Calcareous nannofossil		41.85	108.53	118.84	113.69
	B *Reticulofenestra umbilicus* (>14 µm)	Calcareous nannofossil		41.94	128.20	130.31	129.25
	T *Nannotetrina fulgens*	Calcareous nannofossil		42.87	130.31	137.61	133.96
	T *Chiasmolithus gigas*	Calcareous nannofossil	NP15c	44.12	150.55	153.92	152.24
	B *Sphenolithus furcatolithoides*	Calcareous nannofossil			182.74	192.73	187.73
	B *Chiasmolithus gigas*	Calcareous nannofossil	NP15b	45.49	199.49	202.25	200.87
D15	B *Nannotetrina fulgens*	Calcareous nannofossil	NP15a	46.29	223.21	224.70	223.96
	B *Nannotetrina cristata*	Calcareous nannofossil		47.73	223.21	224.70	223.96
	T *Discoaster lodoensis*	Calcareous nannofossil		47.41	223.21	224.70	223.96
	B *Discoaster sublodoensis* (5 rayed)	Calcareous nannofossil	NP14	49.11	224.70	226.00	225.35
	B *Dictyococcites/Reticulofenestra*	Calcareous nannofossil		50.50	223.21	224.70	223.96
D17	T *Tribrachiatus orthostylus*	Calcareous nannofossil	NP13	50.50	224.70	226.00	225.35
D18	T *Toweius* spp.	Calcareous nannofossil		50.78	224.70	226.00	225.35
D19	B *Discoaster lodoensis*	Calcareous nannofossil	NP12	53.70	227.64	228.12	227.88
	T *Tribrachiatus contortus*	Calcareous nannofossil	NP11	54.17			
	B *Sphenolithus radians*	Calcareous nannofossil		54.17			
	B *Tribrachiatus orthostylus*	Calcareous nannofossil		54.37	228.12	228.34	228.23
	B *Discoaster diastypus*	Calcareous nannofossil		54.95	228.85	229.27	229.06
	T *Fasciculithus* spp.	Calcareous nannofossil		55.64	229.36	229.44	229.40
	B *Rhomboaster bramlettei*	Calcareous nannofossil	NP10	55.86	229.44	229.49	229.47
	Fasciculithus diversity decline	Calcareous nannofossil		56.00	229.93	229.93	229.93
D20	T *Fasciculithus alanii*	Calcareous nannofossil		56.00	229.65	229.93	229.79
	T *Ericsonia robusta* (>9 µm)	Calcareous nannofossil		57.10	232.38	243.88	238.13
D21	B *Discoaster multiradiatus*	Calcareous nannofossil	NP9	57.21	243.88	245.19	244.54
	Tc *Sphenolithus anarrhopus*	Calcareous nannofossil			243.88	246.59	245.23
	B *Discoaster delicatus*	Calcareous nannofossil		57.45	245.19	246.59	245.89
	B *Ericsonia robusta* (>9 µm)	Calcareous nannofossil		57.54	245.19	246.59	245.89
	Tc *Discoaster backmanii*	Calcareous nannofossil		57.57	243.88	245.19	244.53
	B *Discoaster backmanii*	Calcareous nannofossil		58.28	246.59	246.59	246.59
D22	B *Discoaster mohleri*	Calcareous nannofossil	NP7	58.97	246.59	246.59	246.59
	T *Calocyclas trichopa*	Radiolarian		43.38	144.29		144.29
	T *Podocyrtis dorus*	Radiolarian	RP13	43.81	145.09	150.50	147.80
	B *Calocyclas trichopa*	Radiolarian		44.46	150.50		150.50
	T *Amphisphaera goruna*	Radiolarian		55.50	227.85	231.85	229.85
	X *Bekoma campechensis - B. bidartensis*	Radiolarian	RP7	58.23	246.59		246.59
	T *Orbulinoies beckmani*	Planktonic foraminifer	E13/E12	40.03	50.40	51.68	51.04
	B *Orbulinoies beckmani*	Planktonic foraminifer	E12/E11	40.43	57.30	58.80	58.05
	T *Guembelitrioides nuttalli*	Planktonic foraminifer	E11/E10	42.07	73.30	74.80	74.05
	T *Morozovella aragonensis*	Planktonic foraminifer	E10/E9	43.26	137.57	138.51	138.04
	B *Globigerinatheka kugleri*	Planktonic foraminifer	E9/E8	43.88	163.33	165.78	164.56
	B *Guembelitrioides nuttalli*	Planktonic foraminifer	E8/E7	45.72	215.82	220.20	218.01
	T *Globanomalina pseudomenardii*	Planktonic foraminifer	P4/P5	57.10	238.88	243.87	241.38
D6	C17n.3n/C17r	Chron boundary		38.33			29.39
D7	C17r/C18n.1n	Chron boundary		38.62			30.63
D8	C18n.1n/C18n.1r	Chron boundary		39.63			48.70
D9	C18n.2n/C18r	Chron boundary		40.14			59.30
D10	C18r/C19n	Chron boundary		41.15			73.77
D11	C19n/C19r	Chron boundary		41.39			75.38
D12	C19r/C20n	Chron boundary		42.30			101.21
D13	C20n/C20r	Chron boundary		43.43			139.07
D14	C20r/C21n	Chron boundary		45.72			212.60

T = top, Tc = top common, B = base, Ba = base of acme, X = faunal crossover.

Table T16. Datum tie points, Hole U1408A.

Datum tie point	Datum	Datum type	Zone/ Subzone	Age (Ma)	Mid-point depth (mbsf)	Distance (m)	Duration (Ma)	LSR (cm/k.y.)	Notes
D01	Ba *Emiliania huxleyi*	Calcareous nannofossil	NN21	0.29	1.50				
D02	T *Discoaster hamatus*	Calcareous nannofossil	Nn10	9.53	10.55	9.05	9.24	0.10	Average rate = 0.09 cm/k.y.
D03	B *Catinaster calyculus*	Calcareous nannofossil		10.79	12.59	2.04	1.26	0.16	
D04	B *Sphenolithus distentus*	Calcareous nannofossil		30.00	28.06	15.48	19.21	0.08	
D05	T *Chiasmolithus grandis*	Calcareous nannofossil		37.98	28.81	0.00	7.98	0.00	Hiatus
D06	C17n.3n/C17r	Chron boundary		38.33	29.39	1.33	0.35	0.38	
D07	C17r/C18n.1n	Chron boundary		38.62	30.63	1.24	0.28	0.44	
D08	C18n.1n/C18n.1r	Chron boundary		39.63	48.70	18.07	1.01	1.79	Average rate = 1.39 cm/k.y.
D09	C18n.2n/C18r	Chron boundary		40.14	59.30	10.60	0.52	2.05	
D10	C18r/C19n	Chron boundary		41.15	73.77	14.47	1.01	1.43	
D11	C19n/C19r	Chron boundary		41.39	75.38	1.61	0.24	0.68	
D12	C19r/C20n	Chron boundary		42.30	101.21	25.84	0.91	2.83	
D13	C20n/C20r	Chron boundary		43.43	139.07	37.86	1.13	3.35	Average rate = 3.03 cm/k.y.
D14	C20r/C21n	Chron boundary		45.72	212.60	74.16	2.29	3.24	
D15	B *Nannotetrina fulgens*	Calcareous nannofossil	NP15a	46.29	223.96	10.73	0.57	1.89	
D17	*T Tribrachiatus orthostylus*	Calcareous nannofossil	NP13	50.50	225.35	1.40	4.21	0.03	Hiatus
D18	T *Toweius* spp.	Calcareous nannofossil	NP12	50.78	225.35	0.00	0.28	0.00	
D19	B *Discoaster lodoensis*	Calcareous nannofossil		53.70	227.88	2.53	2.92	0.09	Condensed
D20	T *Fasciculithus alanii*	Calcareous nannofossil		56.00	229.79	1.91	2.30	0.08	
D21	B *Discoaster multiradiatus*	Calcareous nannofossil	NP9	57.21	245.23	15.44	1.21	1.27	Average rate = 1.27 cm/k.y.
D22	B *Discoaster mohleri*	Calcareous nannofossil	NP7	58.97	246.59	1.36	1.76	0.08	Condensed

LSR = linear sedimentation rate. T = top, B = base, Ba = base of acme.

Table T17. Carbonate content and accumulation rates, Site U1408. (Continued on next four pages.)

Age (Ma)	LSR (cm/k.y.)	Dry density (g/cm^3)	$CaCO_3$ (wt%)	MAR (g/cm^2/k.y.)	CAR (g/cm^2/k.y.)	nCAR (g/cm^2/k.y.)
0.8	0.09	0.67	43.45	0.06	0.03	0.03
1.0	0.09	0.70	43.14	0.06	0.03	0.04
1.2	0.09	0.73	42.84	0.07	0.03	0.04
1.4	0.09	0.76	42.54	0.07	0.03	0.04
1.6	0.09	0.79	42.23	0.07	0.03	0.04
1.8	0.09	0.82	41.93	0.07	0.03	0.04
2.0	0.09	0.85	41.62	0.08	0.03	0.04
2.2	0.09	0.88	41.32	0.08	0.03	0.05
2.4	0.09	0.92	41.03	0.08	0.03	0.05
2.6	0.09	0.98	40.75	0.09	0.04	0.05
2.8	0.09	1.03	40.48	0.09	0.04	0.05
3.0	0.09	1.09	40.21	0.10	0.04	0.06
3.2	0.09	1.15	39.93	0.10	0.04	0.06
3.4	0.09	1.20	39.66	0.11	0.04	0.06
3.6	0.09	1.26	39.38	0.11	0.04	0.07
3.8	0.09	1.31	39.11	0.12	0.05	0.07
4.0	0.09	1.37	38.84	0.12	0.05	0.07
4.2	0.09	1.43	38.56	0.13	0.05	0.08
4.4	0.09	1.48	38.29	0.13	0.05	0.08
4.6	0.09	1.46	36.44	0.13	0.05	0.08
4.8	0.09	1.32	32.79	0.12	0.04	0.08
5.0	0.09	1.18	29.13	0.11	0.03	0.07
5.2	0.09	1.04	25.47	0.09	0.02	0.07
5.4	0.09	0.91	21.81	0.08	0.02	0.06
5.6	0.09	0.81	19.70	0.07	0.01	0.06
5.8	0.09	0.81	20.05	0.07	0.01	0.06
6.0	0.09	0.81	20.43	0.07	0.01	0.06
6.2	0.09	0.81	20.81	0.07	0.02	0.06
6.4	0.09	0.81	21.19	0.07	0.02	0.06
6.6	0.09	0.81	21.57	0.07	0.02	0.06
6.8	0.09	0.81	21.95	0.07	0.02	0.06
7.0	0.09	0.81	22.33	0.07	0.02	0.06
7.2	0.09	0.81	22.81	0.07	0.02	0.06
7.4	0.09	0.84	23.88	0.07	0.02	0.06
7.6	0.09	0.87	25.05	0.08	0.02	0.06
7.8	0.09	0.90	26.22	0.08	0.02	0.06
8.0	0.09	0.93	27.39	0.08	0.02	0.06
8.2	0.09	0.96	28.57	0.09	0.02	0.06
8.4	0.09	0.99	29.74	0.09	0.03	0.06
8.6	0.09	1.03	30.91	0.09	0.03	0.06
8.8	0.09	1.06	32.06	0.09	0.03	0.06
9.0	0.09	1.07	30.53	0.10	0.03	0.07
9.2	0.09	1.06	27.13	0.09	0.03	0.07
9.4	0.09	1.05	23.72	0.09	0.02	0.07
9.6	0.09	1.04	20.32	0.09	0.02	0.07
9.8	0.09	1.03	16.92	0.09	0.02	0.08
10.0	0.09	1.03	13.52	0.09	0.01	0.08
10.2	0.09	1.02	10.11	0.09	0.01	0.08
10.4	0.09	1.01	6.84	0.09	0.01	0.08
10.6	0.09	1.00	6.15	0.09	0.01	0.08
10.8	0.09	1.00	6.46	0.09	0.01	0.08
11.0	0.09	0.99	6.78	0.09	0.01	0.08
11.2	0.09	0.98	7.09	0.09	0.01	0.08
11.4	0.09	0.98	7.41	0.09	0.01	0.08
11.6	0.09	0.97	7.72	0.09	0.01	0.08
11.8	0.09	0.97	8.03	0.09	0.01	0.08
12.0	0.09	0.95	8.10	0.08	0.01	0.08
12.2	0.09	0.89	6.95	0.08	0.01	0.07
12.4	0.09	0.82	5.62	0.07	0.00	0.07
12.6	0.09	0.75	4.30	0.07	0.00	0.06
12.8	0.09	0.69	2.97	0.06	0.00	0.06
13.0	0.09	0.62	1.65	0.06	0.00	0.05
13.2	0.09	0.57	1.02	0.05	0.00	0.05
13.4	0.09	0.57	2.20	0.05	0.00	0.05
13.6	0.09	0.57	3.48	0.05	0.00	0.05
13.8	0.09	0.57	4.75	0.05	0.00	0.05
14.0	0.09	0.57	6.03	0.05	0.00	0.05
14.2	0.09	0.57	7.30	0.05	0.00	0.05
14.4	0.09	0.57	8.56	0.05	0.00	0.05

Table T17. (continued). (Continued on next page.)

Age (Ma)	LSR (cm/k.y.)	Dry density (g/cm^3)	$CaCO_3$ (wt%)	MAR (g/cm^2/k.y.)	CAR (g/cm^2/k.y.)	nCAR (g/cm^2/k.y.)
14.6	0.09	0.61	8.94	0.05	0.00	0.05
14.8	0.09	0.69	8.76	0.06	0.01	0.06
15.0	0.09	0.76	8.58	0.07	0.01	0.06
15.2	0.09	0.83	8.41	0.07	0.01	0.07
15.4	0.09	0.90	8.23	0.08	0.01	0.07
15.6	0.09	0.97	8.05	0.09	0.01	0.08
15.8	0.09	1.04	7.87	0.09	0.01	0.09
16.0	0.09	1.11	7.70	0.10	0.01	0.09
16.2	0.09	1.16	7.62	0.10	0.01	0.10
16.4	0.09	1.11	7.80	0.10	0.01	0.09
16.6	0.09	1.06	7.99	0.09	0.01	0.09
16.8	0.09	1.00	8.17	0.09	0.01	0.08
17.0	0.09	0.95	8.36	0.09	0.01	0.08
17.2	0.09	0.90	8.55	0.08	0.01	0.07
17.4	0.09	0.85	8.74	0.08	0.01	0.07
17.6	0.09	0.79	8.93	0.07	0.01	0.06
17.8	0.09	0.74	9.04	0.07	0.01	0.06
18.0	0.09	0.72	8.28	0.06	0.01	0.06
18.2	0.09	0.72	7.26	0.06	0.00	0.06
18.4	0.09	0.71	6.25	0.06	0.00	0.06
18.6	0.09	0.70	5.24	0.06	0.00	0.06
18.8	0.09	0.70	4.22	0.06	0.00	0.06
19.0	0.09	0.69	3.21	0.06	0.00	0.06
19.2	0.09	0.68	2.19	0.06	0.00	0.06
19.4	0.09	0.68	1.18	0.06	0.00	0.06
19.6	0.09	0.68	1.19	0.06	0.00	0.06
19.8	0.09	0.69	2.38	0.06	0.00	0.06
20.0	0.09	0.70	3.58	0.06	0.00	0.06
20.2	0.09	0.72	4.77	0.06	0.00	0.06
20.4	0.09	0.73	5.97	0.07	0.00	0.06
20.6	0.09	0.74	7.16	0.07	0.00	0.06
20.8	0.09	0.75	8.36	0.07	0.01	0.06
21.0	0.09	0.77	9.55	0.07	0.01	0.06
21.2	0.09	0.77	10.62	0.07	0.01	0.06
21.4	0.09	0.76	11.09	0.07	0.01	0.06
21.6	0.09	0.75	11.49	0.07	0.01	0.06
21.8	0.09	0.73	11.88	0.07	0.01	0.06
22.0	0.09	0.71	12.28	0.06	0.01	0.06
22.2	0.09	0.70	12.67	0.06	0.01	0.05
22.4	0.09	0.68	13.07	0.06	0.01	0.05
22.6	0.09	0.67	13.47	0.06	0.01	0.05
22.8	0.09	0.66	13.61	0.06	0.01	0.05
23.0	0.09	0.69	13.23	0.06	0.01	0.05
23.2	0.09	0.72	12.84	0.06	0.01	0.06
23.4	0.09	0.75	12.44	0.07	0.01	0.06
23.6	0.09	0.77	12.04	0.07	0.01	0.06
23.8	0.09	0.80	11.83	0.07	0.01	0.06
24.0	0.09	0.80	12.23	0.07	0.01	0.06
24.2	0.09	0.80	12.68	0.07	0.01	0.06
24.4	0.09	0.80	13.14	0.07	0.01	0.06
24.6	0.09	0.80	13.59	0.07	0.01	0.06
24.8	0.09	0.81	14.04	0.07	0.01	0.06
25.0	0.09	0.81	14.50	0.07	0.01	0.06
25.2	0.09	0.81	14.95	0.07	0.01	0.06
25.4	0.09	0.81	15.41	0.07	0.01	0.06
25.6	0.09	0.81	15.90	0.07	0.01	0.06
25.8	0.09	0.81	16.62	0.07	0.01	0.06
26.0	0.09	0.81	17.37	0.07	0.01	0.06
26.2	0.09	0.81	18.12	0.07	0.01	0.06
26.4	0.09	0.81	18.87	0.07	0.01	0.06
26.6	0.09	0.80	19.62	0.07	0.01	0.06
26.8	0.09	0.80	20.18	0.07	0.01	0.06
27.0	0.09	0.80	19.98	0.07	0.01	0.06
27.2	0.09	0.80	19.69	0.07	0.01	0.06
27.4	0.09	0.79	19.41	0.07	0.01	0.06
27.6	0.09	0.79	19.13	0.07	0.01	0.06
27.8	0.09	0.79	18.85	0.07	0.01	0.06
28.0	0.09	0.78	18.57	0.07	0.01	0.06
28.2	0.09	0.78	18.29	0.07	0.01	0.06
28.4	0.09	0.78	18.02	0.07	0.01	0.06

Table T17. (continued). (Continued on next page.)

Age (Ma)	LSR (cm/k.y.)	Dry density (g/cm^3)	$CaCO_3$ (wt%)	MAR (g/cm^2/k.y.)	CAR (g/cm^2/k.y.)	nCAR (g/cm^2/k.y.)
28.6	0.09	0.79	18.17	0.07	0.01	0.06
28.8	0.09	0.80	18.51	0.07	0.01	0.06
29.0	0.09	0.81	18.86	0.07	0.01	0.06
29.2	0.09	0.83	19.20	0.07	0.01	0.06
29.4	0.09	0.84	19.55	0.08	0.01	0.06
29.6	0.09	0.86	19.89	0.08	0.02	0.06
29.8	0.09	0.87	20.23	0.08	0.02	0.06
30.0	0.02	0.88	20.58	0.01	0.00	0.01
30.2	0.02	0.90	20.92	0.01	0.00	0.01
30.4	0.02	0.91	21.26	0.01	0.00	0.01
30.6	0.02	0.92	21.61	0.01	0.00	0.01
30.8	0.02	0.94	21.92	0.01	0.00	0.01
31.0	0.02	0.94	22.14	0.01	0.00	0.01
31.2	0.02	0.93	22.35	0.01	0.00	0.01
31.4	0.02	0.93	22.57	0.01	0.00	0.01
31.6	0.02	0.93	22.79	0.01	0.00	0.01
31.8	0.02	0.92	23.00	0.01	0.00	0.01
32.0	0.02	0.92	23.22	0.01	0.00	0.01
32.2	0.02	0.92	23.43	0.01	0.00	0.01
32.4	0.02	0.92	23.65	0.01	0.00	0.01
32.6	0.02	0.91	23.87	0.01	0.00	0.01
32.8	0.02	0.91	24.08	0.01	0.00	0.01
33.0	0.02	0.91	24.30	0.01	0.00	0.01
33.2	0.02	0.91	24.51	0.01	0.00	0.01
33.4	0.02	0.90	24.73	0.01	0.00	0.01
33.6	0.02	0.90	24.95	0.01	0.00	0.01
33.8	0.02	0.90	25.16	0.01	0.00	0.01
34.0	0.02	0.89	25.38	0.01	0.00	0.01
34.2	0.02	0.89	25.59	0.01	0.00	0.01
34.4	0.02	0.89	25.81	0.01	0.00	0.01
34.6	0.02	0.89	26.03	0.01	0.00	0.01
34.8	0.02	0.88	26.24	0.01	0.00	0.01
35.0	0.02	0.88	26.46	0.01	0.00	0.01
35.2	0.02	0.88	26.67	0.01	0.00	0.01
35.4	0.02	0.88	26.89	0.01	0.00	0.01
35.6	0.02	0.87	27.11	0.01	0.00	0.01
35.8	0.02	0.87	27.32	0.01	0.00	0.01
36.0	0.02	0.87	27.54	0.01	0.00	0.01
36.2	0.02	0.86	27.75	0.01	0.00	0.01
36.4	0.02	0.86	27.97	0.01	0.00	0.01
36.6	0.02	0.86	28.19	0.01	0.00	0.01
36.8	0.02	0.86	28.40	0.01	0.00	0.01
37.0	0.02	0.85	28.62	0.01	0.00	0.01
37.2	0.02	0.85	28.83	0.01	0.00	0.01
37.4	0.02	0.85	29.05	0.01	0.00	0.01
37.6	0.02	0.85	29.27	0.01	0.00	0.01
37.8	0.02	0.84	29.48	0.01	0.00	0.01
38.0	0.02	0.84	29.70	0.01	0.00	0.01
38.2	0.02	0.84	29.91	0.01	0.00	0.01
38.4	0.44	0.84	30.95	0.37	0.11	0.25
38.6	0.44	0.86	36.34	0.38	0.14	0.24
38.8	1.79	0.87	35.43	1.56	0.55	1.01
39.0	1.79	0.91	47.36	1.63	0.77	0.86
39.2	1.79	0.89	35.09	1.59	0.56	1.03
39.4	1.79	0.87	35.90	1.55	0.55	0.99
39.6	1.79	0.91	43.95	1.62	0.71	0.91
39.8	2.05	0.92	44.85	1.88	0.84	1.04
40.0	2.05	0.92	44.63	1.88	0.84	1.04
40.2	1.43	0.93	34.35	1.33	0.46	0.88
40.4	1.43	0.92	34.50	1.32	0.46	0.87
40.6	1.43	0.96	32.22	1.37	0.44	0.93
40.8	1.43	1.00	32.43	1.43	0.47	0.97
41.0	1.43	1.01	37.05	1.45	0.54	0.91
41.2	0.68	1.05	36.27	0.72	0.26	0.46
41.4	2.83	1.05	34.36	2.98	1.02	1.95
41.6	2.83	0.99	41.26	2.80	1.15	1.64
41.8	2.83	1.01	44.63	2.87	1.28	1.59
42.0	2.83	1.00	66.92	2.83	1.90	0.94
42.2	2.83	1.06	51.12	3.00	1.53	1.47
42.4	3.35	1.06	38.66	3.54	1.37	2.17

Table T17. (continued). (Continued on next page.)

Age (Ma)	LSR (cm/k.y.)	Dry density (g/cm^3)	$CaCO_3$ (wt%)	MAR (g/cm^2/k.y.)	CAR (g/cm^2/k.y.)	nCAR (g/cm^2/k.y.)
42.6	3.35	1.01	37.38	3.38	1.26	2.12
42.8	3.35	0.98	39.16	3.29	1.29	2.00
43.0	3.35	1.01	37.73	3.37	1.27	2.10
43.2	3.35	1.00	36.02	3.37	1.21	2.15
43.4	3.35	1.00	45.94	3.33	1.53	1.80
43.6	3.21	0.97	41.12	3.10	1.27	1.82
43.8	3.21	0.99	51.31	3.18	1.63	1.55
44.0	3.21	1.03	44.56	3.31	1.48	1.84
44.2	3.21	1.13	47.67	3.62	1.73	1.89
44.4	3.21	1.20	44.32	3.86	1.71	2.15
44.6	3.21	1.22	44.74	3.91	1.75	2.16
44.8	3.21	1.22	42.57	3.91	1.67	2.25
45.0	3.21	1.22	45.63	3.92	1.79	2.13
45.2	3.21	1.25	42.41	4.00	1.70	2.30
45.4	3.21	1.22	42.92	3.92	1.68	2.24
45.6	3.21	1.21	42.86	3.89	1.67	2.22
45.8	3.21	1.24	39.78	3.97	1.58	2.39
46.0	3.21	1.21	38.17	3.88	1.48	2.40
46.2	3.21	1.34	48.95	4.29	2.10	2.19
46.4	0.00	1.39	66.73	0.00	0.00	0.00
46.6	0.00	1.39	67.81	0.00	0.00	0.00
46.8	0.00	1.39	68.89	0.00	0.00	0.00
47.0	0.00	1.39	69.96	0.00	0.00	0.00
47.2	0.00	1.39	71.04	0.00	0.00	0.00
47.4	0.00	1.38	72.12	0.00	0.00	0.00
47.6	0.00	1.38	73.20	0.00	0.00	0.00
47.8	0.00	1.38	74.28	0.00	0.00	0.00
48.0	0.00	1.38	75.35	0.00	0.00	0.00
48.2	0.00	1.38	76.43	0.00	0.00	0.00
48.4	0.00	1.38	77.51	0.00	0.00	0.00
48.6	0.00	1.37	78.59	0.00	0.00	0.00
48.8	0.00	1.37	79.67	0.00	0.00	0.00
49.0	0.00	1.37	80.74	0.00	0.00	0.00
49.2	0.00	1.37	81.82	0.00	0.00	0.00
49.4	0.00	1.37	82.90	0.00	0.00	0.00
49.6	0.00	1.37	83.98	0.00	0.00	0.00
49.8	0.00	1.36	85.06	0.00	0.00	0.00
50.0	0.00	1.36	86.13	0.00	0.00	0.00
50.2	0.00	1.36	87.21	0.00	0.00	0.00
50.4	0.00	1.36	88.29	0.00	0.00	0.00
50.6	0.00	1.36	89.37	0.00	0.00	0.00
50.8	0.09	1.35	90.44	0.12	0.11	0.01
51.0	0.09	1.36	90.78	0.12	0.11	0.01
51.2	0.09	1.37	90.48	0.12	0.11	0.01
51.4	0.09	1.38	90.17	0.12	0.11	0.01
51.6	0.09	1.39	89.87	0.12	0.11	0.01
51.8	0.09	1.41	89.56	0.12	0.11	0.01
52.0	0.09	1.42	89.29	0.12	0.11	0.01
52.2	0.09	1.41	89.34	0.12	0.11	0.01
52.4	0.09	1.40	89.48	0.12	0.11	0.01
52.6	0.09	1.39	89.62	0.12	0.11	0.01
52.8	0.09	1.38	89.76	0.12	0.11	0.01
53.0	0.09	1.37	89.86	0.12	0.11	0.01
53.2	0.09	1.38	88.32	0.12	0.11	0.01
53.4	0.09	1.39	85.91	0.12	0.10	0.02
53.6	0.09	1.41	83.50	0.12	0.10	0.02
53.8	0.08	1.42	81.09	0.12	0.10	0.02
54.0	0.08	1.43	78.68	0.12	0.09	0.03
54.2	0.08	1.45	76.27	0.12	0.09	0.03
54.4	0.08	1.46	73.87	0.12	0.09	0.03
54.6	0.08	1.45	71.56	0.12	0.09	0.03
54.8	0.08	1.43	69.29	0.12	0.08	0.04
55.0	0.08	1.41	67.01	0.12	0.08	0.04
55.2	0.08	1.39	64.73	0.12	0.07	0.04
55.4	0.08	1.37	62.45	0.11	0.07	0.04
55.6	0.08	1.35	60.18	0.11	0.07	0.04
55.8	0.08	1.33	57.90	0.11	0.06	0.05
56.0	1.27	1.31	60.41	1.67	1.01	0.66
56.2	1.27	1.31	84.43	1.67	1.41	0.26
56.4	1.27	1.29	83.17	1.64	1.37	0.28

Table T17. (continued).

Age (Ma)	LSR (cm/k.y.)	Dry density (g/cm^3)	$CaCO_3$ (wt%)	MAR (g/cm^2/k.y.)	CAR (g/cm^2/k.y.)	nCAR (g/cm^2/k.y.)
56.6	1.27	1.25	81.29	1.60	1.30	0.30
56.8	1.27	1.21	81.37	1.54	1.25	0.29
57.0	1.27	1.19	75.92	1.51	1.15	0.36
57.2	1.27	1.08	67.91	1.37	0.93	0.44
57.4	0.08	1.05	68.47	0.08	0.06	0.03
57.6	0.08	1.03	69.86	0.08	0.06	0.02
57.8	0.08	1.01	71.25	0.08	0.06	0.02
58.0	0.08	0.99				

LSR = linear sedimentation rate, MAR = mass accumulation rate, CAR = carbonate accumulation rate, nCAR = noncarbonate accumulation rate.

Table T18. Geochemistry of headspace gas samples, Hole U1408A.

Core, section, interval (cm)	Depth (mbsf)	Methane (ppmv)
342-U1408-		
1H-3, 0–5	3.00	1.84
2H-7, 0–5	12.81	1.81
3H-7, 0–5	22.30	1.97
4H-6, 0–5	30.81	1.88
5H-7, 0–5	41.30	2.6
6H-7, 0–5	50.80	2.36
7H-7, 0–5	60.80	2.5
8H-7, 0–5	69.92	4.4
9H-6, 0–5	78.11	2.73
10H-7, 0–5	89.30	2.78
11H-7, 0–5	98.61	2.43
12H-7, 0–5	107.21	2.79
13H-7, 0–5	117.80	3.29
14H-7, 0–5	127.30	4.46
15H-7, 0–5	136.80	4.79
16H-7, 0–5	145.00	3.89
17H-7, 0–5	155.31	4.33
18H-7, 0–5	163.76	3.5
19H-7, 0–5	174.70	4.31
20H-5, 0–5	181.30	3.08
21X-7, 0–5	191.80	3.51
22X-7, 0–5	197.82	3.28
23X-6, 0–5	206.00	3.08
24X-5, 0–5	214.10	2.7
25X-7, 0–5	226.20	2.71
26X-4, 0–5	230.99	2.16
27X-7, 0–5	245.71	2.27

Table T19. Interstitial water constituents, Hole U1408A.

Core, section, interval (cm)	Depth (mbsf)	pH	Alkalinity (mM)	NH_4 (μM)	Salinity	Cl^- (mM)	Na^+ (mM)	SO_4^{2-} (mM)	HPO_4^- (μM)	Mn^{2+} (μM)	Fe^{2+} (μM)	Ca^{2+} (mM)	Mg^{2+} (mM)	B (μM)	K^+ (mM)	Mg/Ca
342-U1408A-																
1H-2, 145–150	2.95	7.45	3.279	10	37	551.037	473.517	28.902	BDL	28.20	ND	11.38	54.01	393.30	13.64	4.7
2H-6, 96–101	12.76	7.45	3.26	6	38	544.879	467.342	28.202	BDL	13.88	ND	11.56	53.17	395.79	14.04	4.6
3H-6, 95–100	22.25	7.27	3.177	40	38	543.185	461.96	27.454	BDL	7.11	ND	11.66	51.99	473.04	13.85	4.5
4H-5, 146–151	30.76	7.35	3.146	23	38	544.48	474.209	27.737	BDL	4.24	13.98	12.04	52.70	472.27	14.02	4.4
5H-6, 95–100	41.25	7.42	3.086	6	38	547.803	468.683	26.48	BDL	2.80	6.35	12.37	51.99	456.66	12.01	4.2
6H-6, 95–100	50.75	7.00	3.187	3	38	560.656	482.903	27.608	BDL	3.90	42.78	12.94	52.76	475.32	14.55	4.1
7H-6, 145–150	60.75	7.23	3.504	12	37	533.657	457.912	26.135	BDL	4.63	32.85	13.09	50.42	464.48	12.80	3.9
8H-6, 107-112	69.87	7.24	3.893	8	37	542.211	468.032	26.524	BDL	5.72	30.28	13.90	51.39	489.58	11.32	3.7
9H-5, 126–131	78.06	7.08	3.851	16	37	546.905	469.973	26.492	BDL	5.90	33.19	14.32	50.51	453.21	13.27	3.5
10H-6, 145–150	89.25	7.09	4.144	4	38	537.512	460.777	26.103	BDL	7.21	40.96	14.59	49.40	421.69	11.91	3.4
11H-6, 126–131	98.56	7.20	4.501	34	37	548.347	464.148	26.086	BDL	7.48	35.02	15.43	50.60	443.02	11.89	3.3
12H-6, 145–150	107.16	7.14	4.556	12	37	554.485	471.682	26.643	BDL	8.49	20.15	16.16	51.29	375.44	11.81	3.2
13H-6, 145–150	117.75	6.99	4.941	5	37	561.461	479.668	26.193	BDL	10.34	BDL	16.79	50.87	393.03	12.12	3.0
14H-6, 145–150	127.25	6.99	5.026	9	37	546.407	461.073	25.476	BDL	10.98	11.27	16.68	49.00	366.87	12.72	2.9
15H-6, 140–150	136.70	7.14	5.486	22	37	552.805	469.444	25.448	BDL	11.23	17.92	17.46	49.56	353.25	12.96	2.8
16H-6, 140–150	144.9	7.13	5.588	9	37	549.918	468.336	25.795	BDL	10.63	11.61	17.44	48.93	321.62	13.62	2.8
17H-6, 91–101	155.21	ND	ND	49	37	562.077	473.088	25.471	BDL	10.38	12.31	17.77	49.43	317.08	12.68	2.8
18H-5, 132–142	162.23	7.01	5.599	5	37	551.767	467.507	25.104	BDL	8.10	1.17	17.89	49.00	381.40	12.22	2.7
19H-6, 130–140	174.60	7.46	5.78	74	37	543.069	458.911	24.526	BDL	6.80	3.51	17.90	48.35	363.84	11.44	2.7
20H-4, 140–150	181.20	7.12	5.524	13	37	547.373	467.144	24.852	BDL	9.44	13.77	18.11	48.76	367.65	11.59	2.7
21X-6, 130–140	191.70	7.05	5.32	12	37	541.022	458.622	25.539	BDL	6.41	17.47	16.923	46.213	374.62	10.252	ND
23X-5, 140–150	205.90	7.12	4.648	5	37	516.595	444.022	24.207	BDL	4.84	7.41	16.617	46.12	329.04	8.982	ND
24X-4, 140–150	214.00	7.12	4.391	4	37	529.813	453.582	25.042	BDL	4.23	0.77	16.88	46.62	305.58	9.634	ND
25X-6, 90–100	226.10	7.12	5.279	29	37	539.296	470.173	24.805	BDL	3.91	BDL	17.258	46.465	280.10	10.88	ND
26X-3, 140–150	230.89	7.17	4.45	4	37	538.126	465.138	25.788	BDL	2.94	BDL	16.813	46.17	291.95	10.798	ND
27X-6, 121–131	245.61	7.17	4.635	4	37	531.492	461.473	26.143	BDL	2.13	BDL	16.679	46.482	291.30	9.925	ND

BDL = below detection limit (HPO_4^- = 0.2 μM, Fe^{2+} = 0.6 μM), calculated as two times the standard deviation of multiple measures of a blank. ND = not determined.

Table T20. Sedimentary sample and bulk elemental geochemistry, Hole U1408A. (Continued on next two pages.)

Core, section, interval (cm)	Depth (mbsf)	$CaCO_3$ (wt%)	IC (wt%)	TC (wt%)	TN (wt%)	TOC (wt%)	Corrected TC (wt%)	Corrected TOC (wt%)	TN (wt%)
342-U1408A-									
1H-1, 37–38	0.37	32.908	3.946	4.01	0.05	0.06	5.13	1.19	0.05
1H-2, 37–38	1.87	43.595	5.227	5.05	0.05	–0.18	6.07	0.84	0.05
1H-3, 32–33	3.32	41.128	4.931	5.44	0.04	0.51	6.42	1.49	0.04
2H-1, 97–98	5.27	38.142	4.573	4.61	0.03	0.04	5.67	1.10	0.03
2H-2, 38–39	6.18	19.524	2.341	3.12	0.05	0.78	4.33	1.99	0.05
2H-3, 38–39	7.68	22.72	2.724	3.2	0.05	0.48	4.40	1.68	0.05
2H-4, 38–39	9.18	32.559	3.904	4.09	0.04	0.19	5.20	1.30	0.04
2H-5, 28–29	10.58	5.911	0.709	0.81	0.06	0.1	2.25	1.54	0.06
2H-6, 16–17	11.96	8.332	0.999	0.98	0.05	–0.02	2.40	1.40	0.05
2H-7, 19–20	13.00	0.631	0.076	0.12	0.05	0.04	0.35	0.27	0.05
3H-1, 38–39	14.18	9.047	1.085	2.97	0.06	1.89	2.44	1.35	0.06
3H-2, 38–39	15.68	7.564	0.907	0.93	0.05	0.02	2.36	1.45	0.05
3H-3, 38–39	17.18	9.142	1.096	1.17	0.06	0.07	2.57	1.48	0.06
3H-4, 38–39	18.68	0.635	0.076	0.27	0.09	0.19	0.27	0.19	0.09
3H-5, 38–39	20.18	10.663	1.278	1.39	0.07	0.11	2.77	1.49	0.07
3H-6, 27–28	21.57	13.746	1.648	1.7	0.07	0.05	3.05	1.40	0.07
3H-7, 19–20	22.49	11.708	1.404	4.15	0.09	2.75	2.80	1.40	0.09
4H-1, 82–83	24.12	15.842	1.899	2.03	0.06	0.13	3.35	1.45	0.06
4H-2, 38–39	25.18	20.289	2.433	2.59	0.06	0.16	3.85	1.42	0.06
4H-3, 38–39	26.68	17.924	2.149	2.27	0.06	0.12	3.56	1.42	0.06
4H-4, 38–39	28.18	21.871	2.622	2.59	0.06	–0.03	3.85	1.23	0.06
4H-5, 38–39	29.68	30.129	3.612	3.82	0.07	0.21	4.96	1.35	0.07
4H-6, 15–16	30.96	37.965	4.552	13.25	0.09	8.7	5.62	1.07	0.09
5H-1, 38–39	33.18	36.495	4.376	13.09	0.09	8.71	5.57	1.19	0.09
5H-2, 38–39	34.68	32.481	3.894	11.94	0.1	8.05	5.21	1.32	0.1
5H-3, 38–39	36.18	40.927	4.907	14.69	0.1	9.78	6.06	1.16	0.1
5H-4, 38–39	37.68	59.356	7.117	20.98	0.08	13.86	8.01	0.89	0.08
5H-4, 38–39	37.68	58.504	7.014						
5H-5, 38–39	39.18	36.947	4.43	13.08	0.1	8.65	5.57	1.14	0.1
5H-6, 22–23	40.52	34.153	4.095	4.43	0.06	0.34	5.51	1.42	0.06
5H-7, 15–16	41.45	38.385	4.602	13.68	0.1	9.08	5.75	1.15	0.1
6H-1, 38–39	42.68	30.526	3.66	11.12	0.11	7.46	4.96	1.30	0.11
6H-2, 38–39	44.18	34.173	4.097	12.32	0.37	8.22	5.33	1.23	
6H-3, 38–39	45.68	36.864	4.42	13.49	0.11	9.07	5.69	1.27	0.11
6H-4, 38–39	47.18	60.011	7.195	21.24	0.07	14.04	8.09	0.89	0.07
6H-4, 38–39	47.18	59.641	7.151						
6H-5, 38–39	48.68	28.552	3.423	10.68	0.1	7.26	4.82	1.40	0.1
6H-5, 38–39	48.68	27.384	3.283						
6H-6, 21–22	50.01	46.356	5.558	16.55	0.08	10.99	6.64	1.08	0.08
6H-7, 15–16	50.95	44.643	5.353	15.72	0.08	10.37	6.38	1.03	0.08
7H-3, 63–64	55.43	44.916	5.385	16.38	0.18	10.99	6.59	1.20	
7H-4, 38–39	56.68	51.752	6.205	18.64	1.08	12.44	7.29	1.08	
7H-5, 38–39	58.18	33.867	4.061	12.5	0.13	8.44	5.39	1.33	
7H-6, 38–39	59.68	32.371	3.881	11.64	0.17	7.76	5.12	1.24	
7H-7, 18–19	60.98	36.97	4.433	13.08	0.11	8.65	5.57	1.13	0.11
8H-1, 38–39	61.68	34.588	4.147	12.38	0.73	8.23	5.35	1.20	
8H-2, 38–39	63.18	32.878	3.942	12.23	0.36	8.29	5.30	1.36	
8H-3, 38–39	64.68	39.151	4.694	12.02	0.26	7.33	5.24	0.54	
8H-4, 38–39	66.18	26.626	3.192	9.51	0.1	6.32	4.46	1.27	0.1
8H-5, 38–39	67.68	34.859	4.179	13.04	0.12	8.86	5.55	1.37	0.12
8H-6, 25–26	69.05	25.526	3.061	9.98	0.12	6.92	4.61	1.55	0.12
8H-7, 12–13	70.04	42.747	5.125	15.28	0.09	10.15	6.25	1.12	0.09
9H-1, 38–39	71.18	39.843	4.777	14.44	0.1	9.66	5.99	1.21	0.1
9H-2, 38–39	72.68	30.736	3.685	13.24	0.41	9.55	5.61	1.93	
9H-3, 38–39	74.18	39.081	4.686	14.18	0.09	9.49	5.91	1.22	0.09
9H-4, 38–39	75.68	30.957	3.712	11.32	0.1	7.61	5.02	1.31	0.1
9H-5, 38–39	77.18	36.895	4.424	12.96	0.09	8.54	5.53	1.10	0.09
9H-6, 15–16	78.26	37.896	4.544	13.8	0.1	9.26	5.79	1.24	0.1
10H-1, 38–39	80.68	35.125	4.211	12.76	0.19	8.55	5.47	1.26	
10H-2, 38–39	82.18	41.497	4.975	14.65	0.18	9.67	6.05	1.08	
10H-3, 38–39	83.68	53.29	6.389	18.97	0.09	12.58	7.39	1.00	0.09
10H-4, 38–39	85.18	53.6	6.426	19.02	0.62	12.59	7.40	0.98	
10H-5, 38–39	86.68	44.076	5.285	15.71	0.09	10.43	6.38	1.09	0.09
10H-6, 38–39	88.18	33.126	3.972	11.62	0.08	7.65	5.11	1.14	0.08
10H-7, 14–15	89.44	43.526	5.219	15.33	0.49	10.11	6.26	1.04	

Table T20. (continued). (Continued on next page.)

Core, section, interval (cm)	Depth (mbsf)	$CaCO_3$ (wt%)	IC (wt%)	TC (wt%)	TN (wt%)	TOC (wt%)	Corrected TC (wt%)	Corrected TOC (wt%)	TN (wt%)
11H-1, 38–39	90.18	63.876	7.659	8.15	0.06	0.49	8.86	1.20	0.06
11H-2, 38–39	91.68	88.221	10.577	10.79	0.04	0.21	11.24	0.67	0.04
11H-3, 38–39	93.18	78.736	9.44	9.76	0.03	0.32	10.31	0.87	0.03
11H-4, 38–39	94.68	33.687	4.039	4.33	0.11	0.29	5.42	1.38	0.11
11H-4, 38–39	94.68	33.721	4.043						
11H-5, 38–39	96.18	67.073	8.042	8.23	0.06	0.19	8.94	0.89	0.06
11H-5, 38–39	96.18	66.936	8.025						
11H-6, 38–39	97.68	55.072	6.603	6.81	0.1	0.21	7.66	1.05	0.1
11H-7, 13–14	98.74	37.55	4.502	4.8	0.11	0.3	5.84	1.34	0.11
12H-1, 8–9	99.38	45.223	5.422	5.67	0.09	0.25	6.63	1.21	0.09
12H-2, 28–29	99.99	46.137	5.532	5.7	0.09	0.17	6.66	1.12	0.09
12H-3, 38–39	101.59	46.047	5.521	5.74	0.08	0.22	6.69	1.17	0.08
12H-4, 38–39	103.09	36.088	4.327	4.52	0.11	0.19	5.59	1.27	0.11
12H-5, 38–39	104.59	43.994	5.275	5.55	0.1	0.28	6.52	1.25	0.1
12H-6, 38–39	106.09	33.269	3.989	4.2	0.09	0.21	5.30	1.31	0.09
12H-7, 38–39	107.59	33.742	4.046	4.45	0.1	0.4	5.53	1.48	0.1
13H-1, 38–39	109.18	44.047	5.281	5.65	0.09	0.37	6.61	1.33	0.09
13H-2, 38–39	110.68	30.993	3.716	4.27	0.05	0.55	5.37	1.65	0.05
13H-3, 38–39	112.18	34.955	4.191	4.35	0.09	0.16	5.44	1.25	0.09
13H-4, 38–39	113.68	42.032	5.039	5.33	0.1	0.29	6.32	1.28	0.1
13H-5, 38–39	115.18	32.357	3.88	4.18	0.1	0.3	5.29	1.41	0.1
13H-6, 38–39	116.68	39.547	4.742	5.04	0.08	0.3	6.06	1.32	0.08
13H-7, 19–20	117.99	35.87	4.301	4.69	0.1	0.39	5.75	1.44	0.1
14H-1, 38–39	118.68	45.345	5.437	5.75	0.11	0.31	6.70	1.26	0.11
14H-2, 38–39	120.18	44.978	5.393	5.58	0.08	0.19	6.55	1.15	0.08
14H-3, 38–39	121.68	27.953	3.351	3.71	0.12	0.36	4.86	1.51	0.12
14H-4, 38–39	123.18	33.159	3.976	4.25	0.09	0.27	5.35	1.37	0.09
14H-5, 38–39	124.68	42.721	5.122	5.43	0.09	0.31	6.41	1.29	0.09
14H-6, 38–39	126.18	42.13	5.051	5.29	0.09	0.24	6.29	1.24	0.09
14H-7, 15–16	127.45	40.948	4.91	5.2	0.08	0.29	6.21	1.30	0.08
15H-1, 38–39	128.18	41.288	4.95	14.76	0.09	9.81	6.09	1.14	0.09
15H-2, 38–39	129.68	48.846	5.856	6.09	0.1	0.23	7.01	1.15	0.1
15H-3, 38–39	131.18	29.751	3.567	3.97	0.13	0.4	5.10	1.53	0.13
15H-4, 38–39	132.68	28.036	3.361	3.68	0.1	0.32	4.84	1.47	0.1
15H-5, 38–39	134.18	33.443	4.01	4.37	0.11	0.36	5.46	1.45	0.11
15H-6, 38–39	135.68	36.4	4.364	4.65	0.09	0.29	5.71	1.35	0.09
15H-7, 10–11	136.90	34.434	4.129	4.51	0.1	0.38	5.58	1.45	0.1
16H-1, 14–15	137.44	31.461	3.772	4.08	0.08	0.31	5.20	1.42	0.08
16H-2, 38–39	137.89	49.891	5.982	6.15	0.09	0.17	7.06	1.08	0.09
16H-3, 38–39	139.38	77.767	9.324	9.59	0.03	0.27	10.16	0.84	0.03
16H-3, 38–39	139.38	77.3	9.268						
16H-4, 38–39	140.88	30.379	3.642	3.97	0.1	0.33	5.10	1.45	0.1
16H-5, 38–39	142.38	28.379	3.403	3.83	0.12	0.43	4.97	1.57	0.12
16H-6, 38–39	143.88	34.469	4.133	4.72	0.12	0.59	5.77	1.64	0.12
16H-7, 38–39	145.38	44.963	5.391	5.55	0.08	0.16	6.52	1.13	0.08
17H-1, 37–38	147.17	60.187	7.216	7.48	0.07	0.26	8.26	1.04	0.07
17H-2, 38–39	148.68	59.164	7.094	7.26	0.06	0.17	8.06	0.97	0.06
17H-3, 38–39	150.18	39.119	4.69	5	0.08	0.31	6.02	1.33	0.08
17H-4, 38–39	151.68	47.215	5.661	5.93	0.07	0.27	6.86	1.20	0.07
17H-5, 38–39	153.18	60.875	7.299	7.57	0.04	0.27	8.34	1.04	0.04
17H-5, 38–39	153.18	60.81	7.291						
17H-6, 20–21	154.50	43.251	5.186	5.4	0.06	0.21	6.39	1.20	0.06
17H-7, 15–16	155.46	48.247	5.785	6.03	0.06	0.25	6.95	1.17	0.06
18H-1, 20–21	156.50	39.372	4.721	4.93	0.08	0.21	5.96	1.24	0.08
18H-2, 20–21	157.71	41.723	5.002	5.07	0.07	0.07	6.09	1.09	0.07
18H-3, 38–39	158.51	39.192	4.699	5.28	0.09	0.58	6.28	1.58	0.09
18H-4, 38–39	159.85	52.327	6.274	6.36	0.06	0.09	7.25	0.98	0.06
18H-5, 38–39	161.29	55.761	6.686	6.85	0.05	0.16	7.69	1.01	0.05
18H-6, 45–46	162.78	47.465	5.691	5.85	0.07	0.16	6.79	1.10	0.07
18H-7, 20–21	163.96	45.14	5.412	5.56	0.08	0.15	6.53	1.12	0.08
19H-1, 38–39	166.18	44.607	5.348	15.82	0.09	10.47	6.41	1.07	0.09
19H-2, 38–39	167.68	36.937	4.429	4.62	0.09	0.19	5.68	1.25	0.09
19H-3, 38–39	169.18	46.145	5.533	16.57	0.08	11.04	6.65	1.11	0.08
19H-3, 38–39	169.18	45.393	5.442						
19H-4, 38–39	170.68	43.622	5.23	15.29	0.07	10.06	6.25	1.02	0.07
19H-5, 38–39	172.18	49.534	5.939	17.08	0.06	11.14	6.80	0.86	0.06
19H-6, 38–39	173.68	46.445	5.569	17.08	0.06	11.51	6.80	1.23	0.06
19H-7, 10–11	174.80	47.171	5.656	5.87	0.08	0.21	6.81	1.15	0.08
20H-1, 38–39	175.68	47.394	5.682	16.42	0.06	10.74	6.60	0.92	0.06

Table T20. (continued).

Core, section, interval (cm)	Depth (mbsf)	$CaCO_3$ (wt%)	IC (wt%)	TC (wt%)	TN (wt%)	TOC (wt%)	Corrected TC (wt%)	Corrected TOC (wt%)	TN (wt%)
20H-2, 38–39	177.18	46.458	5.57	16.26	0.08	10.69	6.55	0.98	0.08
20H-3, 38–39	178.68	39.858	4.779	13.97	0.09	9.19	5.84	1.06	0.09
20H-4, 38–39	180.18	37.461	4.491	4.71	0.07	0.22	5.76	1.27	0.07
20H-5, 38–39	181.68	41.285	4.95	14.93	0.07	9.98	6.14	1.19	0.07
21X-1, 33–34	183.23	46.583	5.585	16.23	0.07	10.64	6.54	0.95	0.07
21X-1, 33–34	183.23	44.387	5.322						
21X-2, 71–72	185.11	43.003	5.156	14.79	0.07	9.63	6.09	0.94	0.07
21X-3, 46–47	186.36	47.419	5.685	16.7	0.08	11.01	6.69	1.00	0.08
21X-4, 26–27	187.66	46.742	5.604	16.32	0.08	10.72	6.57	0.96	0.08
21X-5, 66–67	189.56	49.708	5.96	17.07	0.07	11.11	6.80	0.84	0.07
21X-6, 38–39	190.78	46.069	5.524	16.16	0.07	10.64	6.52	0.99	0.07
21X-7, 15–16	191.95	48.121	5.77	16.81	0.05	11.04	6.72	0.95	0.05
21X-7, 15–16	191.95	44.161	5.295						
22X-1, 39–40	189.39	44.431	5.327	5.52	0.08	0.19	6.49	1.17	0.08
22X-2, 36–37	190.66	40.156	4.815	5.06	0.08	0.25	6.08	1.26	0.08
22X-3, 36–37	192.16	42.026	5.039	5.24	0.1	0.2	6.24	1.20	0.1
22X-4, 44–45	193.74	42.622	5.11	5.41	0.08	0.3	6.39	1.28	0.08
22X-5, 36–37	195.16	39.838	4.776	4.83	0.08	0.05	5.87	1.10	0.08
22X-6, 35–36	196.67	47.528	5.698	5.89	0.06	0.19	6.83	1.13	0.06
22X-7, 17–18	197.99	39.923	4.787	4.99	0.08	0.2	6.02	1.23	0.08
23X-1, 51–52	199.01	40.969	4.912	5.12	0.07	0.21	6.13	1.22	0.07
23X-2, 40–41	200.40	41.002	4.916	5.12	0.08	0.2	6.13	1.22	0.08
23X-3, 82–83	202.32	44.212	5.301	5.37	0.07	0.07	6.36	1.06	0.07
23X-4, 37–38	203.37	49.305	5.912	6.06	0.08	0.15	6.98	1.07	0.08
23X-5, 19–20	204.69	39.462	4.731	4.88	0.08	0.15	5.92	1.19	0.08
23X-6, 62–63	206.62	38.52	4.618	4.79	0.09	0.17	5.84	1.22	0.09
24X-1, 31–32	208.41	41.448	4.969	15.21	0.05	10.24	6.22	1.26	0.05
24X-2, 10–11	209.70	44.736	5.364	5.61	0.07	0.25	6.57	1.21	0.07
24X-3, 41–42	211.51	49.534	5.939	6.21	0.08	0.27	7.12	1.18	0.08
24X-4, 44–45	213.04	43.987	5.274	5.48	0.07	0.21	6.46	1.18	0.07
24X-5, 35–36	214.45	35.233	4.224	4.51	0.08	0.29	5.58	1.36	0.08
25X-1, 36–37	218.06	40.063	4.803	4.96	0.07	0.16	5.99	1.19	0.07
25X-2, 52–53	219.72	35.599	4.268	4.48	0.06	0.21	5.56	1.29	0.06
25X-3, 80–81	221.50	45.512	5.457	5.53	0.05	0.07	6.50	1.05	0.05
25X-4, 19–20	222.39	44.092	5.286	5.45	0.06	0.16	6.43	1.14	0.06
25X-5, 22–23	223.92	66.128	7.928	7.92	0.02	–0.01	8.66	0.73	0.02
25X-6, 25–26	225.45	90.945	10.904	10.97	0	0.07	11.40	0.50	0
25X-7, 23–24	226.43	89.222	10.697	10.78	0	0.08	11.23	0.54	0
26X-1, 3–4	227.33	89.949	10.785	10.76	0	–0.02	11.22	0.43	0
26X-2, 49–50	228.48	73.584	8.822	9.01	0.01	0.19	9.64	0.82	0.01
26X-3, 45–46	229.94	55.488	6.653	6.69	0	0.04	7.55	0.89	0
26X-4, 62–63	231.61	86.241	10.34	10.28	0.01	–0.06	10.78	0.44	0.01
27X-1, 79–80	237.69	80.537	9.656	9.76	0	0.1	10.31	0.66	0
27X-2, 70–71	239.10	82.755	9.922	9.76	0	–0.16	10.31	0.39	0
27X-3, 85–86	240.75	80.374	9.637	9.49	–0.01	–0.15	10.07	0.43	–0.01
27X-4, 78–79	242.18	77.723	9.319	9.25	0.01	–0.07	9.85	0.54	0.01
27X-5, 76–77	243.66	71.704	8.597	8.88	0	0.28	9.52	0.92	0
27X-6, 32–33	244.72	66.877	8.018	8.79	0.03	0.77	9.44	1.42	0.03
27X-7, 18–19	245.89	73.095	8.764	8.77	0	0.01	9.42	0.66	0

For corrected total carbon (TC) with low-carbonate estuarine sediment calibration, if TC < 2.2 wt%, no correction was applied; if TC > 2.2 wt%, corrected TC = 2.2 + (x – 2.2) × 0.309. For corrected TC with high-carbonate La Luna shale calibration, if TC < 2.2/2.913, corrected TC = 2.913 × x; if TC > 2.2/2.913, corrected TC = 2.2 + (x – 2.2/2.913) × 0.901. Corrected total organic carbon (TOC) is corrected TC minus inorganic carbon (IC). Total nitrogen (TN) values are uncorrected with anomalous values removed.

Table T21. Thermal conductivity results, Hole U1408A.

Core, section, interval (cm)	Depth (mbsf)	Thermal conductivity (W/[m·K])			Heating power (W/m)
		Mean	Standard deviation	Observation	
342-U1408A-					
1H-3W, 60	3.01	1.017	3.30E–03	1.012	1.815
1H-3W, 60	3.01			1.019	1.815
1H-3W, 60	3.01			1.018	1.815
2H-3A, 75	7.31	1.078	3.10E–03	1.073	1.815
2H-3A, 75	7.31			1.079	1.815
2H-3A, 75	7.31			1.081	1.815
3H-3A, 75	16.81	1.048	5.70E–03	1.041	1.815
3H-3A, 75	16.81			1.055	1.815
3H-3A, 75	16.81			1.048	1.815
4H-3A, 75	26.31	1.129	5.50E–03	1.123	1.815
4H-3A, 75	26.31			1.134	1.815
5H-3A, 75	35.81	1.074	7.90E–03	1.075	1.815
5H-3A, 75	35.81			1.083	1.815
5H-3A, 75	35.81			1.064*	1.815
6H-3A, 75	45.31	1.085	2.60E–03	1.082	1.815
6H-3A, 75	45.31			1.087	2.016
7H-3A, 75	54.81	1.102	1.34E–02	1.083*	2.016
7H-3A, 75	54.81			1.109	2.016
7H-3A, 75	54.81			1.113	2.016
8H-3A, 75	64.31	1.126	9.30E–03	1.114	2.016
8H-3A, 75	64.31			1.137*	2.016
8H-3A, 75	64.31			1.127	2.016
9H-3A, 75	73.81	1.227	—	1.227	2.016
10H-3A, 75	83.31	1.109	4.94E–01	1.091*	2.016
10H-3A, 75	83.31			1.109	2.016

* = result obtained directly from the TK04 processing software. Other results were generated by the IODP uploader using raw data because they were rejected by the TK04 software. Thermal conductivity mean and standard deviation calculated from thermal conductivity observations. Heating power used to perform the measurement is also listed. — = incalculable data.

Table T22. Core top and composite depth, Site U1408. (Continued on next page.)

Core	Depth (mbsf)	Depth (m CCSF)	Offset (m)	Cumulative offset (m)	Comment	Data sets used
342-U1408A-						
1H	0.00	0.00	0.00	0.00		Physical properties
2H	4.30	5.40	1.10	1.10		Physical properties
3H	13.80	17.30	2.40	3.50		Physical properties
4H	23.30	27.35	0.55	4.05		Physical properties
5H	32.80	35.65	–1.20	2.85		XRF core scanning
6H	42.30	45.65	0.50	3.35		XRF core scanning
7H	51.80	58.65	3.50	6.85		XRF core scanning
8H	61.30	68.94	0.79	7.64		XRF core scanning
9H	70.80	79.42	0.98	8.62		XRF core scanning
10H	80.30	89.47	0.55	9.17		XRF core scanning
11H	89.80	102.07	3.10	12.27		XRF core scanning
12H	99.30	112.67	1.10	13.37		XRF core scanning
13H	108.80	123.22	1.05	14.42		XRF core scanning
14H	118.30	133.82	1.10	15.52		XRF core scanning
15H	127.80	144.92	1.60	17.12		XRF core scanning
16H	137.30	156.17	1.75	18.87		XRF core scanning
17H	146.80	168.05	2.38	21.25		XRF core scanning
18H	156.30	177.85	0.30	21.55		XRF core scanning
19H	165.80	187.21	–0.14	21.41	Tentative	XRF core scanning
20H	175.30	198.57	1.86	23.27	Tentative	XRF core scanning
21X	182.90	206.12	–0.05	23.22	Tentative	XRF core scanning
22X	189.00	215.75	3.53	26.75	Tentative	XRF core scanning
23X	198.50	225.05	–0.20	26.55	Tentative	XRF core scanning
24X	208.10	234.85	0.20	26.75		Physical properties
25X	217.70	244.65	0.20	26.95		Physical properties
26X	227.30	254.45	0.20	27.15		Physical properties
27X	236.90	264.25	0.20	27.35		Physical properties
342-U1408B-						
1H	0.00	0.00	0.00	0.00		Physical properties
2H	6.70	7.45	0.75	0.75		Physical properties
3H	16.20	18.45	1.50	2.25		Physical properties
41	25.70	27.95	0.00	2.25		Physical properties
5H	28.70	29.25	–1.70	0.55		XRF core scanning
6H	38.20	37.70	–1.05	–0.50		XRF core scanning
7H	47.70	48.10	0.90	0.40		XRF core scanning
8H	57.20	58.95	1.35	1.75		XRF core scanning
9H	66.70	68.59	0.14	1.89		XRF core scanning
10H	76.20	79.44	1.35	3.24		XRF core scanning
11H	81.20	84.97	0.53	3.77		XRF core scanning
12H	90.70	94.77	0.30	4.07		XRF core scanning
13H	100.20	103.87	–0.40	3.67		XRF core scanning
14H	109.70	114.17	0.80	4.47	Disturbed	XRF core scanning
15H	119.20	124.17	0.50	4.97		XRF core scanning
16H	128.70	135.02	1.35	6.32		XRF core scanning
17H	135.60	142.42	0.50	6.82		XRF core scanning
18H	145.00	152.27	0.45	7.27		XRF core scanning
19X	154.50	162.85	1.08	8.35	Tentative	XRF core scanning
20X	161.50	171.41	1.56	9.91	Tentative	XRF core scanning
21X	171.10	181.01	0.00	9.91	Tentative	XRF core scanning
22X	179.10	191.47	2.46	12.37	Tentative	XRF core scanning
23X	187.10	199.97	0.50	12.87	Tentative	XRF core scanning
24X	192.60	207.42	1.95	14.82	Tentative	XRF core scanning
25X	202.20	217.90	0.88	15.70	Tentative	XRF core scanning
26X	211.80	227.50	0.00	15.70	Tentative	Physical properties
342-U1408C-						
1H	0.00	0.20	0.20	0.20		Physical properties
21	8.80	9.00	0.00	0.20		Physical properties
3H	11.80	13.10	1.10	1.30		Physical properties
4H	21.30	23.60	1.00	2.30	Tentative	Physical properties
5H	30.80	31.90	–1.20	1.10		XRF core scanning
6H	40.30	41.30	–0.10	1.00		XRF core scanning
7H	49.80	52.15	1.35	2.35		XRF core scanning
8H	59.30	62.25	0.60	2.95		XRF core scanning
9H	68.80	72.84	1.09	4.04		XRF core scanning
10H	78.30	82.47	0.13	4.17		XRF core scanning
11H	87.80	92.12	0.15	4.32		XRF core scanning
12H	97.30	100.67	–0.95	3.37	Pull up 2.5 m	XRF core scanning

Table T22. (continued).

Core	Depth (mbsf)	Depth (m CCSF)	Offset (m)	Cumulative offset (m)	Comment	Data sets used
13H	104.30	108.52	0.85	4.22		XRF core scanning
14H	113.80	118.82	0.80	5.02		XRF core scanning
15H	121.80	127.22	0.40	5.42		XRF core scanning
16H	131.30	137.72	1.00	6.42		XRF core scanning
17H	140.80	148.22	1.00	7.42		XRF core scanning
18H	146.50	157.42	3.50	10.92	Tentative	XRF core scanning
19H	156.00	167.90	0.98	11.90	Tentative	XRF core scanning
20X	165.10	177.46	0.46	12.36		XRF core scanning
21X	0.00	0.20	0.20	0.20		Physical properties
22X	8.80	9.00	0.00	0.20		Physical properties
23X	11.80	13.10	1.10	1.30		Physical properties

Table T23. Splice tie points, Site U1408.

Hole, core, section, interval (cm)	Depth (mbsf)	Depth (m CCSF)		Hole, core, section, interval (cm)	Depth (mbsf)	Depth (m CCSF)	Comment	Data sets used
342-				342-				
				U1408B-1H-1, 0	0.00	0.00		Physical properties
U1408B-1H-3, 100	4.00	4.00	Tie to	U1408C-1H-3, 81	3.81	4.00		Physical properties
U1408B-1H-1, 131	7.31	7.51	Tie to	U1408A-2H-2, 61	6.41	7.51		Physical properties
U1408A-2H-3, 76	8.06	9.16	Tie to	U1408B-2H-2, 20	8.40	9.16		Physical properties
U1408B-2H-5, 95	13.65	14.40	Tie to	U1408C-3H-1, 130	13.10	14.40		Physical properties
U1408C-3H-5, 60	18.40	19.70	Tie to	U1408B-3H-1, 125	17.45	19.70		Physical properties
U1408B-3H-6, 83	24.55	26.80	Tie to	U1408C-4H-3, 21	24.51	26.80		Physical properties
U1408C-4H-5, 109	28.39	30.69	Tie to	U1408B-5H-1, 145	30.15	30.69	Tentative	Physical properties
U1408B-5H-6, 150	37.70	38.25	Tie to	U1408A-5H-2, 109	35.39	38.25		XRF core scanning
U1408A-5H-6, 35	40.65	43.50	Tie to	U1408C-6H-2, 69	42.49	43.50		XRF core scanning
U1408C-6H-6, 48	48.31	49.31	Tie to	U1408B-7H-1, 120	48.90	49.31		XRF core scanning
U1408B-7H-5, 115	54.85	55.25	Tie to	U1408C-7H-3, 11	52.91	55.25		XRF core scanning
U1408C-7H-6, 120	58.50	60.85	Tie to	U1408B-8H-2, 40	59.10	60.85		XRF core scanning
U1408B-8H-6, 80	65.50	67.25	Tie to	U1408C-8H-4, 50	64.31	67.25		XRF core scanning
U1408C-8H-6, 122	68.03	70.98	Tie to	U1408A-8H-2, 54	63.34	70.98		XRF core scanning
U1408A-8H-6, 41	69.21	76.85	Tie to	U1408C-9H-3, 101	72.81	77.46		XRF core scanning
U1408C-9H-5, 120	76.00	80.04	Tie to	U1408A-9H-1, 62	71.42	81.29		XRF core scanning
U1408A-9H-3, 105	74.85	83.47	Tie to	U1408C-10H-1, 100	79.30	84.15		XRF core scanning
U1408C-10H-6, 9	85.89	90.06	Tie to	U1408B-11H-4, 60	86.30	90.74		XRF core scanning
U1408B-11H-6, 50	89.20	92.97	Tie to	U1408A-10H-3, 50	83.80	93.65		XRF core scanning
U1408A-10H-6, 31	88.11	97.28	Tie to	U1408B-12H-2, 100	93.20	97.96		XRF core scanning
U1408B-12H-6, 90	99.10	103.17	Tie to	U1408C-12H-2, 99	99.79	103.85		XRF core scanning
U1408C-12H-4, 40	102.20	105.57	Tie to	U1408A-11H-3, 51	93.31	106.25		XRF core scanning
U1408A-11H-6, 34	97.64	109.91	Tie to	U1408C-13H-1, 139	105.69	110.59		XRF core scanning
U1408C-13H-6, 31	111.51	115.73	Tie to	U1408B-14H-2, 5	111.25	116.41		XRF core scanning
U1408B-14H-5, 65	116.35	120.82	Tie to	U1408C-14H-2, 49	115.79	121.50		XRF core scanning
U1408C-14H-4, 124	119.54	124.56	Tie to	U1408A-13H-1, 135	110.15	125.24		XRF core scanning
U1408A-13H-5, 49	115.29	129.71	Tie to	U1408C-15H-2, 99	124.29	130.39		XRF core scanning
U1408C-15H-6, 91	130.21	135.63	Tie to	U1408A-14H-2, 30	120.10	136.31		XRF core scanning
U1408A-14H-6, 40	126.20	141.72	Tie to	U1408C-16H-3, 100	135.30	142.40		XRF core scanning
U1408C-16H-5, 71	138.01	144.43	Tie to	U1408B-17H-2, 50	137.60	145.11		XRF core scanning
U1408B-17H-5, 130	142.58	149.40	Tie to	U1408C-17H-1, 118	141.98	150.08		XRF core scanning
U1408C-17H-4, 31	145.61	153.03	Tie to	U1408B-18H-1, 75	145.75	153.71		XRF core scanning
U1408B-18H-4, 100	150.50	157.77	Tie to	U1408A-16H-2, 140	138.91	158.45		XRF core scanning
U1408A-16H-6, 96	144.46	163.33	Tie to	U1408B-19X-1, 48	154.98	164.20		XRF core scanning
U1408B-19X-5, 20	160.70	169.05	Tie to	U1408A-17H-1, 100	147.80	169.85		XRF core scanning
U1408A-17H-5, 82	153.62	174.87	Tie to	U1408B-20X-3, 46	164.96	176.20	Tentative	XRF core scanning
U1408B-20X-5, 105	168.55	178.46	Tie to	U1408C-20X-1, 100	166.10	179.05		XRF core scanning
U1408C-20X-3, 123	169.33	181.69	Tie to	U1408B-21X-1, 70	171.80	182.28	Tentative	XRF core scanning
U1408B-21X-7, 16	180.26	190.17	Tie to	U1408A-19H-2, 146	168.76	190.65	Tentative	XRF core scanning
U1408A-19H-5, 20	172.00	193.41	Tie to	U1408B-22X-2, 44	181.04	194.12	Tentative	XRF core scanning
U1408B-22X-6, 25	186.85	199.22	Tie to	U1408A-20H-1, 65	175.95	198.85	Tentative	XRF core scanning
U1408A-20H-3, 40	178.70	201.97	Tie to	U1408B-23X-2, 50	189.10	201.60	Tentative	XRF core scanning
U1408B-23X-5, 85	193.95	206.82	Tie to	U1408A-21X-1, 70	183.60	206.45		XRF core scanning
U1408A-21X-5, 30	189.20	212.42	Tie to	U1408B-24X-4, 50	197.60	212.05		XRF core scanning
U1408B-24X-CC, 7	201.92	216.74	Tie to	U1408A-22X-1, 88	189.88	216.37	Tentative	Physical properties
U1408A-22X-3, 35	192.15	219.02	Tie to	U1408B-25X-1, 100	203.20	218.65	Tentative	XRF core scanning
U1408B-25X-6, 65	210.35	226.17	Tie to	U1408A-23X-1, 100	199.50	225.80		XRF core scanning
U1408A-23X-6, 136	207.36	234.03	Append to	U1408A-24X-1, 9	208.19	233.66		Physical properties
U1408A-24X-5, 123	215.33	242.20	Append to	U1408A-25X-1, 28	217.98	241.83		Physical properties
U1408A-25X-7, 68	226.88	253.95	Append to	U1408A-26X-1, 7	227.37	253.58		Physical properties
U1408A-26X-4, 98	231.97	259.24	Append to	U1408A-27X-1, 25	237.15	258.87		Physical properties
U1408A-27X-7, 63	246.34	273.81						Physical properties

Table T24. Downhole temperature, Hole U1408A.

Core	Depth DSF (m)	Temperature (°C)	Thermal resistance (m^2K/W)	Remark
342-U1408A-				
	0.0	2.72		Mudline temperature
4H	32.8	NA	31.48	Unusable
7H	61.3	5.10	58.31	Moderate sea
10H	89.8	6.16	82.70	Moderate sea
13H	118.3	7.39	106.44	Moderate sea

ND = no data.